2D phonon thermal transport in thin SiN film

Master's thesis, March 18, 2019

Author:

Teemu Loippo

Supervisor:

Ilari Maasilta

UNIVERSITY OF JYVÄSKYLÄ
DEPARTMENT OF PHYSICS

Tiivistelmä

Loippo, Teemu
2D lämpöfononien kulkeutuminen ohuessa SiN kalvossa
Pro gradu
Fysiikan laitos, Jyväskylän yliopisto, 2019, 91 sivua

Tässä tutkielmassa suunnitellaan, valmistetaan ja kokeillaan uudenlaista suprajohde-normaalimetalli-suprajohde (SNS) lämmintintä. Uutta lämmittimessä on sen geometria, jonka on tarkoitus tehdä mittaustulosten analysoinnista helpompaa kuin aiemmin. SNS liitoksen käyttäminen lämmittimenä suprajohde-eriste-normaalimetalli-eriste-suprajohde (SINIS) liitoksen sijaan antaa suuremman tehoalueen tutkittavaksi, sillä SNS liitos on kestävämpi kuin herkkä SINIS liitos. Lisäksi SNS liitoksen etuna on se, että lämpöenergia emittoidaan koko normaalimetallista, kun taas SINIS liitokseen perustuvassa lämmittimessä suurin osa emissiosta tapahtuu tunneliliitoksen alueella. Työssä käytettiin jo aiemmista kokeista tuttua SINIS liitokseen perustuvaa lämpömittaria, mutta liitos oli hieman pienempi kuin aiemmin. SNS ja SINIS liitokset valmistettiin itsekantavan SiN kalvon päälle.

Valmistusprosessien optimoinnin jälkeen SiN kalvolle valmisettu näyte mitattiin lämmittämällä kavoa ja samanaikaisesti mitaten kalvon lämpötilaa. Mittauksista saatiin selville SiN kalvon lämmönjohtuvuus, tosin ensimmäinen mitattava näyte ei ollut täydellisen onnistunut ja mittauksessa oli selviä virhelähteitä. Kaikki erot aiempiin mittauksiin pyrittiin selittämään ja pääosin tulokset olivat samassa linjassa aiempien tulosten kanssa. Kun mittauksiin liittyvät ongelmat saatiin korjattua, olivat uudet mittaustulokset hyviä. Lisäksi lämmöjohtumisen simulaatiomalliin tehtiin muutoksia, jolloin kokeelliset tulokset sopivat lähes täydellisesti yhteen simulaation kanssa. Tulevaisuudessa vastaavanlaiset mittaukset suoritetaan ohuemmille SiN kalvoille ja fononikiderakenteille.

Avainsanat: SINIS lämpömittari, SNS lämmitin, Ballistiset fononit, SiN kalvo, Lämmönjohtuvuus

Abstract

Loippo, Teemu
2D thermal phonon transport in thin SiN membrane
Master's thesis
Department of Physics, University of Jyväskylä, 2019, 91 pages.

This thesis contains the design, fabrication and initial tests for a new type of a superconductor-normal metal-superconductor (SNS) heater element. The novel part is the heater geometry, which should make the heating experiment analysis simpler than previously. Also utilizing the SNS junction as a heater instead of a superconductor-insulator-normal metal-insulator-superconductor (SINIS) junction was different compared to the previous experiments. The SNS heater allows greater power range compared to the SINIS heater, beacause SNS junctions are more robust compared to SINIS junctions. Also the heat is emitted from the normal metal, whereas in SINIS heaters most of the heat is emitted from the junction area. In this work the thermometer was a typical SINIS junction with a bit smaller dimensions than in previous experiments. SINIS and SNS junctions were fabricated on top of a suspended SiN membrane.

After the fabrication processes were optimized, the thermal conductance of a SiN membrane sample was measured. The first results were promising although the data was aquired by using a non-ideal sample and non-ideal measurement setup. All differences to previously measures samples were explained. Once all issues with the measauremnts were solved the experiments were run again with good results. In addition some modifications to the simulation model were done. The experimental results agreed well with the updated simulation model. Also the heating experiment will be performed for thinner SiN membranes and for a phononic crystal structure in the future.

Keywords: SINIS thermometry, SNS heater, Ballistic phonons, SiN membrane, Thermal conductivity

Acknowledgements

I got lured into nanosciences in 2016 when I did my bachelor's thesis about helium ion microscope. Since then I have gotten more and more amazed about all the things that are done at the Nanoscience Center. Now approximately three years later, my master's thesis is finally ready. At first i'd like to thank my supervisor Professor Ilari Maasilta for the opportunity to work in his group. Every project I've taken part has been interesting and I hope to continue working with this magnificent group also in the future.

Laboratory engineers Dr. Kimmo Kinnunen and Mr. Tarmo Suppula kept laboratory equipment running and always offered help when needed. Their work is very much appreciated, thank you! Special thanks to Mr. Samuli Heiskanen and Mr. Geng Zhuoran for their advice in fabrication processes and cryostat operation. For fruitful theory discussions and simulation data for this thesis I want to thank Dr. Tuomas Puurtinen. Discussions about fabrication processes and difficulties included in them with Ms. Emmi Kirjanen have been helpful.

Finally I wish to thank my parents and my sister for their support and understanding during this process. Also support from all my friends is gratefully appreciated.

Jyväskylä March 18, 2019

Teemu Loippo

Contents

Tiivistelmä **3**

Abstract **5**

Acknowledgements **7**

1 Introduction **11**
1.1 Motivation 11
1.2 Previous work 12
1.3 Scope of this project 15

2 Theory **17**
2.1 A short introduction to superconductivity 17
2.2 Andreev reflection 19
2.3 Proximity effect 21
2.4 SNS junction 22
2.5 SINIS thermometry 23
2.6 Heat conduction at low temperatures 24
2.6.1 Phonons 24
2.6.2 Diffusive heat transfer 25
2.6.3 Heat transfer in superconductors 26
2.6.4 Rayleigh-Lamb theory of elastic waves 27
2.6.5 Heat conduction in dielectric membranes 31
2.6.6 Geometrical considerations of the radiation law 33
2.6.7 Heat flow at material interfaces 34

3 Fabrication methods and equipment **37**
3.1 Electron beam lithography 39
3.2 Metal evaporation 39
3.3 Suspended SiN membrane fabrication 40
3.4 SNS design and fabrication 41
3.5 Theory of heater thermometer geometries in ballistic regime 44
3.6 SINIS design and fabrication 46
3.7 Challenges 47

4 Measurements and results **51**
4.1 Experimental methods and equipment 51
4.2 Data analysis and results of the first measurement run 56

4.2.1 Proximity effect on Nb wire coated with Ti Au bilayer 56
4.2.2 SINIS IV curves 59
4.2.3 SINIS calibration 63
4.2.4 Heating experiment 63
4.2.5 SINIS T_c 70
4.3 Data analysis and results of the second measurement run 71
4.3.1 SINIS IV curves 72
4.3.2 SINIS calibration 75
4.3.3 Heating experiment 77

5 Conclusions **85**

References **87**

1 Introduction

Heat is a form of energy and depending on the situation it can be beneficial or unwanted property. For example a cold winter evening is comfortably spent in front of a fireplace with a good book, but on the other hand overheating electrical components or mechanical parts can pose a fire hazard or an expensive repair invoice. Understanding the behaviour of thermal energy and its transport properties (thermal conductance) is important to make more efficient electrical and mechanical components. To understand these properties a fundamental laws of nauture and some way of probing few physical quantities are needed. In order to get an estimate of thermal conductance of an object a heater element is needed with a way of measuring the heating power. Also two thermometers are needed for measuring temperature of hot and cold ends of the object. To obatin accurate value for the temperature of the hot end of the object we have to rely on the zeroth law of thermodynamics, which states that if two objects A and B are in thermal equilibrium with a third object C then also A and B are in thermal equilibrium. Then Fourier's law can be used in diffusive limit to calculate the thermal conductance of the object. Through this example it is understood that good coupling of the heater and the thermometer located at the hot end is essential to making the experiments more accurate.

This thesis contains the design, fabrication and measurements of a nanoscale thermal transport measurement device. The device differs from previous ones by the heater geometry. The geometry introduced has an improved power transmission into the thermometer, giving a higher sensitivity, and ideally a direct measure of the heater temperature. The thermometer still uses the same geometry as before, but is smaller in size.

1.1 Motivation

Photons are quanta of vibrations of electromagnetic (EM) field. The spectrum of EM field has been studied for a long time and the use of it has become self-evident in everyday life. The EM field enables the use of many technologies such as wireless communication, radars, X-ray imaging and so on. Similarly phonons are quanta of vibrations of matter and thus responsible for transferring sound and heat. Phononics is a relatively new field of study, at least if compared to photonics. Main goal of phononics is to harness the phononic spectrum to good use just like scientists have already done with photonics. Phononic spectrum can be divided into different regimes just like EM field.

In general phononics covers a vast range of possible applications in different fields from thermoelectric energy harvesting to medical imaging. Phononic crystals (PnC) are structures that affect material vibrations (phonons) and they can be realized in 1D, 2D or 3D. Here are few interesting examples of the field.

PnC studies for thermal transport are important at least for detector development where PnCs are used for sensitivity and response time optimization [1]. Our group has actively taken part in PnC development for detector applications. There is also an ongoing study of PnC application to lengthen the lifetime of quasiparticle excitations in kinetic inductance detectors (KID) [2]. Longer quasiparticle lifetime increases the sensitivity of a detector. KIDs are also fascinating devices that have multiple application possibilities such as photon detection [3].

More everyday applications of PnCs in acoustics and ultrasonics include for example interior noise dampening with a 2D PnC placed into the ceiling of a car [4]. There is an effort to get higher resolution for medical ultrasonic imaging using acusto-plasmonic resonators [5] as coherent phonon sources. PnCs could be used to guide these phonons for different purposes [6].

Quantum computing might also benefit from PnC structures and this particular application is currently under heavy research [7–9]. Other examples can be found from references [10] and [11].

1.2 Previous work

Previous work done in our group already includes 2D phononic crystal and uncut membrane heat transport studies [12]. The PnC structure was realized by fabricating cylindrical holes with square lattice geometry on a suspended SiN membrane see Figure 1. The previous PnC experiment data can be seen in Figure 2. The sample was heated and local temperature of the membrane was measured along with the heating power. Data from 300 nm thick bare SiN membranes and PnC structures with different periods were were compared [13]. These results were not adjusted for the geometry dependent view factors, that are discussed later. Such view factor corrections have been calculated for previously acquired data in a newer article [14].

However with new equipment, a helium ion microscope (HIM), we have preliminary studies to fabricate smaller features, than before [15]. Those PnCs are supposed to have different properties than the previously studied PnCs. HIM provides ion beam milling capability with helium or neon gas. Typically ion beam milling is done using a gallium beam, but the problem with Ga is its capability to contaminate the sample by implantation, and its lower resolution compared to HIM. Still Ga ion milling of dielectric membranes was studied elsewhere [16]. The smallest period of a PnC structure fabricated in our laboratory with e-beam lithography and reactive ion etching prior to HIM use was about 1 μm, but with HIM, a period of about 120 nm has been achieved successfully while maintaining an acceptable filling factor

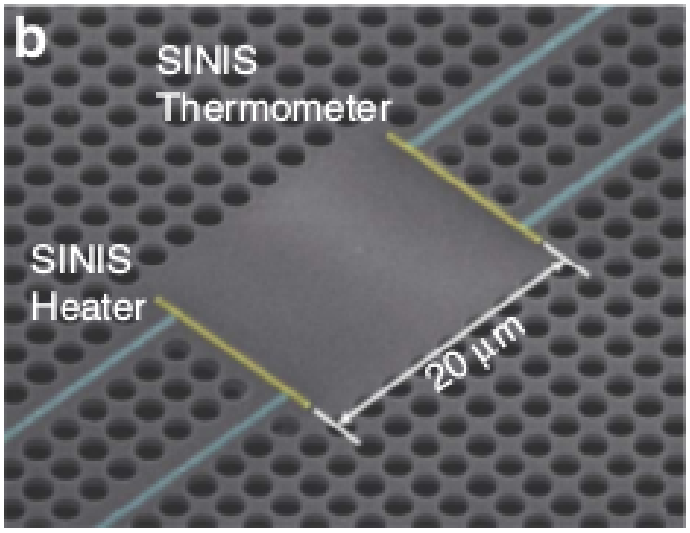

Figure 1. This is typically used measurement setup in previous experiments. The figure is taken from [12].

of 0.5–0.6 [15]. Even smaller period could be achieved by fine tuning the milling parameters. The newer smaller period PnC structure has a hexagonal lattice, whereas a square lattice was used previously.

Other material choices for PnCs have also been studied by others. For example, Sledzinska et al [17], Maire et al [18] and Tang et al [19] have successfully fabricated 2D phononic crystals on thin silicon membranes with similar holey patterns as were demonstrated by our group [12]. In addition Sledzinska et al fabricated a solid-solid PnC structure, where Ti Al bilayer nanopillars were periodically deposited on top of the Si membrane following the same lattice geometry as in the holey case.

A simulation study made in our group implies that a phononic crystal with small enough period can have unintuitive properties at low temperatures, see Figure 3. The effect that arises is the improvement of the heat conductance in the PnC structure compared to the bare membrane [20]. In addition, enhancement of the heat capacity was observed in simulations in small period PnCs [21].

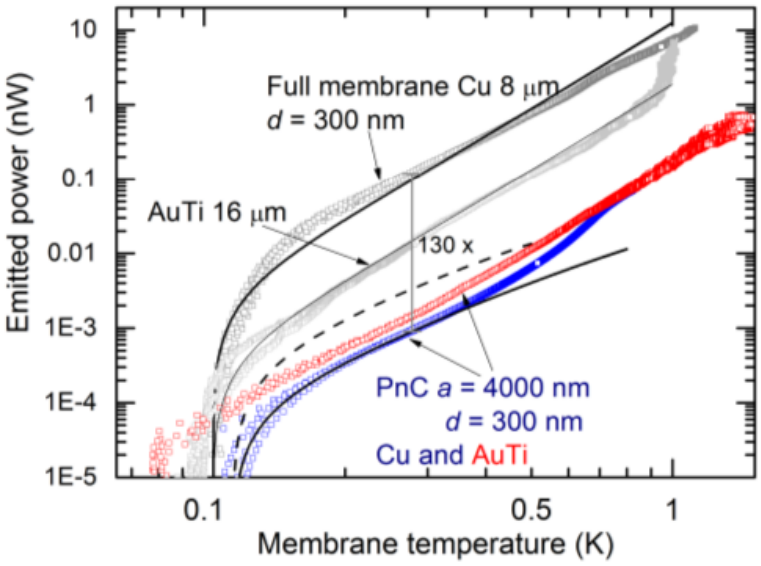

Figure 2. Result from previous experiment comparing bare membrane and a PnC structure [13].

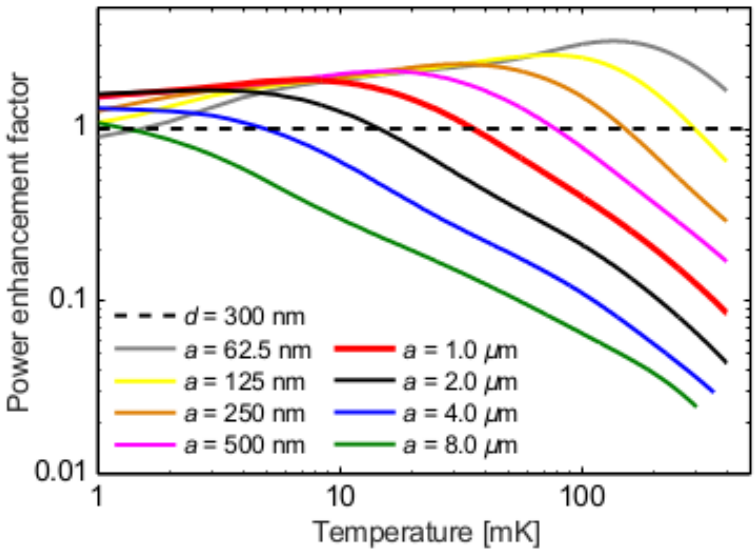

Figure 3. Simulation of power transferred over a PnC by phonons. The dotted line represents unmodified 300 nm thick SiN membrane. Different colors correspond to different periods of the PnC structure [20].

There is also a study of temperature profile of a suspended SiN membrane [22]. The experiment was conducted by heating the membrane with radially symmetric heater and measuring the temperatures at different distances from the heater. The temperature profile measured was in agreement with ballistic theory up to 50 μm distance from the heater element, which is roughly the membrane size used in

this thesis. The membrane thickness was about 40 nm. Some simulations of the temperature profile were also provided, but with 200 nm membrane thickness in the 3D phonon limit. The simulation showed lower temperatures than in the experiment for the same heating power in the ballistic limit.

1.3 Scope of this project

In this work the focus is on the heat transport properties of a thin dielectric membrane, silicon nitride (SiN) in this case. This project only considers the two dimensional case where the PnC would be a thin membrane with nanoscale patterns embedded into the membrane. There are also many other ways to realize a PnC in two dimensions [11].

This master's thesis project considers a new measurement geometry schematically shown in figure 4. The heater structure will be surrounded by the PnC structure in the future for PnC characterization, but is out of the scope of this thesis. The new geometry has some benefits compared to the previously used measurement geometries, shown in Figure 1. The main advantage of the new geometry is that the view factor, i.e. the fraction of phonon radiation leaving the thermometer that is intercepted by the thermometer, should be close to one. If it is assumed that phonons are radiated isotropically, the simple view factor renders the temperature analysis trivial, as will be discussed in section 2. A superconductor-normal metal-superconductor (SNS) junction is used as a heater element. It surrounds the inner structure which is a superconductor-insulator-normal metal-insulator-superconductor (SINIS) junction and is used as a thermometer. The fact that the heater surrounds the thermometer makes the placement of the thermometer non-critical. In other words the placement of the thermometer shouldn't affect the temperature readings too much. The fact that SNS heater is used also has the benefit that all power is dissipated in the normal metal due to Andreev reflection, whereas for NIS junction power is dissipated equally between the two electrodes for large bias voltages.

The main aspect of this whole project was to fabricate a working prototype of the schematic measurement structure shown in Figure 4. There were many technical difficulties in the fabrication process and they will be discussed later in this thesis.

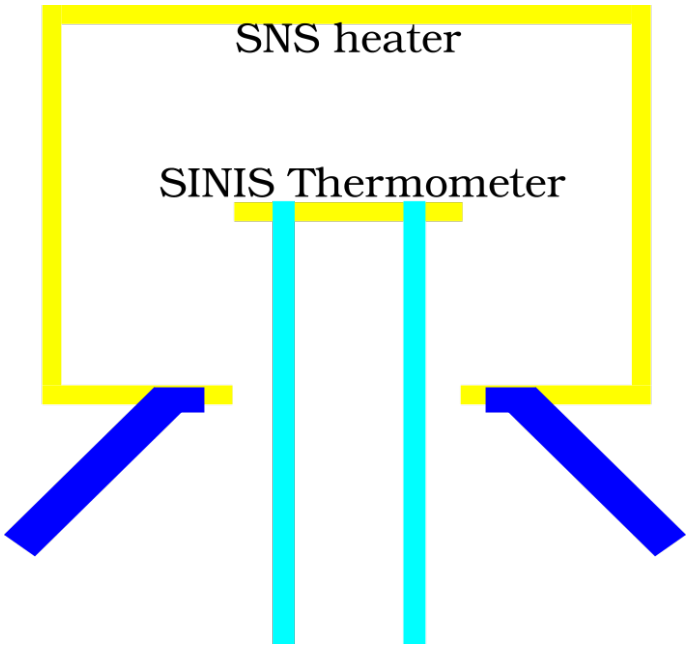

Figure 4. Schematic representation of the heater and thermometer geometries. Different colors represent different materials; blue is Nb, yellow is TiAu bilayer and cyan is Al.

2 Theory

This section shines light on basic theory of superconductivity, superconducting boundary effects. Special care is taken in explaining heat transfer at low temperatures. Some calculations are also performed to justify different approximations. Considerations of different phenomena related to phonons and superconductivity are made to get a grasp of magnitudes that these effects might have during the experiment.

2.1 A short introduction to superconductivity

Heike Kamerlingh Onnes found superconductivity in 1911 in Leiden [23]. He used a helium cryostat to cool down gold and mercury wires. While the experiment with gold didn't give an indication of superconductivity, the one with mercury showed vanishing resistance at 4.19 K [23]. The point where the resistance vanishes is called critical temperature T_c.

Another phenomenon linked to superconductivity is the Meissner effect. It was found by W. Meissner and R. Ochsenfeld in 1933 [24]. The effect is observed as perfect diamagnetism in the superconducting state. This discovery led to a conclusion that the superconducting state can be destroyed by applying strong enough external critical magnetic field H_c. Critical magnetic field's temperature dependence can be approximated by equation

$$H_\mathrm{c}(T) \approx H_\mathrm{c}(0)\left[1-\left(\frac{T}{T_\mathrm{c}}\right)^2\right], \tag{1}$$

where $H_\mathrm{c}(0)$ is critical magnetic field at 0 K, T_c is the critical temperature and T is temperature [25]. Magnetic fields below H_c can penetrate the superconductor's surface to a depth

$$\lambda_\mathrm{L}(0) = \sqrt{\frac{m}{\mu_0 n e^2}}, \tag{2}$$

where m is the electron mass, n is the electron density and e is the electron charge. Equation (2) is called London penetration depth and it is only valid for pure materials with local electrodynamic response at $T << T_\mathrm{c}$. If a two fluid model developed by Gorter and Casimir [26] is applied, one can get temperature dependence

$$\lambda(T) = \lambda(0)\frac{1}{\sqrt{1-t^4}}. \tag{3}$$

where $t = T/T_c$ is known as the reduced temperature.

Let's then consider the wave properties of Cooper pairs. Pippard's non-local electrodynamics suggest that the coherence length of a Cooper pair is

$$\frac{1}{\xi} = \frac{1}{\xi_o} + \frac{1}{l} \tag{4}$$

where l is mean free path and

$$\xi_0 = a\frac{\hbar v_F}{k_B T_c}, \tag{5}$$

where a is a numerical constant that was proved to be 0.18 by the BCS theory and v_F is the Fermi velocity. ξ_0 is often called the intrinsic coherence length. Pippard's coherence length describes the length scale of non-locality in the electrodynamic response, or in other words, the smallest size of a wave packet that Cooper pairs can form.

Ginzburg-Landau (GL) coherence length describes the characteristic length scale over which the superconducting order parameter can vary and it is not same as obtained from Pippard's non-local theory

$$\xi(T) = \frac{\hbar}{|4m\alpha(T)|^{1/2}}. \tag{6}$$

Here m is the electron mass and

$$\alpha(T) = -\frac{2e^2}{m}\mu_0^2 H_c^2(T)\lambda_{\text{eff}}^2(T). \tag{7}$$

λ_{eff} varies depending on the superconductor. For a clean local superconductor ($\xi_0 << l, \lambda$) $\lambda_{\text{eff}} = \lambda_L$, for dirty ($l << \xi_0$) superconductors $\lambda_{\text{eff}}^2 = \lambda_L^2 \xi_0/l$, and for non-local ($\xi_0 >> \lambda$) superconductors $\lambda_{\text{eff}} = (\lambda_L^2 \xi_0)^{1/3}$.

In 1957 J. Bardeen, L. N. Cooper and J. R. Schrieffer published their famous microscopic theory of superconductivity (commonly known as the BCS theory). The BCS theory was able to explain both phenomena described above [27]. The theory predicts that it takes an energy of 2Δ to break a Cooper pair and thus create a pair of excitations. This means that there is an energy gap Δ between the superconducting state and the excited state. The BCS temperature dependence of $\Delta(T)$ can be calculated from [28]

$$-\ln\frac{T}{T_c} = \int_0^\infty \left[\frac{\tanh(\varepsilon')}{\varepsilon'} - \frac{\tanh\sqrt{\left(\varepsilon'^2 + \left(\frac{1.764\Delta(T)/\Delta(0)}{(T/T_c)}\right)^2\right)}}{\sqrt{\varepsilon'^2 + \left(\frac{1.764\Delta(T)/\Delta(0)}{(T/T_c)}\right)^2}}\right] \mathrm{d}\varepsilon'. \tag{8}$$

Around $T = T_c$, equation (8) can be approximated as

$$\frac{\Delta(T)}{\Delta(0)} \approx 1.74\sqrt{1 - \frac{T}{T_c}}, \tag{9}$$

where the gap at zero temperature is defined as

$$2\Delta(0) = 3.528 k_{\mathrm{B}} T_{\mathrm{c}} \tag{10}$$

According to the BCS theory the density of states of excitations of ''quasiparticles'' in the superconducting state is

$$N_{\mathrm{s}}(E) = \frac{E}{\sqrt{E^2 - \Delta^2(T)}} \tag{11}$$

with the restriction for energy $|E| > \Delta$, where the energy E of the excitation is measured from the Fermi level E_{F}. This means that there are no states below the gap. For the quasiparticle excitations in the superconductor we have for their energy

$$E_k = \sqrt{\Delta^2 + \varepsilon_k^2}, \tag{12}$$

where

$$\varepsilon_k = \frac{\hbar^2 k^2}{2m} - E_{\mathrm{F}}. \tag{13}$$

Here ε_k can be identified as the electron energy with the wave vector k measured from the Fermi level. From equation 12 it can be seen that quasiparticle excitations in superconductors are forced to have energy of at least $|E_k| = \Delta$.

For Bogoliubov formalism the BCS theory also defines so called coherence factors

$$u_k^2 = 1 - v_k^2 = \frac{1}{2}\left(1 + \frac{\varepsilon_k}{E_k}\right). \tag{14}$$

Physically, these factors give a probability $|u_k|^2$ that a Cooper pair state (k,-k) is occupied and $|v_k|^2$ that an Cooper pair state (k,-k) is unoccupied. They are also required to fulfill the normalization condition $|u_k|^2 + |v_k|^2 = 1$.

2.2 Andreev reflection

In 1965 Alexander Andreev found an explanation to a problem, where a superconductor is put in an intermediate state using an external magnetic field [29]. The observation was that the superconductor had a lower thermal conductivity than in purely superconducting state. The reasoning was the following: Assuming if the intermediate state is formed by applying a magnetic field perpendicular to the superconductor's surface, the intermediate state consists of normal and superconducting parts. It turns out that the normal areas are typically filaments or lamella along the external field direction [25]. If it's further assumed that the temperature of the superconductor is well below the critical temperature, so that the main contribution to thermal conductivity is from quasiparticle excitations. To carry heat, these excitations must then travel through the normal and superconducting regions even when the excitation energy is lower than the superconducting gap [30, 31]. This

is only possible if the superconducting regions are of the scale ξ, as quasiparticles entering the superconductor below Δ are at evanescent states within the gap and decay into the condensate within the Cooper pair coherence length $\xi(T)$ [25].

Let's measure the quasiparticle excitation energy ε_k from the Fermi level, just like was shown in equation (13) and consider an incident excitation from the normal metal toward the superconductor in an NS interface. Now when the incident excitation from the normal state is a hole we have energy $\varepsilon_k < 0$, whereas for electron-like excitations we have $\varepsilon_k > 0$. There are then different interface processes depending on the energy and the interface quality. The most interesting one is the superconducting Andreev reflection, where incoming electron (hole) backscatters as a hole (electron) and transmits a Cooper pair into the superconductor. Blonder et al [32] calculated the transmission and reflection coefficients for all different processes taking place at the NS interface. The coefficients describe Andreev reflection A, ordinary reflection B and quasiparticle transmissions without and with branch crossing C and D. They also introduced a dimensionless barrier strength factor Z, that describes how ideal the NS interface is. This allows the expression of all coefficient with BCS coherence factors u, v and the barrier strength factor, reducing all factors to a very simple equations.

The simplest case is where $|\varepsilon_k| < \Delta$ and there is no barrier $Z = 0$. Then we get an Andreev reflection coefficient $A = 1$ and all others are 0. For $|\varepsilon_k| > \Delta$, the Andreev reflection coefficient vanishes as a function of ε_k, and transmission without a branch crossing gets a coefficient $C = 1 - A$, see figure 5. The coefficient table for the general case with $Z \neq 0$ can be found in [32].

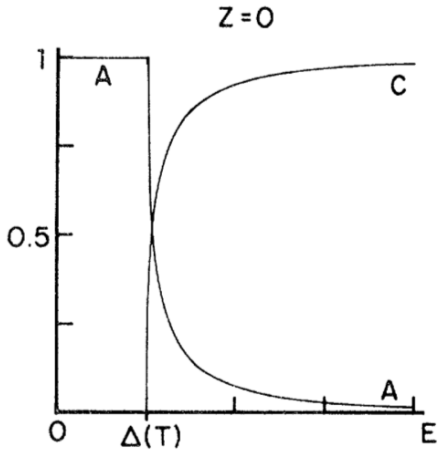

Figure 5. Andreev reflection coefficient A and transmission without branch crossing coefficient C as a function of quasiparticle excitation energy ε_k. The barrier strength factor is $Z = 0$, so A, C are the only possible processes [32].

2.3 Proximity effect

The proximity effect is a phenomenon that is related to the Andreev reflection, which gives rise to quasiparticles entering the superconductor with energies below the superconducting gap. This can be observed as a change in properties of the superconductor and the normal metal. The proximity effect at NS interfaces is interesting, because it can be used as T_c modifier if the superconducting transition needs to be tuned to some specific value. Some unwanted effects can be observed with NS bilayers, as well. Thus, theoretical understanding of these processes is important for experimentalists too.

The proximity effect stems from the superconducting order parameter that doesn't vanish right at the interface but decays exponentially into the normal metal. The normal metal also affects the order parameter on the superconducting side of the interface.

The proximity effect can be described by so called Usadel equations. The Usadel equations are used for describing the superconducting state function $\Theta(x, E)$ and spatially dependent complex order parameter $\Delta(x)$. They are complex valued, with amplitudes 0 and $\pi/2$ for Θ corresponding to the normal state and the BCS superconducting state respectively [33]. In 1D case the Usadel equations are given as

$$\frac{\hbar D_\mathrm{s}}{2}\frac{\partial^2\Theta}{\partial x^2}+iE\sin\Theta-\left[\frac{\hbar}{\tau_\mathrm{sf}}+\frac{\hbar D_\mathrm{s}}{2}\left(\frac{\partial\varphi}{\partial x}+\frac{2e}{\hbar}A_x\right)^2\right]\cos\Theta\sin\Theta+\Delta(x)\cos\Theta=0 \quad (15)$$

and

$$\Delta(x)=n_s V_\mathrm{eff}\int_0^{\hbar\omega_\mathrm{D}}\mathrm{d}E\tanh\left(E/2k_\mathrm{B}T\right)\mathrm{Im}[\sin\Theta]e^{i\varphi(x)}, \quad (16)$$

where D_s is the diffusion constant, n_s is the normal state density of states of the superconductor, V_eff is the pairing interaction potential, τ_sf is the spin-flip time, φ is the superconducting phase, A_x is the vector potential component along x axis, Δ is the superconducting order parameter $\hbar\omega_\mathrm{D}$ is the Debye energy and T is the temperature.

Solving equations (15,16) for a thin NS bilayer one can get modified T_c of the form

$$T_\mathrm{c}=T_\mathrm{c0}\left[\frac{d_s}{d_0}\frac{1}{1.13(1+1/\alpha)}\frac{1}{t}\right]^\alpha \quad (17)$$

where T_c0 is the critical temperature of bare superconductor, d_s is the thickness of the superconductor and t is a free parameter called the transmission factor [34]. The other symbols are defined as

$$\frac{1}{d_0}=\frac{\pi}{2}k_\mathrm{B}T_\mathrm{c0}\lambda_\mathrm{F}^2 n_\mathrm{s} \quad (18)$$

$$\alpha=\frac{d_\mathrm{n}n_\mathrm{n}}{d_\mathrm{s}n_\mathrm{s}}, \quad (19)$$

where n_n, n_s are the densities of states for the normal metal and the superconductor in normal state, λ_F is the Fermi wavelength of the normal metal and d_n is the normal metal thickness.

2.4 SNS junction

SNS junctions that are typically studied for example in [35] or characterized have a relatively small normal metal island between the superconducting leads compared to the heater element used in this thesis. Another typical SNS structure is a thin normal metal slab sandwiched between superconducting leads. We can approximate the length scale of the proximity effect by thermal coherence length of the Au layer given by [36], [37]

$$\xi_\mathrm{N} = \sqrt{\frac{\hbar D}{2\pi k_\mathrm{B} T}}, \tag{20}$$

where D is the diffusion constant given by

$$D = \frac{1}{\rho N(E_\mathrm{F}) e^2}. \tag{21}$$

$N(E_\mathrm{F})$ is the density of states at the Fermi level and we can use the free electron model to estimate it

$$N(E_\mathrm{F}) = \frac{(2m)^{3/2}}{2\pi^2\hbar^3} E_\mathrm{F}^{1/2}, \tag{22}$$

where m is the mass of the electron. Let's then approximate the coherence length of a gold weak link between niobium electrodes. We need the resistivity of gold to get a value for the diffusion constant. It appears that the resistivity of gold doesn't change much in the temperature range of 1 K to 10 K according to [38] and we shall use a value of $\rho = 0.022 \cdot 10^{-8}\Omega\mathrm{cm}$. We find from [39] $E_\mathrm{F,Au} = 5.53\,\mathrm{eV}$, and by substituting equation (21) to equation (20) we get at $T = 0.1$ K for the coherence length $\xi \approx 55$ nm. To get a better grasp of how the coherence length acts with temperature, see Figure 6.

The heater element length is roughly 32 μm, so Cooper pairs can not carry supercurrent over the SNS junction used here. Thus we get Joule heating in the normal metal lead without supercurrent effects. Of course there can be Cooper pairs present inside the normal metal near the superconductor as suggested by theories presented above, but this effect should be negligible in the application used here.

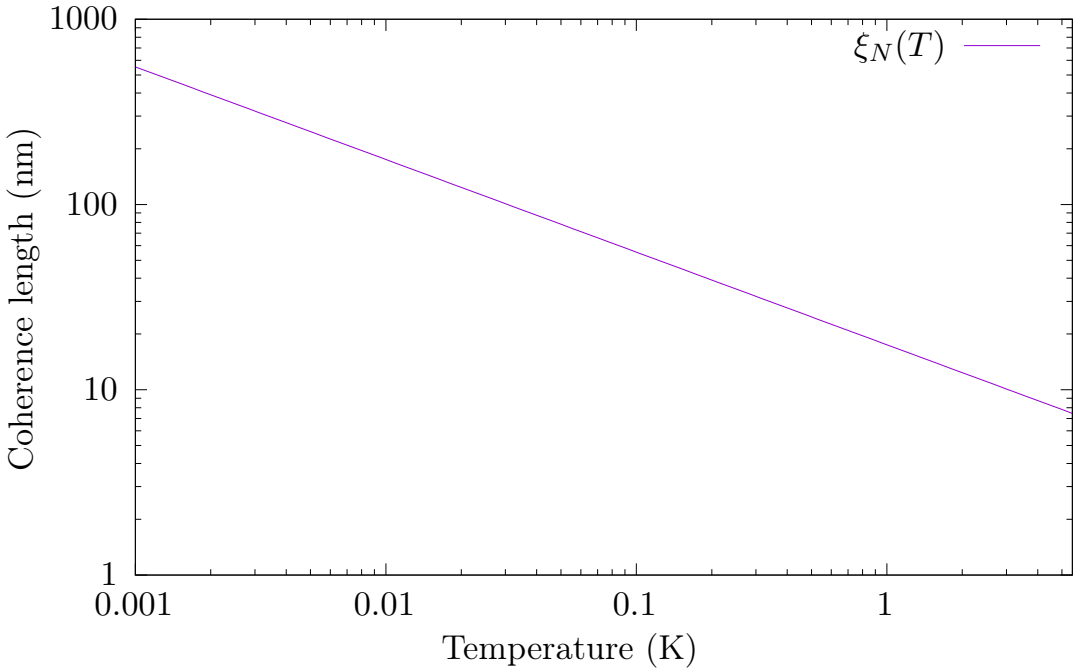

Figure 6. The coherence length of a gold weak link between niobium electrodes. It was assumed, that Nb has T_c of 5.5 K.

2.5 SINIS thermometry

Current through a symmetric SINIS junction can be derived from the BCS theory using the Fermi golden rule [25]. The resulting equation reads

$$I = \frac{1}{2eR_T}\int_{-\infty}^{\infty} \mathrm{d}E\, N_S(E,T_S)[f_N(E-eV,T_N) - f_N(E+eV,T_N)], \tag{23}$$

where R_T is the tunneling resistance of single junction, E is the energy, eV describes the energy difference of normal metal and superconductor Fermi levels. $2V$ is thus the electric potential difference between the two superconducting wires. f_N is the normal metal Fermi distribution of electrons, and $N_S(E,T_S)$ is the superconducting density of states (DoS)

$$N_S(E,T_S) = \left|\mathrm{Re}\left(\frac{E+i\Gamma'}{\sqrt{(E+i\Gamma')^2-\Delta(T_S)^2}}\right)\right|. \tag{24}$$

This expression is phenomenological and Γ' is called Dynes' parameter, that depicts non-idealities in the superconductor [40]. It's worth noting that as $\Gamma' \to 0$, equation (24) approaches the ideal DoS given in BCS theory. To get a better view of the energy levels that are related to SINIS thermometry, a semiconductor model is shown in Figure 7.

If the current through the SINIS junction is constant and voltage is measured at

different temperatures, we get a voltage-temperature curve. Thus SINIS junctions can be used as thermometers by measuring voltage with a constant current bias.

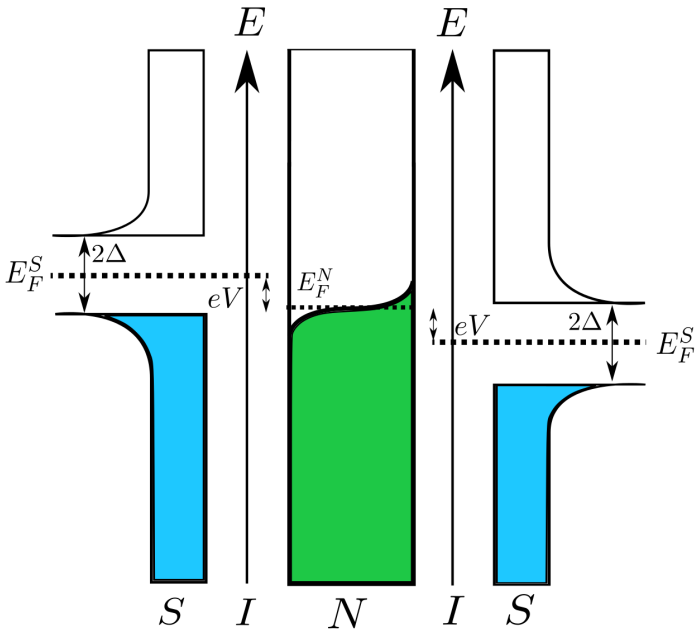

Figure 7. Semiconductor model of a SINIS tunnel junction. E_F^S is Fermi level of the superconductor, E_F^N is Fermi level of normal metal. A constant bias current is driven through the junction pair resulting in temperature dependent voltage $2V$ over the normal metal island.

2.6 Heat conduction at low temperatures

2.6.1 Phonons

Phonons are quasiparticles with particle-and wave-like properties. They are analogous to photons, but instead of being vibrations in electromagnetic field, phonons are vibrations in matter. Phonons can be divided into different regions by frequency.

The thermal average phonon occupation number is given by

$$\langle n \rangle = \frac{1}{\mathrm{e}^{\hbar\omega/k_\mathrm{B}T} - 1}, \tag{25}$$

where ω is the phonon frequency [41]. Phonons can be approximated at low temperatures with the Debye model that assumes linear dispersion relations ($\omega_j = c_j k_j$),

where j represents phonon modes. In 2D, if the dispersion remains linear, the density of states per unit area of phonons is

$$D(\omega)_{\mathrm{2D}} = \frac{\omega}{2\pi}\left(\frac{2}{c_{\mathrm{t}}^2} + \frac{1}{c_{\mathrm{l}}^2}\right), \tag{26}$$

where the speed of sound for two transverse modes c_{t}^2 and one longitudinal one c_{l}^2. Total thermal energy can be calculated from

$$U = \int \mathrm{d}\omega D(\omega)_{\mathrm{2D}} \langle n \rangle \hbar\omega. \tag{27}$$

Then the specific heat is [21]

$$C_V = \frac{\partial U}{\partial T} = \frac{3\zeta(3)k_{\mathrm{B}}^3}{\pi\hbar^2}\left(\frac{2}{c_{\mathrm{t}}^2} + \frac{1}{c_{\mathrm{l}}^2}\right)T^2, \tag{28}$$

assuming isotropic crystal structure.

The dominant phonon wavelength can be derived from the 2D Debye model as the occupation number function has a maximum at $\omega \approx 1.6$ [42]

$$\lambda_{\mathrm{dom}} \approx \frac{h\bar{c}}{1.6k_{\mathrm{B}}T}. \tag{29}$$

For example at 100 mK the dominant phonon wavelength in 300 nm thick SiN with average speed of sound of $\bar{c} = 5800$ m/s is about 1.7 μm.

2.6.2 Diffusive heat transfer

Typical representation of heat transfer assumes that heat flux can only be transferred if there is a gradient of temperature. This type of heat conduction is called diffusive heat transfer. This is analogous to electric current in Ohmic materials, where an electric current only flows in the presence of an electric potential gradient. However, there are also non-Ohmic materials where gradient of electric potential doesn't necessarily put charges in motion. This is for example the case with SINIS junctions. Similarly, the same type of effects can arise with heat transfer too, for example in form of ballistic transfer.

Diffusive heat conduction in solids is typically described by phenomenological Fourier's law

$$\dot{Q} = -\kappa\nabla T \tag{30}$$

where $\dot{Q}$ is heat flux , κ is thermal conductivity and T is temperature. However, this law is no longer valid in cases where scattering processes responsible of κ vanish. This condition can be achieved at low temperatures and, hence, it is not necessary to consider Fourier's law any further in this thesis. It has also been shown that Fourier's law breaks down when the smallest dimensions in nanostructures, ie. PnCs, reach the size of the phonon mean free path [43], [12].

2.6.3 Heat transfer in superconductors

In the superconducting phase the electronic heat transfer is carried by quasiparticle excitations which die out at about $0.2T_c$. Thus, superconductors don't carry electronic heat below $0.2T_c$. The ratio of the electronic specific heat at superconducting state C_{es} and normal state γT_c at $T = T_c$ can be approximated as

$$\frac{C_{es}}{\gamma T_c} \approx 8.5e^{-1.44T_c/T}, \tag{31}$$

where $\gamma = 2/3\pi^2 N(0)k_B^2$ is the Sommerfeld constant and $N(0)$ is the normal density of states at the Fermi surface [27]. This approximation is valid when $\Delta(0)/k_BT >> 1$, and is plotted in Figure 8.

The question remains, whether equation (31) is valid for normal metal coated niobium as used in this thesis. Let's use equation (10) to estimate Nb gap $\Delta(0)_{Nb} \approx 840\,\mu$eV, with a proximized critical temperature $T_c = 5.5$ K that was measured in this thesis. Then calculating at 100 mK or 1 K yields

$$\begin{aligned} \frac{\Delta(0)_{Nb}}{k_BT} &\approx 100 >> 1 \quad T = 100 \text{ mK} \\ &\approx 10 >> 1 \quad T = 1 \text{ K} \end{aligned}$$

Thus we can safely say, that electronic heat conductance at measurement temperatures used here (<1 K) is negligible. Then there is only phononic heat transfer inside the superconductor, and its significance is small because the niobium wire has much smaller area than the SiN membrane.

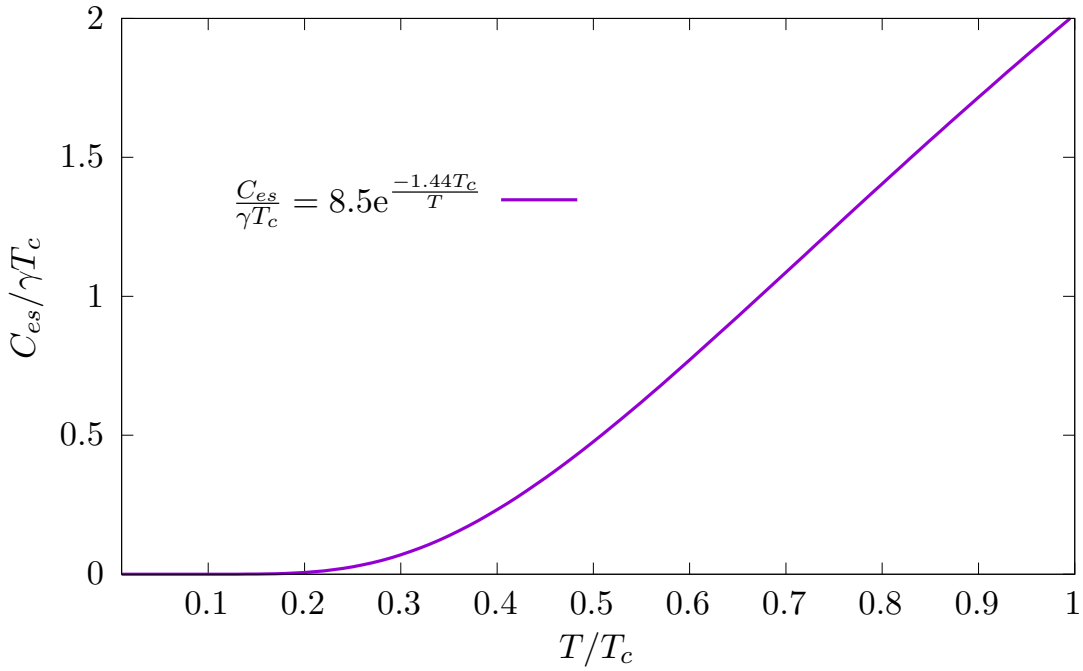

Figure 8. Electronic specific heat of a superconductor vs temperature.

2.6.4 Rayleigh-Lamb theory of elastic waves

To fully understand ballistic conduction in membranes we need to discuss The theory of elasticity for thin membranes of plates. Elastic equations for an isotropic material in cartesian notation are [44]

$$\tau_{ij,j} + \rho f_i = \rho \ddot{u}_i \tag{32}$$
$$\tau_{ij} = \lambda \varepsilon_{kk} \delta_{ij} + 2\mu \varepsilon_{ij} \tag{33}$$
$$\varepsilon_{ij} = 1/2(u_{i,j} + u_{j,i}) \tag{34}$$
$$\omega_{ij} = 1/2(u_{i,j} - u_{j,i}), \tag{35}$$

where λ and μ are the Lamé constants, ρ is the density of the membrane and $\vec{f}$ is the body force per unit mass, u_i is the displacement vector and τ_{ij}, ε_{ij}, ω_{ij} are the tensors for stress, strain and rotation, respectively. The Lamé constants are the only two independent elastic stiffness coefficients for an isotropic material [45]. The comma notation here means differentiation E

$$u_{i,j} = \frac{\partial u_i}{\partial x_j}.$$

Regrouping the elastic equations and switching to vector notation, we obtain the equation for the displacement vector $\vec{u}$, that appears to be Navier's equation

$$(\lambda + \mu)\nabla\nabla \cdot \vec{u} + \mu\nabla^2\vec{u} + \rho\vec{f} = \rho\frac{\partial^2\vec{u}}{\partial t^2}. \tag{36}$$

Continuing this treatment for solving the displacement in three dimensions would result to very complex set of equations. To avoid this, we can define scalar and vector potentials Φ and $\vec{H}$ so that the displacement vector is

$$\vec{u} = \nabla\Phi + \nabla \times \vec{H} \tag{37}$$

with a gauge choice

$$\nabla \cdot \vec{H} = 0. \tag{38}$$

We can also express the force $\vec{f}$ in equation (36) with scalar and vector fields

$$\vec{f} = \nabla f + \nabla \times \vec{B}, \quad \nabla \cdot \vec{B} = 0. \tag{39}$$

Now substituting equations (37, 38, 39) into equation (36) and using a well known vector calculus result for any vector $\vec{a}$ $\nabla \times (\nabla \times \vec{a}) = \nabla(\nabla \cdot \vec{a}) - \nabla^2\vec{a}$ we get

$$\nabla\left[(\lambda + 2\mu)\nabla^2\Phi + \rho f - \rho\frac{\partial^2\Phi}{\partial t^2}\right] + \nabla \times \left[\mu\nabla^2\vec{H} + \rho\vec{B} - \rho\frac{\partial^2\vec{H}}{\partial t^2}\right] = 0. \tag{40}$$

The result (40) is true when both terms inside square brackets equal zero, thus we have two equations, one for the scalar potential and the other for the vector potential

$$(\lambda + 2\mu)\nabla^2\Phi + \rho f = \rho\frac{\partial^2\Phi}{\partial t^2} \tag{41}$$

$$\mu\nabla^2\vec{H} + \rho\vec{B} = \rho\frac{\partial^2\vec{H}}{\partial t^2} \tag{42}$$

In the absence of driving forces, equations (41, 42) take the form of classic wave equations

$$\nabla^2\Phi = \frac{\rho}{\lambda + 2\mu}\frac{\partial^2\Phi}{\partial t^2} \tag{43}$$

$$\nabla^2\vec{H} = \frac{\rho}{\mu}\frac{\partial^2\vec{H}}{\partial t^2}. \tag{44}$$

Now we can identify the speeds of sound for longitudinal and transverse modes as

$$c_\mathrm{l} = \sqrt{\frac{\lambda + 2\mu}{\rho}} \tag{45}$$

$$c_\mathrm{t} = \sqrt{\frac{\mu}{\rho}}. \tag{46}$$

Now let's consider a plate that lies in x, z plane and has a thickness d so that the surfaces of the plate are at $y = \pm d/2$. If we study only the shear mode (h), we can choose for the displacement to occur only in z direction. Then in the absence of external forces we can extract a simple wave equation for the displacement from equation (36)

$$\nabla^2 u_z = \frac{1}{c_\mathrm{t}^2}\frac{\partial^2 u_z}{\partial t^2}. \tag{47}$$

Next we use an ansatz of the form

$$u_z = h(y)\mathrm{e}^{i(k_x x - \omega t)}, \tag{48}$$

where we assumed wave propagation along x-axis, but we might choose the propagation along the z-axis as well. The result of this change would only switch x components to z components and vice versa in equation (48). Substituting eq. (48) in eq. (47) results in another differential equation for the function $h(y)$

$$\frac{\mathrm{d}^2 h(y)}{\mathrm{d}y^2} + (\omega^2/c_\mathrm{t}^2 - k_x^2)h(y) = 0, \tag{49}$$

which has a solution

$$h(y) = A_1 \sin\Big(\sqrt{\omega^2/c_\mathrm{t}^2 - k_x^2}\, y\Big) + A_2 \cos\Big(\sqrt{\omega^2/c_\mathrm{t}^2 - k_x^2}\, y\Big). \tag{50}$$

Inserting eq. (50) back in the ansatz (48) yields the solution for the displacement

$$u_z = \left[A_1 \sin\left(\sqrt{\omega^2/c_\mathrm{t}^2 - k_x^2}\, y\right) + A_2 \cos\left(\sqrt{\omega^2/c_\mathrm{t}^2 - k_x^2}\, y\right)\right] \mathrm{e}^{i(k_x x - \omega t)}. \tag{51}$$

By applying the free boundary conditions $\partial u_z/\partial y = 0$ at the membrane surfaces at $y = \pm d/2$, we get a set of two equations

$$A_1 \cos\left(\sqrt{\omega^2/c_\mathrm{t}^2 - k_x^2}\, d/2\right) - A_2 \sin\left(\sqrt{\omega^2/c_\mathrm{t}^2 - k_x^2}\, d/2\right) = 0 \tag{52}$$

$$A_1 \cos\left(\sqrt{\omega^2/c_\mathrm{t}^2 - k_x^2}\, d/2\right) + A_2 \sin\left(\sqrt{\omega^2/c_\mathrm{t}^2 - k_x^2}\, d/2\right) = 0. \tag{53}$$

These secular equations have a solution when the determinant vanishes, so we get

$$\cos\left(\sqrt{\omega^2/c_\mathrm{t}^2 - k_x^2}\, d/2\right) \sin\left(\sqrt{\omega^2/c_\mathrm{t}^2 - k_x^2}\, d/2\right) = 0, \tag{54}$$

which has solutions when

$$\sqrt{\frac{\omega^2}{c_\mathrm{t}^2} - k_x^2}\, \frac{d}{2} = \frac{n\pi}{2}, \tag{55}$$

where $n = 0, 1, 2, 3, 4, \cdots$. Solving for the frequency yields

$$\omega_{h,n} = c_\mathrm{t}^2 \left[\left(\frac{n\pi}{d}\right)^2 + k_{||}^2\right], \tag{56}$$

where we used $k_x \to k_{||}$ to generalize the solution to cover all the shear waves that propagate parallel to the membrane surface, but also have displacement parallel to the membrane surface, but perpendicular to the propagation direction. This can be done, since the same result could be derived for all k directions, it is only a matter of coordinate choice.

Next we'll take a look at the two remaining wave modes, that are called symmetric (s) and antisymmetric (a) Lamb modes. This time the wave modes affect the surface shape. In case of shear modes we banned displacement in y direction, but with (s) and (a) modes displacement component in y is allowed too.

Now the derivation for the equations for the frequency are a bit more involved, because there is displacement in two directions. However, methods and solutions for differential equations follow the same logic as with the shear modes. For this reason, we'll omit the derivation of displacement and stress functions. Stresses τ_{yy} and τ_{xy} are used for finding the frequency equations for a and s modes

$$\begin{aligned}\tau_{yy} = \mu \Big[&\left(k_{||}^2 - (k_\perp^\mathrm{t})^2\right)\left(A \sin\left(k_\perp^\mathrm{l} y\right) + B \cos\left(k_\perp^\mathrm{l} y\right)\right) \\ &+ 2k_\perp^\mathrm{t} k_{||} \left(C \cos\left(k_\perp^\mathrm{t} y\right) - D \sin\left(k_\perp^\mathrm{t} y\right)\right)\Big] \mathrm{e}^{i(k_{||} x - \omega t)}\end{aligned} \tag{57}$$

$$\begin{aligned}\tau_{xy} = i\mu \Big[&2k_\perp^\mathrm{l} k_{||} \left(A \cos\left(k_\perp^\mathrm{l} y\right) - B \sin\left(k_\perp^\mathrm{l} y\right)\right) \\ &- \left((k_\perp^\mathrm{t})^2 - k_{||}^2\right)\left(C \sin\left(k_\perp^\mathrm{t} y\right) + D \cos\left(k_\perp^\mathrm{t} y\right)\right)\Big] \mathrm{e}^{i(k_{||} x - \omega t)}.\end{aligned} \tag{58}$$

Here constants A and D are responsible for the antisymmetric (a) mode and B and C count for the symmetric (s) mode, $k_{||}$ is the parallel component of the wave vector, and $k_{\perp}^{\mathrm{t}}$ and $k_{\perp}^{\mathrm{l}}$ are the transverse and longitudinal wave number components perpendicular to the membrane surfaces, respectively [46].

Applying free boundaries ($\tau_{yy} = \tau_{xy} = 0$, $y = \pm d/2$) and setting $A = D = 0$ to stress equations (57) and (58) yields

$$(k_{||}^2 - (k_{\perp}^{\mathrm{t}})^2)B\cos\Big(k_{\perp}^{\mathrm{l}}d/2\Big) + 2k_{||}k_{\perp}^{\mathrm{t}}C\cos\Big(k_{\perp}^{\mathrm{t}}d/2\Big) = 0 \tag{59}$$

$$\pm i\left(-2k_{|||}k_{\perp}^{l}B\sin\Big(k_{\perp}^{\mathrm{l}}d/2\Big) + (k_{||}^2 - (k_{\perp}^{\mathrm{t}})^2)C\sin\Big(k_{\perp}^{\mathrm{t}}d/2\Big)\right) = 0 \tag{60}$$

for the s mode. Requiring a vanishing determinant for the characteristic equations, we obtain a transcendental equation for the frequency

$$\frac{\tan\left(\frac{d}{2}k_{\perp}^{\mathrm{t}}\right)}{\tan\left(\frac{d}{2}k_{\perp}^{\mathrm{l}}\right)} = -\frac{4k_{\perp}^{\mathrm{t}}k_{\perp}^{\mathrm{l}}k_{||}^2}{\Big((k_{\perp}^{\mathrm{t}})^2 - k_{||}^2\Big)^2}. \tag{61}$$

It is important to note that $\omega^2 = c_t^2(k_{\perp}^{\mathrm{t}})^2 = c_l^2(k_{\perp}^{\mathrm{l}})^2$.

By applying the same boundary conditions as in previous case, but setting $C = D = 0$ to equations (57) and (58), we get the frequency equation for the a mode

$$\frac{\tan\left(\frac{d}{2}k_{\perp}^{\mathrm{l}}\right)}{\tan\left(\frac{d}{2}k_{\perp}^{\mathrm{t}}\right)} = -\frac{4k_{\perp}^{\mathrm{t}}k_{\perp}^{\mathrm{l}}k_{||}^2}{[(k_{\perp}^{t})^2 - k_{||}^2]^2}. \tag{62}$$

Again the resulting equation is transcendental, so no analytical solutions are available. However, the lowest modes can be calculated by using low energy expansions for s and a modes. The expansions are presented in detail in [47]. For the h mode we just set $n = 0$ in equation (56) to get the lowest mode. Finally, the dispersion relations for the lowest modes are written as

$$\begin{aligned}
\omega_{h,0} &= c_{\mathrm{t}}k_{||} \\
\omega_{s,0} &= \frac{2c_{\mathrm{t}}}{c_{\mathrm{l}}}\sqrt{c_{\mathrm{l}}^2 - c_{\mathrm{t}}^2}k_{||} = c_{\mathrm{s}}k_{||} \\
\omega_{a,0} &= \frac{\hbar}{2m^*}k_{||}^2.
\end{aligned}$$

An assumption of small $k_{||}$ was made, so that $k_{||}d << 1$. Here c_{s} is the speed of sound of the symmetric Lamb mode and m^* is the effective mass of the antisymmetric Lamb mode given by [46]

$$m^* = \frac{\hbar}{2c_{\mathrm{t}}d\sqrt{c_{\mathrm{l}}^2 - c_{\mathrm{t}}^2/3c_{\mathrm{l}}^2}}. \tag{63}$$

The lowest phonon mode dispersion relations are plotted in Figure 9.

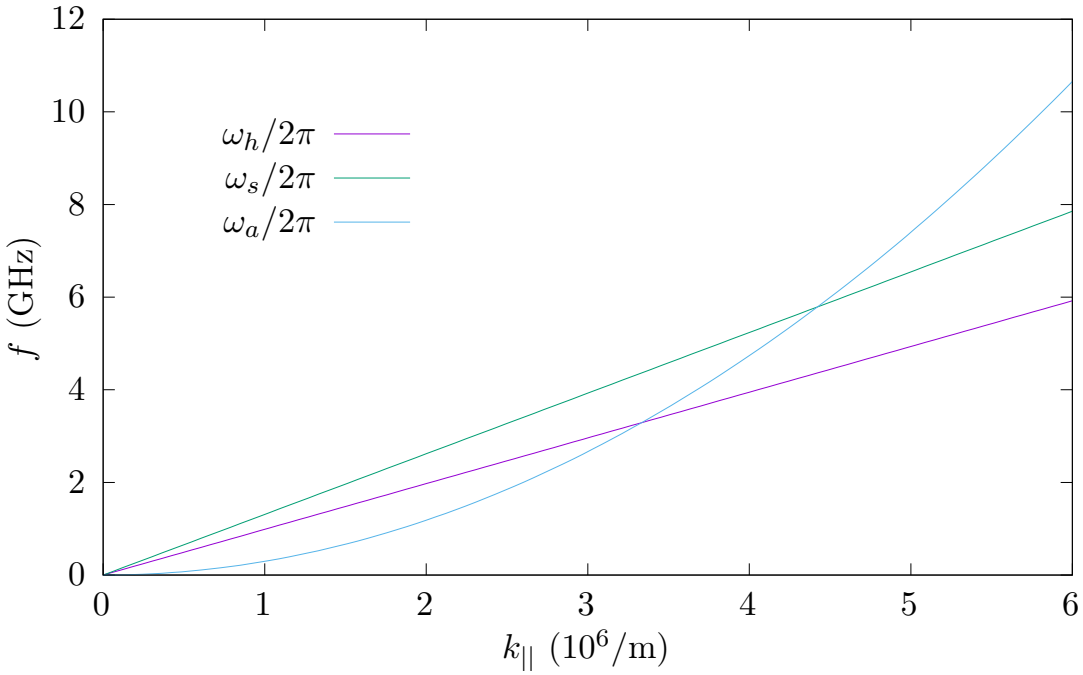

Figure 9. Dispersion relations of lowest phonon modes. a mode is valid only with small $k_{||}$, so that $k||d << 1$.

2.6.5 Heat conduction in dielectric membranes

A thin dielectric membrane is realized as 300 nm thick SiN membrane in this thesis. That is definitely a 3D object, but low enough temperatures combined with spatial constriction (thinness) results in quasi-2D behavior of phonons. It has been observed in many studies that at sub-Kelvin temperatures phonons can transmit ballistically, ie. they don't scatter from each other or from impurities [22, 48]. There could still be surface scattering at the membrane edges and top and bottom surfaces, and the type of surface scattering highly depends on the surface roughness of the membrane. If the surface is smooth enough the scattering is specular, but the scattering can be diffusive from rough surfaces. A crude estimate of the proportion of specular and scattering has been given by Ziman [42]:

$$p(\lambda) = \mathrm{e}^{-\frac{16\pi^3\eta^2}{\lambda^2}}. \tag{64}$$

Here η represents the rms deviation of the surface height and λ is the phonon wavelength. Figure 10 presents the allowed surface roughness for dominant phonons at 100 mK and at 1 K in SiN. Typical SiN membrane surface roughness is 0.65± 0.06 nm for commercial SiN membranes obtained by transmission electron microscopy [49]. This implies that if the membrane used in the experiment is of the same quality as Ted Pella Inc promises, we should expect mostly specular surface scattering below 1 K temperatures. However, there can be some residual matter left on top of the membrane from the fabrication processes. These impurities can affect the surface

scattering at some points on the membrane.

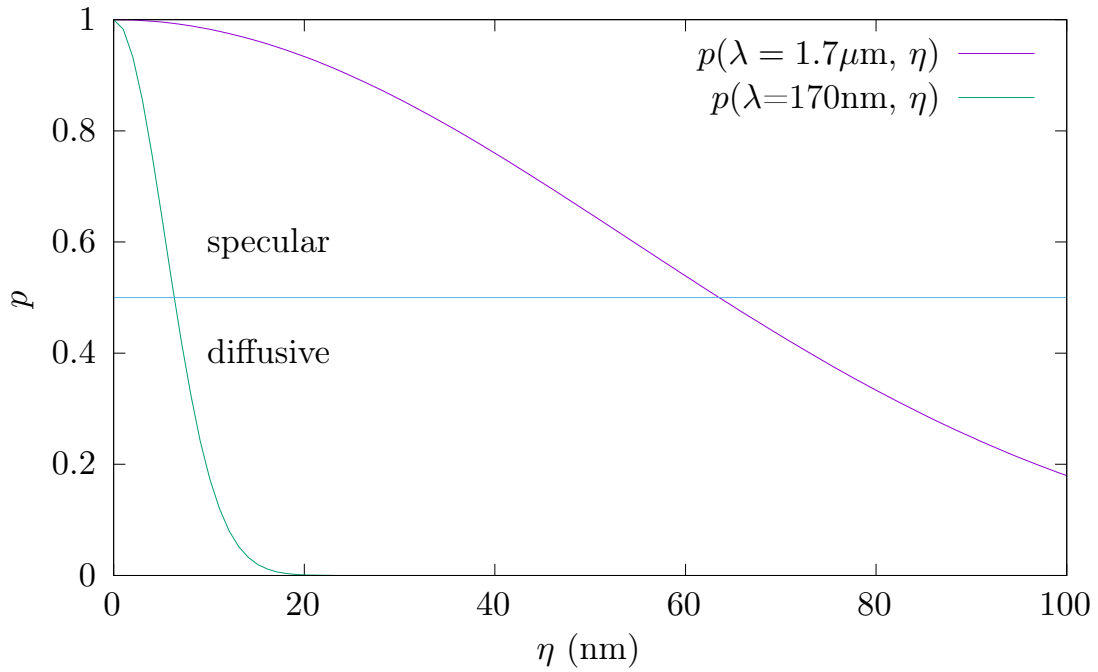

Figure 10. Proportion of specular surface scattering as a function of rms surface roughness is presented with the dominant phonon wavelengths at 1 K (170 nm) and at 100 mK (1.7 μm), calculated for SiN using equation (29) with average speed of sound $\bar{c} = 5800$ m/s.

There is a relation between the temperature and the membrane thickness that describes a cross-over point where the phonons cross from 3D to 2D gas. The cross-over temperature can be calculated from

$$T_c = \frac{\hbar c_\mathrm{t}}{2k_\mathrm{B}d}, \tag{65}$$

where c_t is transverse speed of sound [46, 47]. If membrane thickness is $d = 300$ nm and $c_t = 6200$ m/s we get $T_c \approx 80$ mK. All heating experiments conducted in this thesis went above this value. Thus the measurements should show both 3D and 2D phonon gas regimes, towards the 3D case. This is confirmed by the measurement results, by observing a power law exponent $n = 3.8$ that is nearly the expected 3D value $n_\mathrm{3D} = 4$.

The heater phonon radiation power can be calculated for the quasi-2D case from [12]

$$P(T) = \frac{1}{(2\pi)^2}\sum_j \oint_l \mathrm{d}l \int_K \mathrm{d}\vec{k}\hbar\omega_j(\vec{k})n(\omega_j,T)\frac{\partial\omega_j(\vec{k})}{\partial\vec{k}}\cdot\hat{n}_l\Theta\left(\frac{\partial\omega_j}{\partial\vec{k}}\cdot\hat{n}_l\right), \tag{66}$$

where Θ is the Heaviside step function and $\hat{n}_l$ is the 2D heater surface normal, ie. a vector in the plane of the membrane. For PnC structures, a finite element method

(FEM) simulation is needed to resolve the dispersion relations $\omega(\vec{k})$. l describes the heater boundary, n is the Bose occupation factor. See Figure 11 for a fuller view of the dispersion relations used in the simulations.

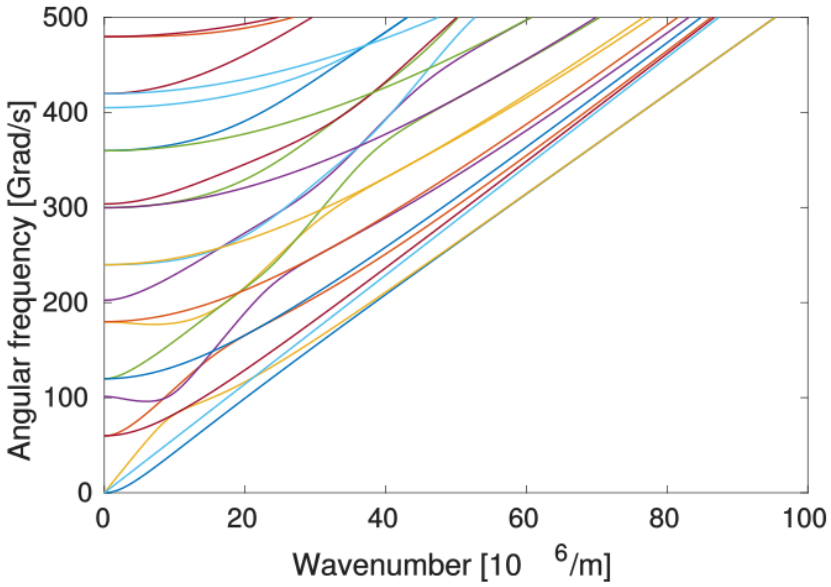

Figure 11. Dispersion relations for 300 nm thick SiN membrane. The figure was kindly produced by Dr. Tuomas Puurtinen.

Using equation (66) with the Rayleigh-Lamb modes discussed earlier, we get a result for the uncut membrane in the low T ($T << T_c$) 2D limit

$$P_{2D} = \frac{l\hbar}{2\pi^2}\left[\left(\frac{1}{c_t}+\frac{1}{c_s}\right)\Gamma(3)\zeta(3)\left(\frac{k_B T}{\hbar}\right)^3 + \sqrt{\frac{2m^*}{\hbar}}\Gamma(5/2)\zeta(5/2)\left(\frac{k_B T}{\hbar}\right)^{5/2}\right]. \quad (67)$$

Here l is the heater boundary length and Γ is the gamma function. Taking a closer look at equation (67) we notice that at the lowest temperatures the first term vanishes first and thus $P \propto T^{5/2}$.

2.6.6 Geometrical considerations of the radiation law

Geometries of the heating element and the receiving element (the thermometer) have a big effect on transmitted heat power. This can be seen by studying the view factor F_{ij} that is the fraction of the radiation emitted by surface i and absorbed by surface j. The view factor can be calculated from

$$F_{ij} = \frac{1}{A_i}\int_{A_i} \mathrm{d}A_i \int_{A_j} \mathrm{d}A_j \frac{\cos(\theta_i)\cos(\theta_j)}{\pi d^2}, \quad (68)$$

where A_i is the area of the emitting surface, A_j is the area of the absorbing surface, θ_i is the angle between the normal of the infinitesimal surface $\mathrm{d}A_i$ and the line

connecting $\mathrm{d}A_i$ and $\mathrm{d}A_j$, and d is the length of the area connecting line. Calculation of the view factor for the geometry used here seems a bit too complicated to be done analytically. Numerical approach would be the way to go here, but rigorous analysis of the matter would take considerable amount of time, so let's leave that job for the future.

A reciprocity relation for the view factors is defined as

$$A_i F_{ij} = A_j F_{ji}. \tag{69}$$

This allows one to calculate the view factor F_{ij} if F_{ji} is already known.

If a surface is enclosed, a summation rule can be derived from the view factor definition

$$\sum_{j=1}^{N} F_{ij} = 1. \tag{70}$$

There are N subsurfaces radiating and all sum to one if whole surface is enclosed. We also have for convex surfaces a rule that $F_{jj} = 0$ [50]. In a 2D case areas A reduce to lengths L.

2.6.7 Heat flow at material interfaces

There are a few mechanisms that can affect the coupling of electronic temperature of the normal metal and the phononic temperature of the SiN membrane. At low temperatures electrons and phonons in the metal can decouple thermally, leading to a difference in phononic and electronic temperatures within the metal. This phenomenon is called hot electron effect [51]. The decoupling can act as a bottleneck for an example in the case of the heater element, because it has a high Joule heating power. In the case of the thermometer, we can assume that electrons are well coupled to phonons, since Joule heating caused by the SINIS bias current is small. In the clean limit $ql << 1$, where$q$ is the phonon wave vector and l the electron mean free path, the electron energy is transferred to phonon energy at a rate

$$P_{\text{e-p}} = \Sigma\Omega(T_{\text{e}}^5 - T_{\text{p}}^5). \tag{71}$$

Here T_{e} and T_{p} are the electronic and phononic temperatures, Ω is the volume of the normal metal and Σ is the electron phonon coupling constant. It is given by [52]

$$\Sigma \approx 0.525\alpha^*\gamma, \tag{72}$$

where γ is the Sommerfeld constant and

$$\alpha^* = \frac{6\zeta(3)k_{\text{B}}^3}{2\pi\mu\hbar^4 v_{\text{s}}^4 v_{\text{F}}} \left(\frac{2E_{\text{F}}}{3}\right)^2, \tag{73}$$

with ζ as the Riemann zeta function, v_{F}, E_{F} are the Fermi velocity and energy, v_{s} is the speed of sound and μ is the mass density. The parameter Σ is usually obtained from experimental data [53].

The phononic heating power must transfer from the normal metal element of the heater to the SiN membrane. Since phonons are the only way to transfer the heat over this interface, the incoming phonon must have a suitable state available on the other side of the interface. So we have the so called acoustic mismatch situation, where lack of available states creates thermal resistance at the interface. This resistance is also known as Kapitza resistance [54, 55] and is defined as

$$R_{\mathrm{K}} = \frac{\Delta T}{P} = \frac{15\hbar^3 \rho_{\mathrm{e}} v_{\mathrm{e}}^3}{2\pi^2 k_{\mathrm{B}}^4 T^3 A \rho_{\mathrm{r}} v_{\mathrm{r}}}, \tag{74}$$

where ΔT is the temperature difference over the interface, P is the thermal power transmitted through the interface, ρ_{e}, ρ_{r} are mass densities of the phonon emitter and receiver, v_{e}, v_{r} are the transverse sound velocities of the phonon emitter and receiver, and A is the contact area. An assumption of small temperature difference ($\Delta T << T$) was made in writing equation (74). Also it only works for 3D objects, theory describing the thin film case is not readily available.

3 Fabrication methods and equipment

In this section all fabrication methods used in this thesis are explained. Special care in explanation is taken with methods that were new to me during this project. All fabrication steps are listed in Table 1. They containt three main steps: SiN membrane, SNS junction and SINIS junction fabrication. The equipment used for the fabrication are shown in Figure 12. All fabrication was performed by the author and the work was carried out in the university of Jyväskylä at the Nanoscience Center (NSC) cleanroom facilities.

Table 1. All fabrication steps in execution order

Fabrication step	Equipment used	Processes
1° SiN membrane	• Spinner • SEM • RIE • Wet etch bench	**1°** Resist spinning **2°** Electron beam exposure **3°** Dry plasma etching of SiN **4°** Wet etching of Si
2° SNS junction	• Spinner • SEM • RIE • UHV evaporator	**1°** Resist spinning **2°** Electron beam exposure **3°** Oxygen plasma cleaning **4°** Metal evaporation
3° SINIS junction	• Spinner • SEM • RIE • UHV evaporator	**1°** Resist spinning **2°** Electron beam exposure **3°** Oxygen plasma cleaning **4°** Metal evaporation

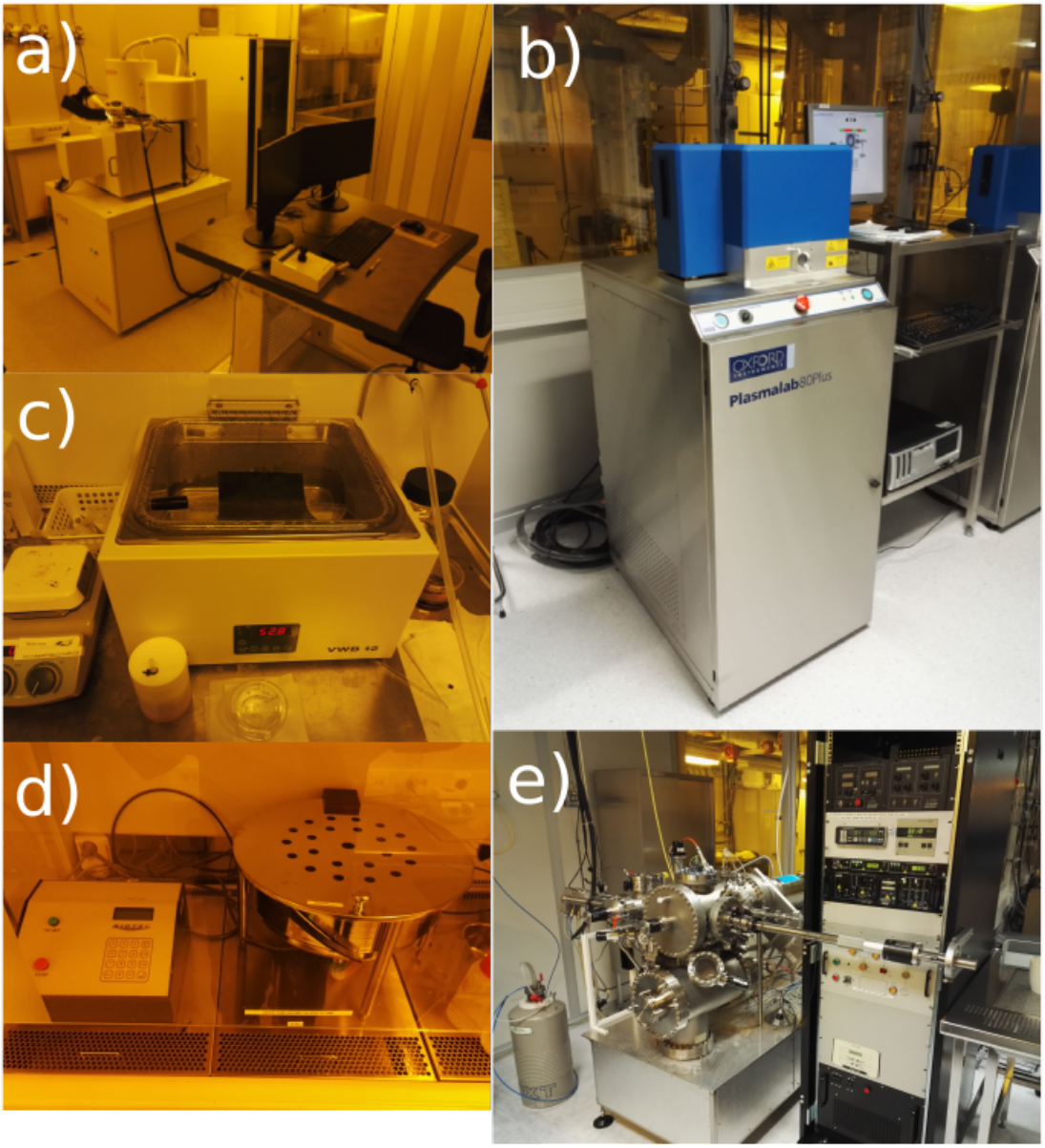

Figure 12. a) Raith eLine SEM used for imaging and EBL, b) Oxford Plasmalab 80 Plus RIE used for SiN etching and oxygen plasma cleaning, c) wet etch bench under a fume hood with VWR VWB 12 hot water bath and KOH solution stored in the white plastic container, d) spinner used for resist application, e) UHV evaporator used for PVD processing.

3.1 Electron beam lithography

Electron beam lithography (EBL) is done using a scanning electron microscope (SEM). NSC has a Raith eLine SEM in the cleanroom facilities. The EBL process utilizes a resist that is exposed with an electron beam. Depending on the properties of the resist, the exposed area either gets removed by a development process while the non-exposed area is conserved, or for a different resist, the exact opposite can be achieved. These resist types are called positive or negative, respectively.

A positive resist is made of long polymer chains that are broken to smaller pieces by the electron beam. Once a short enough chain length is achieved, the resist becomes soluble to a developer, which typically is some sort of an organic solvent. On the other hand, the negative resist is made of shorter polymer chains. These are crosslinked by the secondary electron scattering due to the electron beam. Thus, the exposed area is no longer soluble to the developer solvent [56]. For the samples in this thesis only positive resists were used.

The EBL process has a lot of steps, and each of those has an impact on the quality of the resulting sample. One has to pay attention to the results after each individual step of the EBL process. For example, if there is something wrong with the electron beam and the exposure fails, there is no point of trying to develop the sample. Cleanliness also plays an important role in every step of the EBL process, because for example dust particles are bigger than smallest features exposed in this thesis work.

3.2 Metal evaporation

Metal evaporation in this thesis was carried out by an UHV (Ultra High Vacuum) evaporator, one of the methods to realize physical vapor deposition (PVD). It is based on electron beam heating of the metal to be evaporated. The electron beam is created by thermionic emission of electrons. A tungsten filament is heated up by driving a current through it. Increasing the current through the filament also increases the electron current escaping the filament. Thermionic emission of electrons was first found in 1872 by Frederick Guthrie [57]. Thermionic electron emission was later developed further by biasing the filament voltage negatively to help more electrons escape the filament. This type of electron emitter is called a field enhanced thermionic emission or Schottky emission and is widely used as an electron gun in many applications[58]. Vacuum is needed for the electron transport from the filament to the crucible and to achieve a sizeable metal evaporation rate. The evaporation rate is proportional to the difference of the vapor pressure of the metal and the vacuum vessel pressure. A greater difference gives a better evaporation rate. It is worth noting that typically the mean free path of evaporated atoms is longer than the evaporator dimensions. Thus, metal atoms transport is ballistic and allows angle evaporation techniques to be used, since the atoms follow a line of sight path.

In the UHV evaporator at the NSC the electron beam is guided with magnetic fields into a crucible containing the metal. There is also a sweep control for the electron beam. It allows the operator to adjust the electron beam so that it hits the whole metal piece, making the heating process more consistent and less violent to the metal. There is an adjustment in beam position too, so that the operator can hit the target. The UHV evaporator at the NSC has a revolving holder that typically contains aluminum, gold, titanium, niobium and silver. Only one metal is visible to the electron beam at once. The sample is loaded through a loading chamber so that the actual evaporation chamber is kept at vacuum at all times. The loading is done by actuating a magnetically coupled rod. There is an oxygen line connected to the loading chamber, which allows in-situ oxidation of samples. This is particularly useful for oxidizing aluminum during the SINIS thermometer fabrication. Inside the evaporation chamber there is a liquid nitrogen tank that further improves the vacuum by acting as a cold trap. Typical pressure values during evaporation vary from 10^{-9} mbar to 10^{-7} mbar. The UHV state of the evaporation chamber is maintained by a cryopump, while a turbo pump takes care of the loading chamber side. After the loading chamber is exposed to an atmospheric pressure, it is pre-pumped with a rough pump before turbo pump valve is opened. There is also an Intellemetrics IL150 quartz crystal growth rate monitor attached to the evaporator. It measures the evaporation speed and thickness.

3.3 Suspended SiN membrane fabrication

I already discussed about suspended SiN membrane fabrication quite extensively in my research training report [15]. In short, a 500 μm thick silicon wafer coated with 300 nm silicon nitride (SiN) on both sides was cut to small chips (8 mm$\times$8 mm). Then, electron beam lithography was used to expose about 800 nm thick 950 PMMA A7 resist layer, which was applied on top of the chip by spinning. The exposure pattern contains five square areas (780 μm$\times$780 μm) and the resist was removed from these areas by the development process. Then, the chip was cleaned with oxygen plasma and the exposed SiN was removed by CHF_3+O_2 plasma with a gas flow ratio 10:1, using reactive ion etching (RIE). After RIE, the chip was immersed in 34 % aqueous potassium hydroxide (KOH) solution for wet etching the silicon. The KOH solution container was placed in 98°C water bath. The wet etching process took about 5–6 hours, after which the suspended SiN membranes were ready. Typical membrane size with these parameters was 60–80 μm$\times$ 60–80 μm.

Once the suspended SiN membranes were ready, their locations on the chip needed to be determined. A SEM was used to find the coordinates. First, a corner of the chip was located and marked as origin. Then, the center membrane was found and coordinates with respect to the chip corner were written down. The center of the center membrane was marked as a new origin. Each of the remaining four membranes were located, and their coordinates with respect to the center membrane

were written down.

3.4 SNS design and fabrication

A 2D model of the SNS heater was drawn using Raith ELPHY Multibeam software, with the design shown in Figure 13. Simple 2D models (rectangles) were joined together in order to create the desired design. The design contains multiple layers to allow separate exposure for different parts of the heater structure. The idea behind the new heater geometry is that approximately all phonon power is emitted outwards when the thermometer is in dynamic equilibrium. As the thermometer reaches dynamic equilibrium, it must emit as much phonon power as it absorbs, so the net power flow into the thermometer is zero. The heater, on the other hand, is not in thermal equilibrium with the SiN membrane. The power flow that the heater emits can go inwards (toward the heater) or outwards (toward the membrane edge). One might think that the inward power flow is a problem, but since net absorbance of the thermometer is zero in dynamic equilibrium all inward power ends up back at the heater. Thus the net power flow going inwards is zero.

When the design was ready, it was made sure that there would not be any overlaps in the design which would lead to double exposure of some parts. Luckily, there was an operation called ''overlaps out'' in the software that removed all possible overlaps.

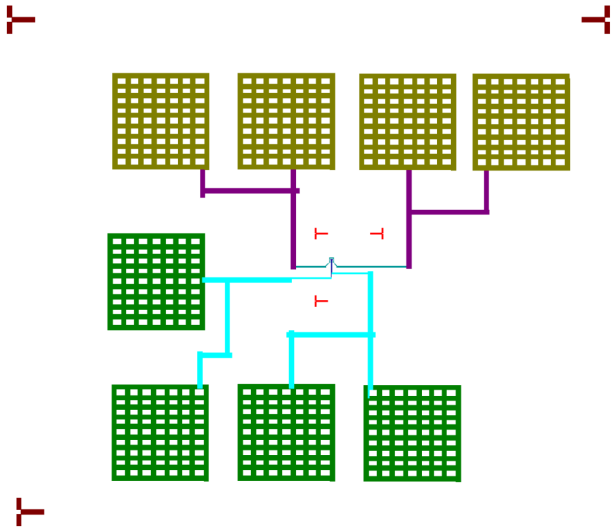

(a) Full design of the sample, bonding pads are 200 μm in size.

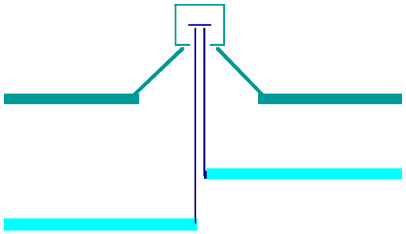

(b) Fine structure of the sample. Thinnest wires are 300 nm wide. The heater is the square shaped wire, and the wire inside it is the thermometer.

Figure 13. Different design layers are presented in different colors.

A standard EBL process was used for the SNS fabrication. A multilayer resist was first applied on top of the chip. A datasheet provided by Microchem was used to determine the spinning speeds needed for wanted resist thicknesses [59]. The first (bottom) layer was 9% poly(methyl methacrylate-methacrylic acid) in ethyl lactate or P(MMA-MAA) EL9 in short. This layer was spun at 2500 rpm speed and baked for 1 min at 160°C to form a 400 nm thick layer. The second layer is 950 000 molecular weight 4% polymethyl methacrylate in anisole or 950 PMMA A4 in short. This time the spinning speed was 2000 rpm and the chip was baked again for 1 min at 160°C resulting in a 350 nm layer. The chip was then put in a vacuum chamber for at lest an hour to evacuate any trapped air and solvent. A thin layer (5 nm) of aluminum was evaporated with the UHV evaporator to reduce the effects of resist charging during the electron beam exposure. The final layer of resist is identical to previous 950 PMMA A 4 layer, but now the chip was baked for 3 min at 160°C. So the total resist layer was 400 nm + 5 nm + 2×350 nm $\approx$ 1.1μm thick.

The sample was then loaded into the SEM to begin the patterning process. A corner of the chip was located, and previously measured coordinates were used to jump to the center membrane used as global origin. The other four membranes were found with the help of the coordinates found earlier during the membrane fabrication. A single image scan was performed at each membrane position to confirm the correct position. The suspended membrane area shows up as a black square in the otherwise gray SEM image. If there was an error in the positioning, a correction was made by measuring and compensating the error. This procedure made sure that the exposure of the SNS design would hit to the center of the membrane with excess exposure from imaging avoided.

The electron beam exposure was carried out in two steps. The general electron microscope settings for the EBL process in this thesis were 20 kV acceleration voltage, 300 μC/cm^2 area dose, target beam speed 7 mm/s. First, the narrower wires in the SNS junction area were exposed with a 50 μm write field, or 2000× magnification, using a 30 μm aperture. This configuration typically yields about 0.3 nA current. Then, the wider wires connecting to thinner ones, bigger markers and the bonding pads were exposed with a 120 μm aperture and 1000 μm write field, or 100× magnification. With the bigger aperture, the current was about 5 nA. In both exposures the exposed areas could not fit in a single write field, so write field stitching was used. This is possible since our microscope has a laser interferometer stage which allows very precise movements. Stitching means just that the area to be exposed is divided into multiple write field sized areas. Then the stage moves from one area to another one.

The sample was then taken to a laminar flow hood and the first layer of PMMA was developed by submerging it to 2:1 ratio of isopropyl alcohol (IPA) and methyl isobutyl ketone (MIBK) for 20 s. The sample was then quickly transferred to a dish filled with IPA for one minute and then dried with a nitrogen gun. Then the aluminum layer was removed by immersing the sample in a room temperature 34 % aqueous KOH solution for about 10 s. The sample was neutralized by submerging it

into a dish filled with deionized water for one minute, and the sample was rinsed with IPA and dried with the nitrogen gun. The unveiled second PMMA layer was then developed by the same manner as the previous one. The co-polymer layer was then developed by immersing the sample in 2:1 ratio of methanol and methoxyethanol for 7 s. The sample was again quickly transferred to the IPA dish for one minute and dried with the nitrogen gun. At this point, there was a SiN membrane visible from the exposed areas, but it was made sure that there would not be any remains of the resist by performing an oxygen plasma cleaning with RIE. The cleaning process lasted for 30 s and used microwave power of 60 W and oxygen gas flow of 50 sccm.

After the plasma cleaning the sample was ready for metal evaporation. The schematic for all the evaporation is shown in Figure 14. The evaporation process started with 5 nm of Ti with evaporation speed of 0.1 nm/s from a 60° angle to create an interface-barrier layer between SiN and Nb. During previous work done in our group it was noted that the superconducting Nb on top of SiN was higher quality if a thin layer of Ti was placed in between the Nb and the SiN. It is known that Nb oxidizes, and the final form of this process is Nb_2O_5, which is an electric insulator. However, this oxide layer is only a few nanometers thick from the surface, if the Nb was exposed to oxygen in atmosphere [60]. Literature shows that NbN is more easily oxidized, and thus the Nb lattice gets degraded deeper than in pure Nb [61]. High concentrations of oxygen was observed even at 50 nm depth of NbN film. This rises a suspicion that SiN and Nb could form NbN and leave some pathway for oxygen to penetrate deeper. It is also noticed in previous work done in our group that superconductivity of Nb appears at higher temperatures (closer to bulk values) when evaporation is done at higher rate [62]. This causes the Nb grains to be smaller in size, which leads to more grain boundaries. These boundaries can act as pathways for oxygen to diffuse even deeper resulting in thicker oxide layer. Interestingly the stress of the Nb film has an impact to the amount of oxygen penetrating into Nb through the grain boundaries. It was shown [61, 63], that higher tensile stress can protect Nb from oxidizing. Measurements revealed also that T_c is higher when the tensile stress gets higher.

20 nm of Nb was evaporated on top of the Ti layer with evaporation speed of 0.2 nm/s, also evaporated from 60° angle from the sample surface normal. This process was repeated after rotating the sample stage 90 degrees to form the second superconducting wire. Next the normal metal part was fabricated. Now 5 nm of Ti was used as a ''glue'' for 20 nm of Au which was evaporated at 0.1 nm/s speed. The normal metal part was evaporated from the sample surface normal. These steps are shown in Figure 14.

The sample was then taken out of the UHV evaporator and transferred to an acetone filled glass dish, which was heated to the boiling point of acetone on a heat plate. Once the acetone was forming bubbles, a syringe with a needle was filled with hot acetone and placed just above the sample. Acetone flow from the syringe was increased until the resist seemed to lift off. The sample was dipped in IPA and dried with a nitrogen gun. The results were then inspected with an optical microscope

and additional acetone washing was performed if some resist remains were visible.

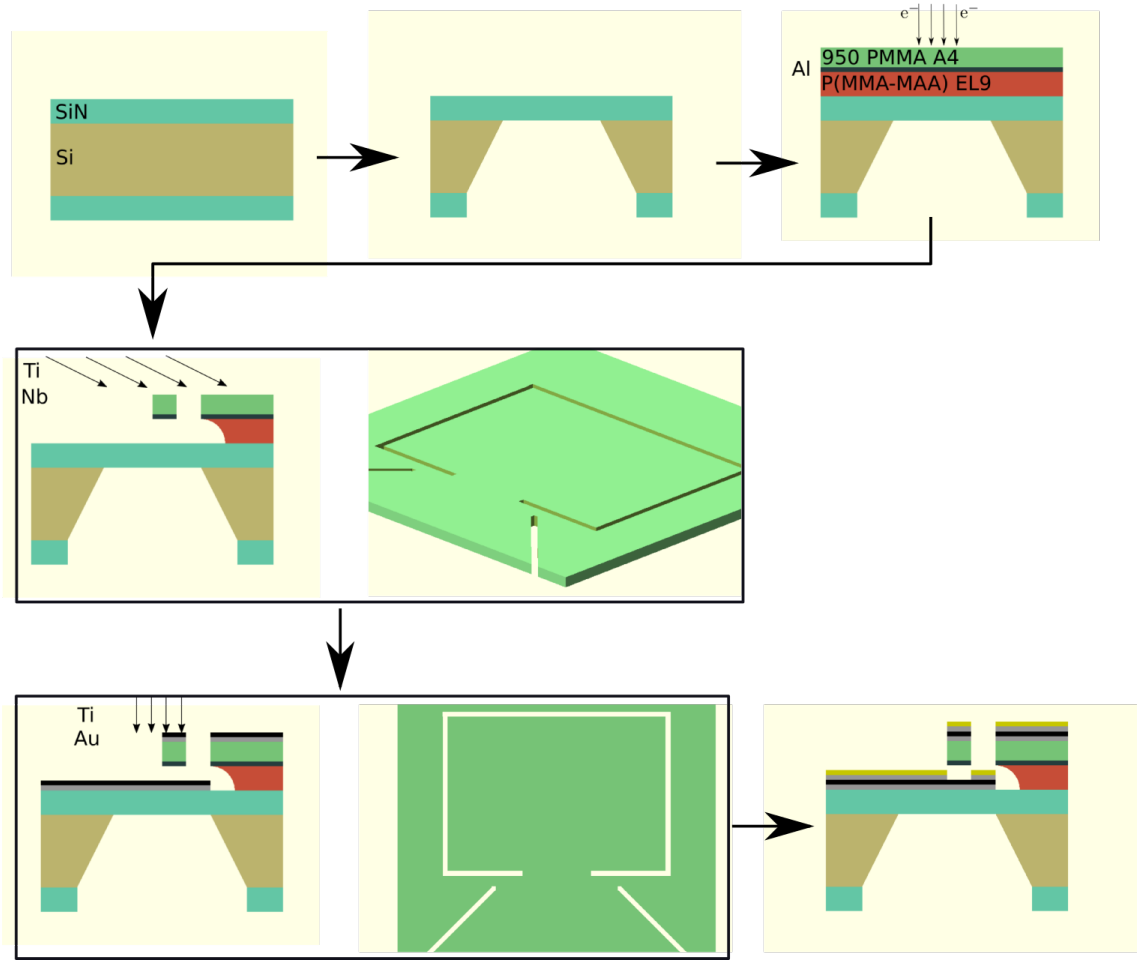

Figure 14. SNS fabrication process. The green 3D schematics show realistically the effect of the angle evaporation technique. Using a thick enough resist or steep enough evaporation angle, the evaporation source can't see some parts of the substrate surface. Thus, angles can be used choose which parts of the design gets deposited with metal.

3.5 Theory of heater thermometer geometries in ballistic regime

Here I will present some estimates of the view factors with the help of equations presented in section 2.6.6 to justify the new heater geometry. Since we consider the 2D case, we have to change all surface areas A to lengths L, as already was discussed in section 2.6.6.

For two wires (heater h and thermometer t) of same length L and separated by a

distance d and are parallel in orientation, we have a view factor [64]

$$F_{\text{parallel}} = \sqrt{1 + \frac{d^2}{L^2}} - \frac{d}{L}. \tag{75}$$

Equation (75) assumes that there is no radiation to the back side of the heater wire, ie. the view factor in one half space is only considered. To extend this equation to full 2D space we have to divide F_{parallel} by two.

Let's imagine a simplified model of the new heater-thermometer geometry (see Figure 15). In the simplified model the heater is $L_{\text{h}} = 32\,\mu$m long and the thermometer is $L_{\text{t}} = 5\,\mu$m long. In this model the opening in the heater has the same length as the thermometer and distance between the opening and the thermometer is $d = 5\,\mu$m. We'll start by enclosing the heater fully, so that the total view factor from the thermometer to the enclosed heater F_{tot} sums up to one, as dictated by Equation (70). Now we can use the summation rule of view factors and Equation (75) for the full 2D space view factor from the thermometer to the opening F_{to} to calculate the real view factor from the thermometer to the heater F_{th}.

$$F_{\text{th}} = F_{\text{tot}} - F_{\text{to}} = 1 - \frac{1}{2}\sqrt{1 + \frac{d^2}{L_{\text{t}}^2}} + \frac{d}{2L_{\text{t}}}. \tag{76}$$

Since $d/F_{\text{t}} = 1$, we get $F_{\text{th}} \approx 0.8$. This means that 80% of the power emitted from the thermometer is intercepted by the heater, assuming emissivity of one. To get the view factor from the heater to the thermometer F_{ht}, we can use the reciprocity law, Equation (69)

$$F_{\text{ht}} = \frac{L_{\text{t}}}{L_{\text{h}}} F_{\text{th}} \approx 0.13. \tag{77}$$

So 13% of the power emitted by the heater is intercepted by the thermometer, again assuming the emissivity of one. Of course, there are other effects too that contribute to the real, physical absorption, but let's leave those out of this analysis.

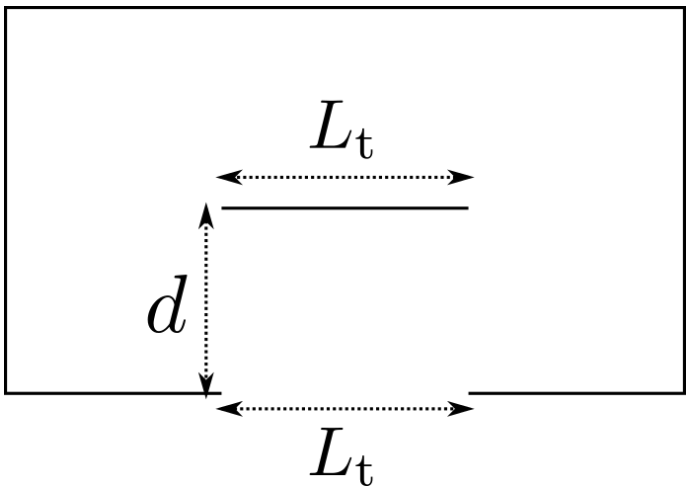

Figure 15. A simplified model of the heater-thermometer geometry with the dimensions used in the view factor calculation.

3.6 SINIS design and fabrication

The SINIS design follows a typical structure as seen in many previous studies. Since the old design works well there was no need to change it. The SINIS fabrication started with the resist application in the exact same manner as in the SNS case, so I don't repeat the process here. Instead, I'll go through how the lithography was targeted in the right spot. As seen from Figure 13 illustrating the design, there is not much margin for error in the SINIS lithography. The wires of SNS and SINIS junctions can't touch, so great care needs to be taken to make sure this does not happen.

Once focus and stigmation settings were roughly set, the center membrane on the chip was searched and marked as a global origin. A spot was exposed at 200000× magnification for 45 s near the center membrane, but not on the suspended part. More precise focus and stigmation adjustments were made using the spot as a target feature. The spot exposure and the focus and stigmation adjustments were repeated until the spot was clearly visible and less than 20 nm in size and round in shape. From there, a jump was made to one of the sample membranes and a rough local origin was set. A bigger marker (see Figure 13) was located, angle and origin corrections were performed using these bigger markers. Then, the smaller markers (see Figure 13) were located and the final, more precise angle and origin corrections were performed. At this point, the local origin and the angle should match with the SNS structure. A three-point adjustment was done by locating all three smaller markers and giving their supposed coordinates to the software to make sure that the SNS and the SINIS structures would match perfectly. A Final check of the focus and stigmation was performed by exposing a spot near the membrane area to be exposed. Then the write field alignment was performed using the exposed spot as a target feature. The first exposed item was the SINIS junction area, containing thinner wires using a 50 μm write field and a 30 μm aperture. Then, wider wires and bonding pads were exposed using a 1000 μm write field and a 120 μm aperture.

The development process was again conducted the same way as in the SNS case. The evaporation of the SINIS junction begun with 20 nm of aluminum at 60° angle from the sample surface normal. The sample was then transferred back to the loading chamber, and oxygen was released in so that the pressure was around 200 mbar. The sample was kept in the oxygen environment for 5 minutes, after which the loading chamber was pumped to a vacuum. The sample was then rotated 90 degrees and transferred back to the evaporation chamber for the normal metal evaporation. The normal metal in this case is again a Ti Au bi-layer where Ti was evaporated first and Au after that. The normal metal evaporation was performed from 55, 50 and 45 degree angles. Now the angles were used from both sides, so if the sample surface normal is 0°, then evaporation was made form ± 55° ± 55° and ± 55° in turns. About 1 nm of Ti and 4.5 nm of Au was evaporated in one turn to reach total thicknesses of 6 nm Ti and 42 nm Au. These angles combined with the rotation made earlier made sure that the Al wires near the junction area would not be covered

with normal metal, and multiple angles ensured minimal shadowing effect. Thus, the superconductivity of the wires near the normal metal island should not be affected by the vertical proximity effect, or phonons should not strongly scatter from the Al leads. The final product can be seen in Figure 16.

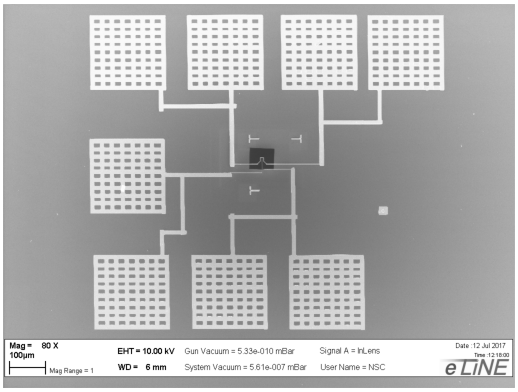

(a) SEM micrograph of the whole sample stucture.

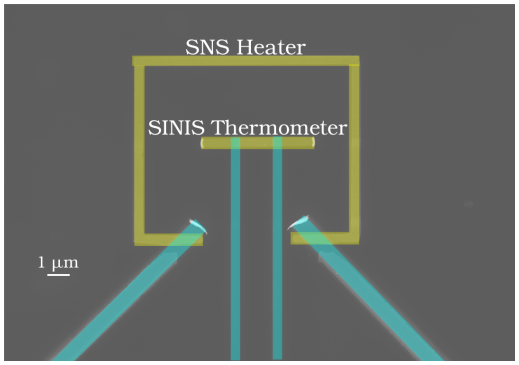

(b) Zoom-in of the SNS heater and SINIS thermometer.

Figure 16

3.7 Challenges

First issues were caused by bad design choices, but they were easily fixed by iterating the design and fabrication steps. Typically, these problems came visible after the metal evaporation and one solution was to fine tune the evaporation angles. One design issue for example was with the SINIS junction superconducting wires that are very close together. When a 60 degree evaporation angle was first used for the normal metal evaporation, the superconducting wires got connected with normal metal from a wrong place, see Figure 17. The contact was avoided by changing the maximum evaporation angle to 55 degrees.

At one point all chips came out very dirty from the KOH etching of the membranes. The chip surface looked like there was pieces of resist, however, hot acetone bath or O_2 plasma cleaning were not able to get rid of the dirt. Hot acetone bath with acetone flow from a syringe cleaned the surface a bit, but not completely. Ultrasonic cleaning was out of the question, because it is known to break suspended membranes. The key for this was to dispose the old KOH solution and make new. Also, the chip was cleaned in hot acetone in an ultrasonic cleaner and polished with a cotton swab before KOH etching to keep the KOH solution clean.

Early on the resist was cracking from the sharp edges of the structure, causing electric contacts that were undesirable, see Figure 18. The cracks were caused by charging of the resist layer. The problem was fixed by evaporating a thin layer of aluminum between the two PMMA layers, as discussed above. Another issue seen in

Figure 18 is the resist bridge collapsing above SINIS junctions. It can be caused by a combination of charging and a too thick co-polymer layer. The aluminum layer and a thinner co-polymer layer were solutions to this issue.

The last problem with the fabrication process was particularly annoying. Small normal metal pieces from the SNS junction broke away during lift-off. This problem lasted for about a month and several fixes were tried. Different plasma cleaning processes together with adjustments to the development process were tried, but they did not resolve the issue. Finally, once the co-polymer bottle was nearly finished, a new co-polymer solution was made, and it fixed the issues. So the co-polymer had gone bad or the composition of the old resist was not what was originally intended.

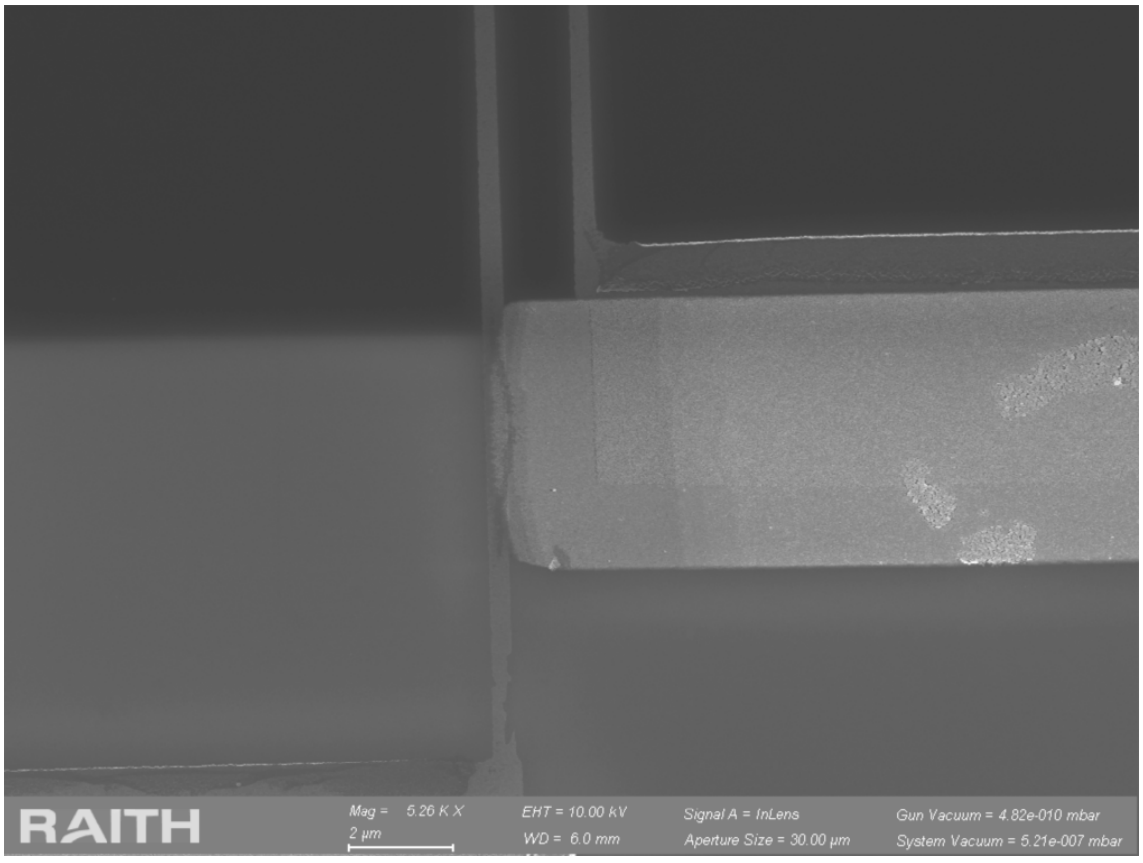

Figure 17. SINIS junction appeared in wrong place with a too large evaporation angle. The membrane edge is seen at the background color change position. The narrow wires going upwards are supposed to form the SINIS junction with the normal metal island higher up in the middle of the membrane.

Figure 18. Resist cracking caused unwanted electric contacts. Cracking and resist bridge collapsing were fixed by applying thin aluminum layer between the two PMMA layers and using thinner co-polymer layer. The cloudy background is probably some impurities on the backside of the SiN membrane.

4 Measurements and results

This section describes the measurement setups and presents the data analysis along with results.

4.1 Experimental methods and equipment

The main tools for carrying out the experiments are shown in Figure 19. After the sample fabrication was done, the sample was tested for its room temperature resistance. The chip was fixed to a steel plate under a microscope. Thin probe spikes were attached to microactuators with a magnetic base that allow precise movement of the probes. The probes were connected to a Fluke 75 III multimeter, and the microactuators were used to connect the probes to bonding pads on the chip. The measurement was done by choosing a manual range and starting with the highest one. If the result showed an overload, there was no electrical contact between the pads. If the multimeter showed some other value than overload, the range was reduced until a reasonable value was shown in the multimeter screen. Typically the SNS heater and the SINIS thermometer showed resistance values of ~1 kΩ and ~4–8 kΩ, respectively.

A sample stage of a ^{3}He-^{4}He refrigerator, later known just as a cryostat, was connected to a brass stand and grounded through all bonding pads. The sample stage bonding pads were polished with a piece of 1000 grit sanding paper to remove any oxidized copper that could affect the bonding process. The chip was glued to the sample stage using ethanol thinned varnish and tobacco paper. The tobacco paper was used to leave some porosity between the stage and the sample so that any air that was trapped to a cavity under the SiN membrane could escape when the cryostat would be pumped to a vacuum. Thinned varnish was chosen to stop it from contacting the membrane, and thus creating a direct thermal link between the membrane and the sample stage. The varnish was left to dry for a couple of hours before using an ultrasonic bonder (Kulicke&Soffa 4523A Digital) to connect the sample bonding pads to the sample stage pads with aluminum bonding wire. The sample stage was then removed from the stand and connected back to the cryostat. A contact check was made with a Fluke 77 multimeter to make sure there was enough working electrical connections to proceed with the experiment.

The cryostat was then transferred to an electromagnetic interference (EMI) shielded room and its vacuum jacket was pumped over a weekend with a diffusion pump backed by a dual stage rotary vane pump. The room provides attenuation of

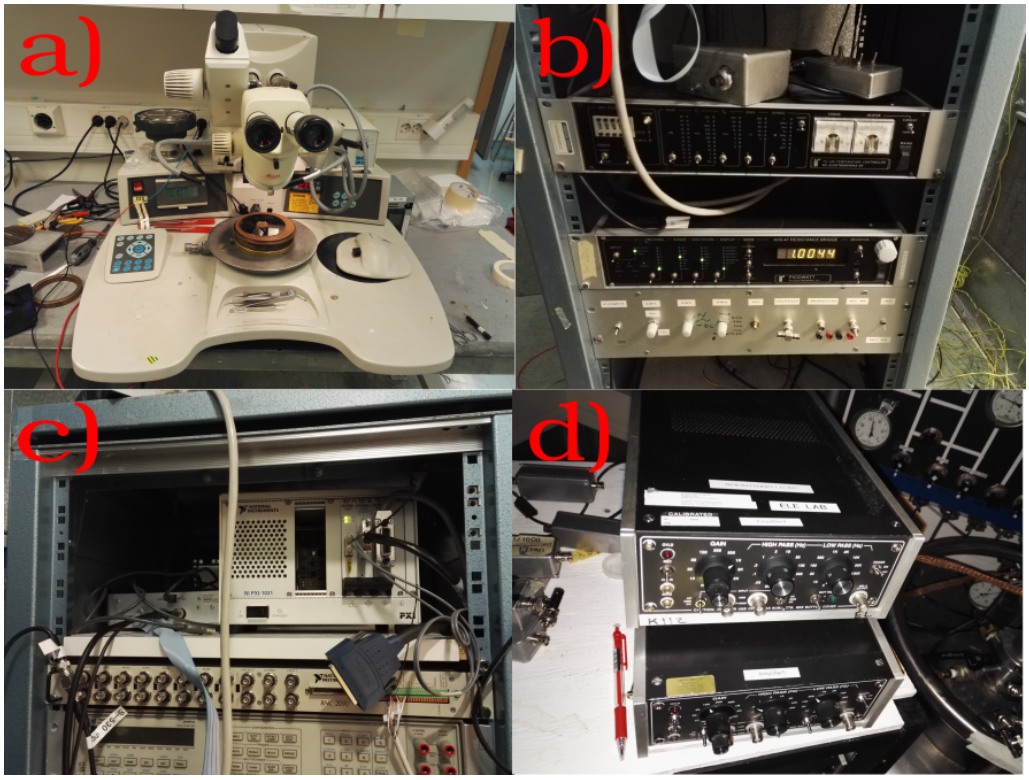

Figure 19. a) Ultrasonic bonder for bonding the sample on a cryostat sample stage. b) Devices from the top: PID controller for controlling the stage temperature, resistance bridge for measuring stage thermometer resistance, car battery powered voltage sweep box. c) Data acquisition system. d) Two voltage amplifiers.

electromagnetic radiation interference in the normal environment. The cryostat was precooled in a liquid nitrogen dewar to 77 K for about an hour before transferring it to a liquid helium dewar. For the liquid nitrogen precooling, a small amount of air was let into the vacuum jacket to act as heat exchange gas. For cooling to 4 K, <1 mbar of ^{3}He/^{4}He mixture was let in the vacuum jacket for heat exchanging, and as the 4 K limit was reached the mixture was pumped away. Then internal vacuum lines of the cryostat were pumped dry by circulating a small amount of ^{3}He/^{4}He mixture through a cold trap that was cooled with liquid nitrogen. All vacuum lines were pumped and ^{3}He/^{4}He mixture was let into isolated still line and condensed with a pot cooler that operates at about 1.3 K. When circulation of the mixture is on, ^{3}He and ^{4}He phase separation at the mixing chamber provides the cooling power for the sample stage via a thermal link.

Voltage was measured with a DL Instruments model 1201 voltage amplifier whose output was set to -10–10 V range. Since the probing signal was nearly DC, low and high pass filter cut-off frequencies of the voltage amplifier were set to 3 Hz and DC, respectively. The amplified voltage signal was fed to a National instruments BNC-2090 data acquisition system (DAQ). The analog signal was converted to a

Figure 20. Measuring room in use.

digital form by a National Instruments PXI-6251 analog to digital converter (ADC) card attached to a National Instruments PXI-1031 chassis. The digital signal was sent to a computer through optical fiber by a National Instruments PXI-8335 PCI-PCI bridge, PCI stands for Peripheral Component Interconnect, and it is a bus for connecting hardware to a computer. In the system used here, one PCI card connected to the National instruments PXI-1031 chassis sends data to another one located inside the datalogging computer. Digital data was logged to a text file by National Instruments Labview software. The current was measured with a DL Instruments model 1211 current amplifier that outputs a voltage signal proportional to input current. The same DAQ and ADC systems were used for the current measurement. The temperature measurement at the sample stage was performed with a Lake Shore Cryotronics Inc. germanium resistor (model GR-200A-30-0.05). The resistance of the resistor was measured with a RV-Elektroniikka Picowatt AV47 resistance bridge, using a scale range of 0.2–2. The resistance bridge utilizes different scale factors from 1 to 10^6 so the full range of the bridge is 0.2 Ω –2 MΩ.

As the cryostat reached the lowest temperature, current-voltage curves (IV curves) of the SINIS junction were measured at different temperatures, starting with the

lowest one. Temperature was regulated by a PID (proportional-integral-derivative) controller (RV-Elektroniikka TS-530), which controlled power input to a stage heater. A voltage sweep box was used to control voltage over the SINIS junction. The sweeping speed was set to the lowest value, and triangle wave was selected as the signal wave form. The sweep box was powered from two car batteries connected in series, with a maximum voltage range from -12 V–12 V. A SINIS junction could break at these voltages, so a voltage divider was used to reduce the voltage swing. Typical dividers used were 1/5000, 1/2500 and 1/1000. The IV curves were used to characterize and to determine a good bias current for the thermometer usage. See Figure 21 for electrical circuit schematics for the measurement.

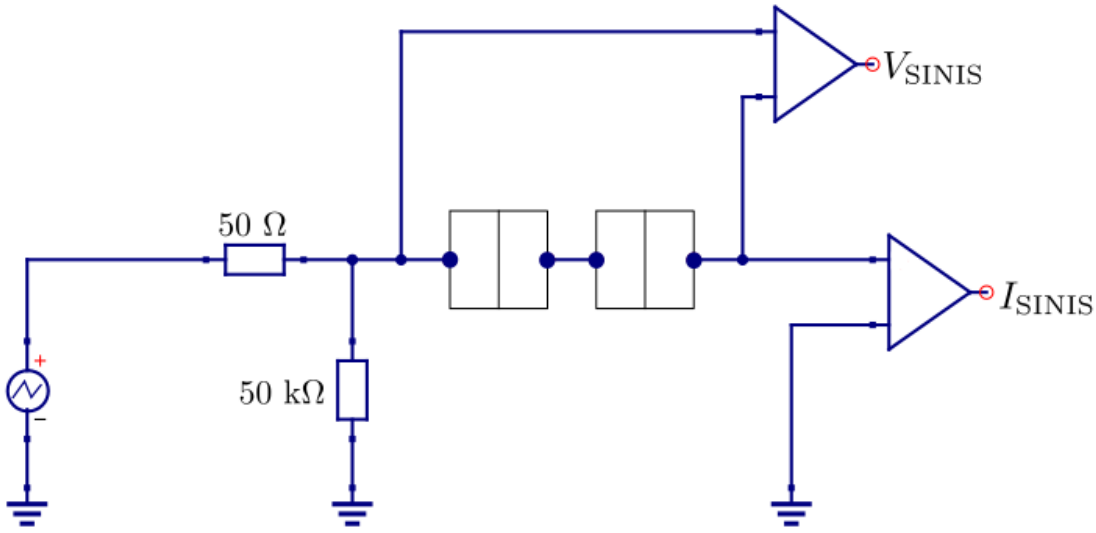

Figure 21. SINIS IV characterization setup. In this example, a voltage divider is made of 50 kΩ and 10 Ω resistors. The divider is used to determine voltage range of the measurement. One NIS junction is represented by the slit square symbol.

After the IV curves were analyzed, a suitable bias current was determined and a floating, battery powered constant current source was utilized to push the current through the junction. The voltage over the junction and the stage temperature were measured in the same manner as before. The cryostat stage was heated close to the aluminum critical temperature, and was then left cooling back down,while measuring previously mentioned physical quantities. This is for calibrating the SINIS thermometer, as by using the collected data it is possible to convert the voltage over the junction to temperature. The SINIS thermometer was calibrated for two different bias currents.

A heating experiment was conducted by using the voltage sweep box as a power source for the SNS heater, see Figure 22 for electrical circuit schematics. The voltage and the current over the SNS heater were measured along with the SINIS thermometer voltage. A voltage divider was used to control the maximum input power to the SNS

heater. The cryostat stage temperature was kept constant during the measurement by a PID controlled stage heater. It would have been beneficial to have another SINIS thermometer on the chip to get better readings for the bath temperature. With the used configuration it has to be assumed that the chip temperature follows the stage temperature. The experiment was repeated for three different power swings and with two different SINIS bias currents.

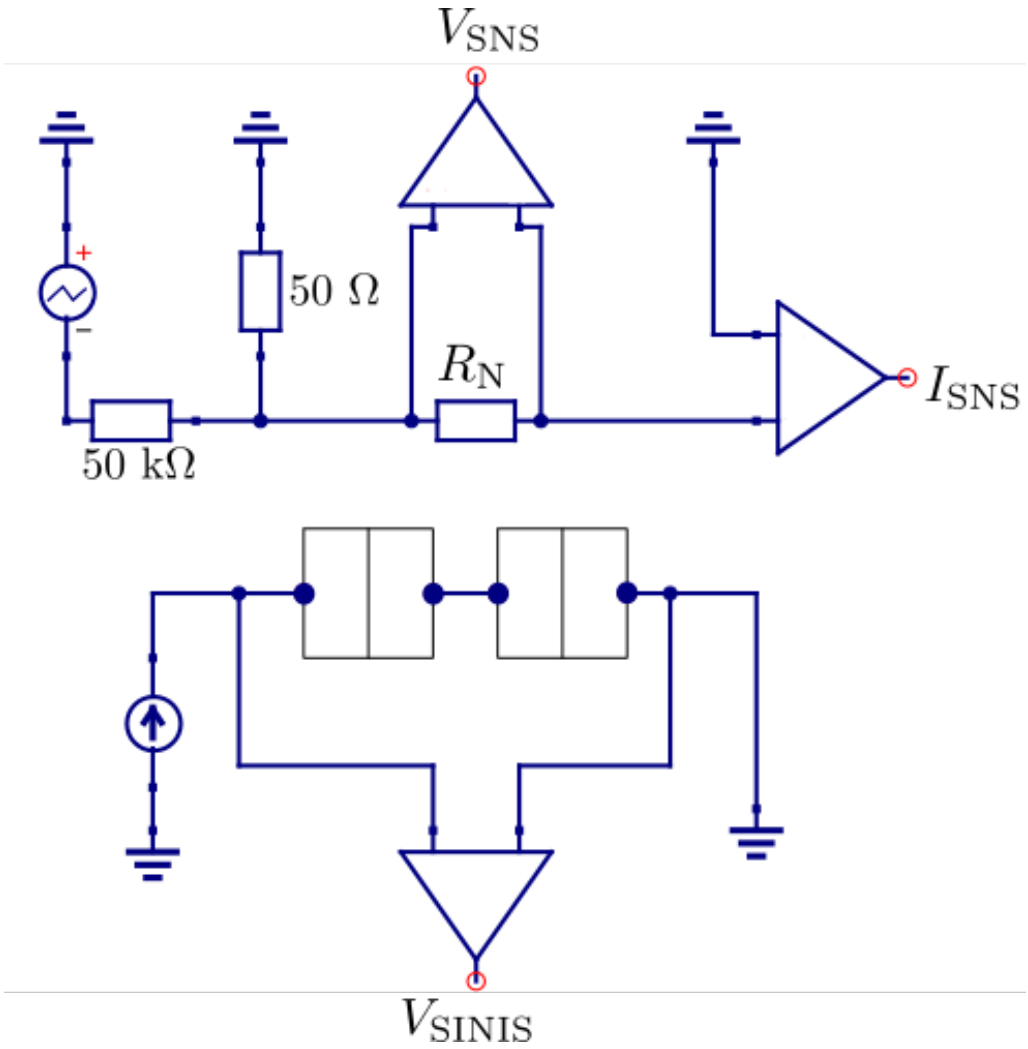

Figure 22. Heating experiment electrical schematics. R_N represents the normal metal of the SNS heater. A voltage divider is now used with the heater to restrict the voltage range.

The last experiment was the critical temperature measurement of aluminum. This time, probing of the SINIS junction was made by a lock-in amplifier (Stanford Research Systems SR830 DSP). A random probing frequency was picked between 14 and 15 Hz. At this range $1/f$ noise is not significant and the 50 Hz noise peak is still far away. Another lock-in amplifier (Stanford Research Systems SR810 DSP) was set to measure the current through the SINIS junction. The current signal was measured

with the same probing frequency as the voltage signal. The phase difference between the voltage and the current was monitored during the experiment to make sure it was close to zero. The experiment was performed during heating of the cryostat. The stage heating power was increased until a drop in the current was observed. The temperature range around the critical point was swept a couple of times in order to record more data. The superconducting phase transition of aluminum wires was clearly observed multiple times during heating and cooling.

4.2 Data analysis and results of the first measurement run

All figures shown in this section were plotted with Gnuplot (version 5.2 patchlevel 0) using cairolatex terminal. Compilation of the final graphs was performed with pdflatex compiler found from TeX Live distribution 2013/Debian. Power vs temperature fits were done with Gnuplot fitting option that utilizes a non-linear Marquardt-Levenberg least squares algorithm. Python interpreter 3.6.1 included in Anaconda 4.4.0 distribution was used to interpret the data analysis codes. All libraries used in the codes can be found in the same Anaconda distribution.

4.2.1 Proximity effect on Nb wire coated with Ti Au bilayer

Before fabricating the SNS junctions, a preliminary study of the T_c suppression of the Nb superconductor when it's coated with normal metal was made. Motivation for this came from the fabrication method, where the normal metal coating can't be avoided. Sample cooling was performed with a dipstick type of a cryostat, see Figure 23. The lowest temperature possible is thus the helium boiling point at 4.2 K.

Figure 23. a) Dipstick sample stage before the sample was bonded. b) Dipstick in action.

Two resistance bridges (RV-Elektroniikka Picowatt AVS47) were used to measure the Nb wire resistance and the stage thermometer resistance. The temperature of the sample stage was controlled by changing the dipping depth. As seen in Figure 24 the critical temperature was higher than the helium boiling point in all cases. There were two Nb wires and two TiAu coated Nb wires. The critical temperature of the normal metal coated Nb wire shows only about one Kelvin drop at most, so proximity effect doesn't cause problems to the behaviour of the SNS heater, since the actual measurements were performed at a much lower temperature than the lowest proximized T_c~5 K. The step-like features in Figure 24 are caused by different critical temperatures, as the critical temperature is dependent on the wire width. There are four clear transitions in the figure and four different line widths in the sample, so everything adds up.

Let's try to explain the observed change of T_c by using Equations (17–19). The thicknesses of the metal layers were approximately 20 nm for Nb and Au. At this point we leave the Ti layers underneath Nb and Au out of the consideration, because it would add too much complexity. However, it would be interesting to see at some point how the equations would look like if they were derived for four metal layers.

We now start the estimation by using the free electron model presented in equation (22) to calculate the densities of states for both metals. From [39] we find values for the Fermi energies

$$E_{\mathrm{F,Nb}} = 5.32\,\mathrm{eV}$$
$$E_{\mathrm{F,Au}} = 5.53\,\mathrm{eV}.$$

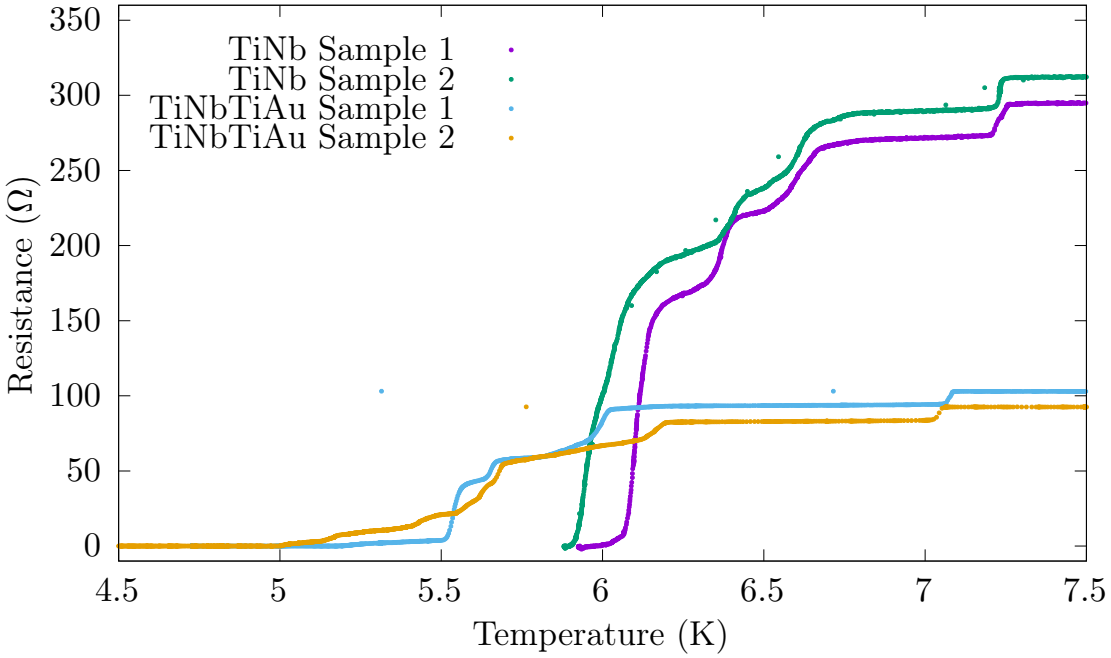

Figure 24. Here the proximity effect on the critical temperature of Nb is clearly seen. In the worst case T_c gets suppressed down to around 5 K for the TiAu coated Nb. Samples 1 and 2 are located on the same chip. Different materials are on separate chips.

Then by using equation (22) we get

$$n_{\mathrm{s}}(E_{\mathrm{F,Nb}}) = 6.12\,\mathrm{cm}^{-3}\mathrm{eV}^{-1}$$
$$n_{\mathrm{n}}(E_{\mathrm{F,Au}}) = 6.24\,\mathrm{cm}^{-3}\mathrm{eV}^{-1}.$$

The Fermi wavelength we can calculate from

$$\lambda_{\mathrm{F}} = \frac{2\pi}{k_{\mathrm{F}}}, \tag{78}$$

and a value for gold $k_{\mathrm{F}} = 1.21$ Å^{-1} is found from [39] too. Now we can calculate d_0 and α from equations (18) and (19)

$$\frac{1}{d_0} = 134000\,\mathrm{cm}^{-1}$$
$$\alpha = 1.0195.$$

Finally we get for the proximized critical temperature from equation (17)

$$T_{\mathrm{c}} \approx 5.5\,\mathrm{K}$$

if $T_{\mathrm{c0}} = 6$ K and $t = 0.13$, we have a good fit for the experiment as can be seen from Figure 24. The transmission coefficient t describes essentially the cleanliness of

the superconductor normal metal interface, ideal interface representing a value of 1. Thus the interface is not fully ideal. However, we have to also remember that there is some effect from the thin Ti layers under the Nb and between Nb and Au that weren't considered in the calculation of the proximized critical temperature.

4.2.2 SINIS IV curves

The recorded current and voltage data of the SINIS junction were opened in Microcal Origin 2015 software (version 92E). Voltage values in the datafile were divided by the amplification factor to get a real physical value. For the current data, a multiplication was used, since the current amplifier had units of attenuation. As the data was converted into actual physical values, an offset of voltage and current needed to be taken into account. At first, a differential conductance ($\mathrm{d}I/\mathrm{d}V$) was calculated and plotted against the voltage. Voltage was shifted so that the conductance peaks were symmetric around the zero voltage point. Then an IV curve was plotted and the current data was shifted so that at zero voltage current is also zero. Then, an IV curve with a logarithmic current scale was plotted, including data from all measurements with different temperatures. Two bias currents were chosen to get good sensitivity for low and high temperatures.

The analyzed data from the first measurement run is shown in Figures 25, 26, 27, 28 and 29, with Figures 25–27 showing IV curves and 28–29 differential conductance vs voltage obtained by numerical differentiations from the I-V data. The difference of the measured data and ideal BCS theory is clear, especially in differential conductance plots 28–29. The subgap conductance seems to have two different slopes (Figure 29), on the positive and negative voltage sides and peak positions are shifted at some temperatures. Also, there seems to be double peaks at some temperatures and especially noisy data peak at 100 mK temperature. Another anomaly is seen in Figure 28, where the differential conductance does not saturate to $1/R_T$ quickly, but shows a drop between 2 and 3 mV. The same behaviour was later duplicated by a colleague (Emmi Kirjanen) and it was discovered that the EMS room grounding was connected to the noisy building grounding. From the building ground, the noise was picked up via the current amplifier that connects the sample to the ground. Later we found that a fix for the issue is to use an isolation transformer between the wall outlet and the current amplifier. However, even with the non-idealities, Figure 27 clearly demonstrates the possibility for thermometry above 100 mK.

A simple BCS fit was performed for all measured temperatures from the IV data using equations 23 and 24. They are shown in Figure 30. The BCS theory didn't give very good fits for any of the temperatures, the closest fits being at 100 mK and 700 mK. The worst fit is at 200 mK and that can be explained by SINIS self cooling effect. Other fitting issues may be explained by the grounding issue during the experiment, which led to non-ideal IV and differential conductance curves. The simple BCS fit parameters are the Dynes' parameter Γ and the superconducting gap Δ.

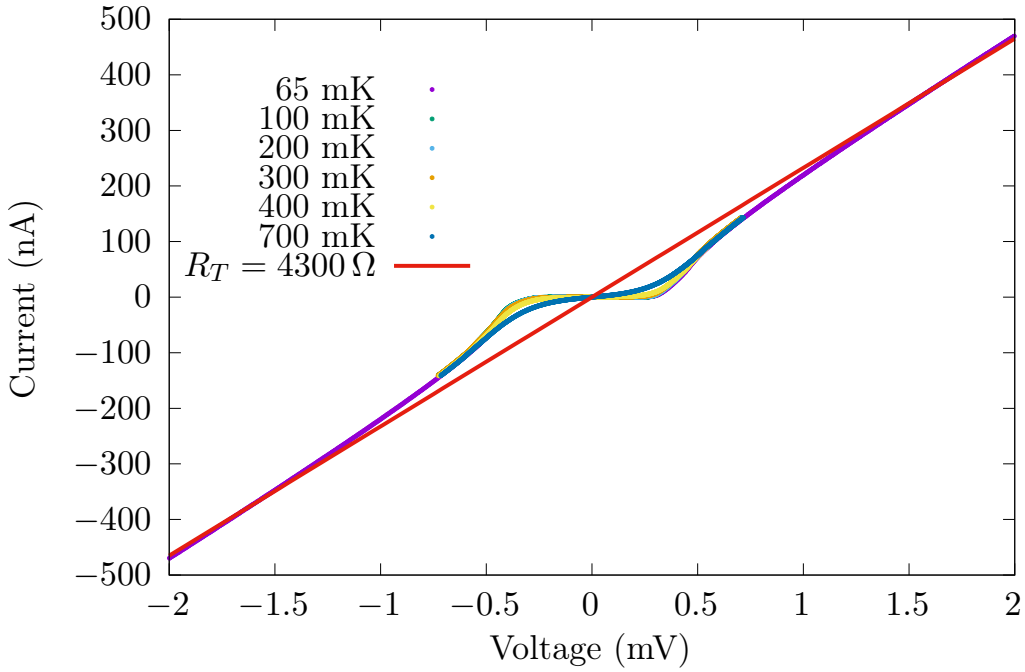

Figure 25. IV curves at various bath temperatures with the largest range measured at 65 mK. R_T was determined by fitting the Ohm's law to the linear part of the 65 mK data.

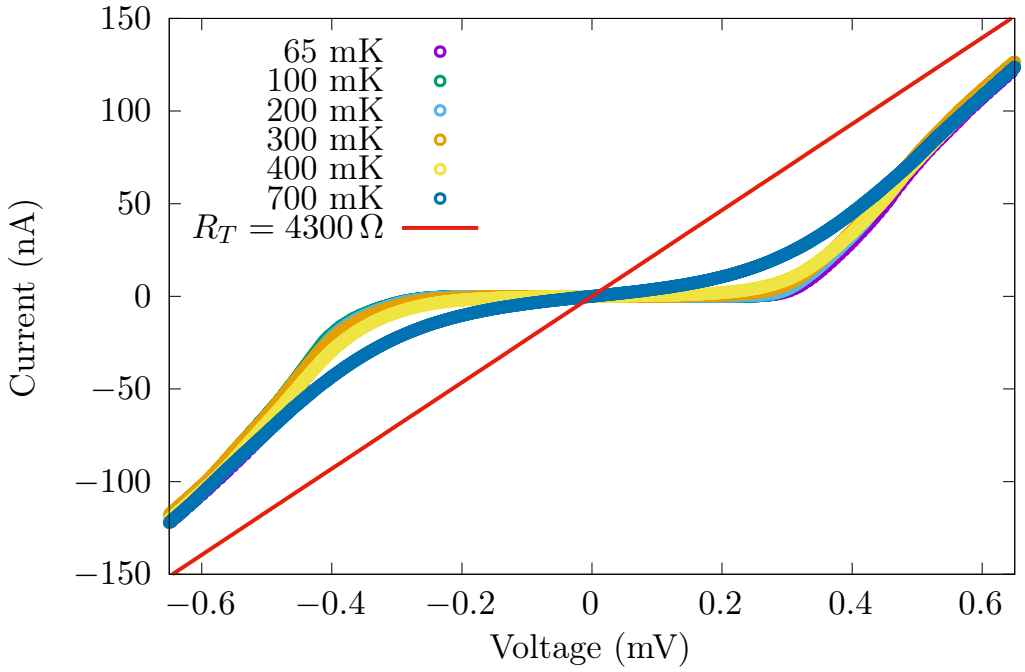

Figure 26. Zoom-in of the SINIS junction current voltage characteristics.

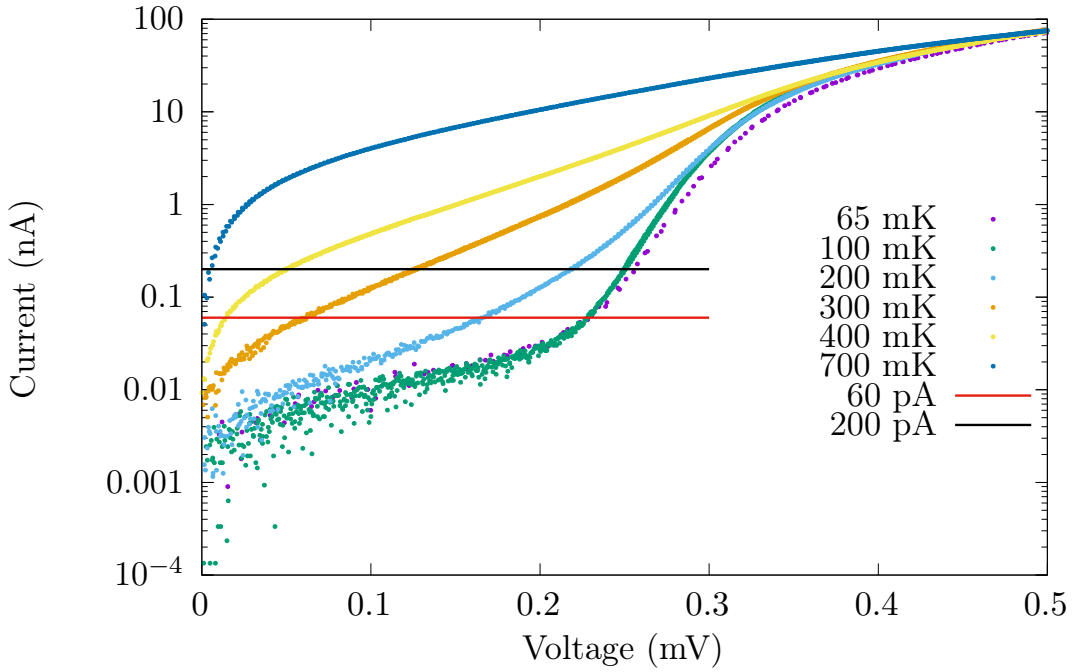

Figure 27. IV data in logarithmic current scale with chosen bias currents denoted with the horizontal lines. Note how much self heating the 65 mK data suffers. It seems to be hotter than the 100 mK data.

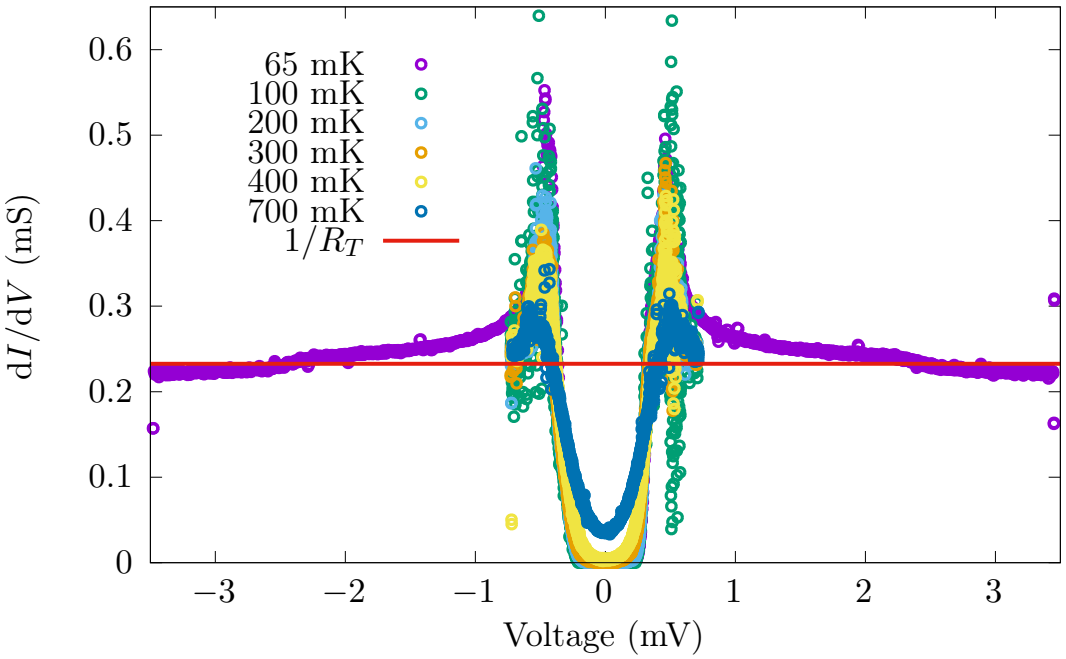

Figure 28. Differential conductance curves at different temperatures with the whole range of the measured data. $R_T = 4300\,\Omega$.

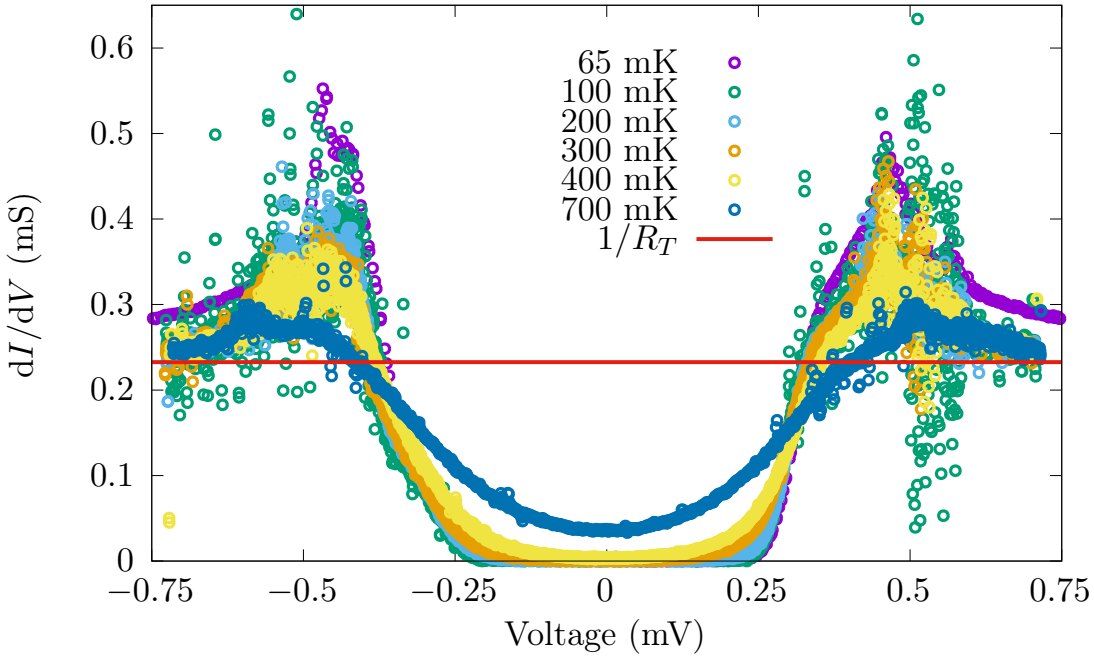

Figure 29. Differential conductance curves at different temperatures, $R_T = 4300\,\Omega$.

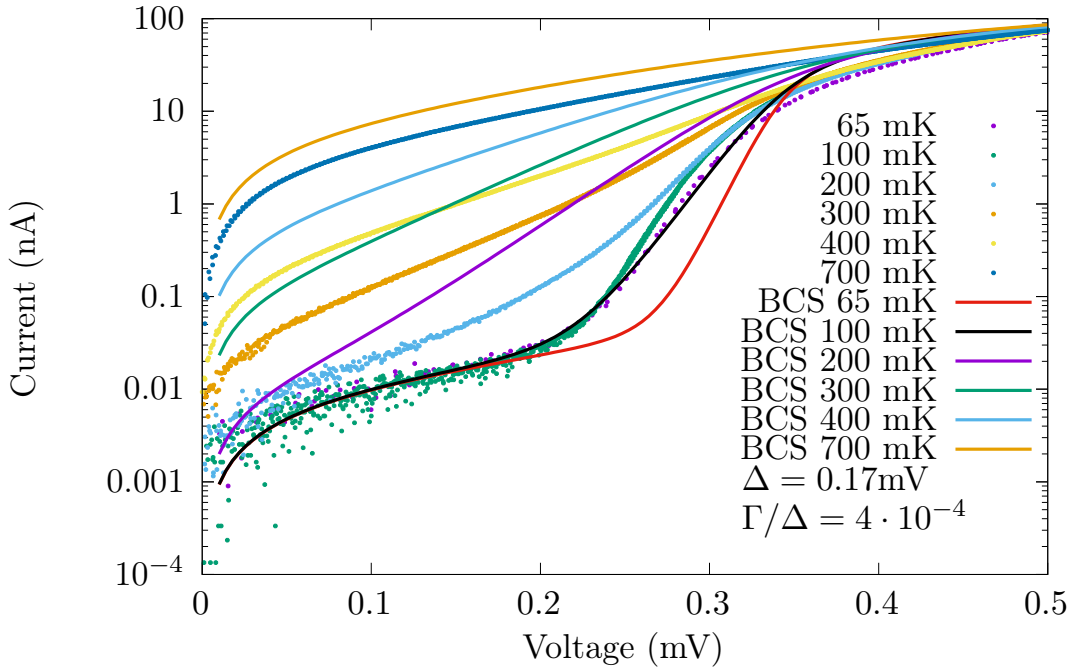

Figure 30. IV curves at different temperatures with BCS theory fits for all measured data. At 200 mK there is clear self cooling of the SINIS junction. Thermal effects were not considered in the fits.

4.2.3 SINIS calibration

The calibration data included the cryostat stage thermometer resistance and the voltage over the SINIS junction. The resistance bridge output voltage was first converted to the physical resistance value by multiplying the value by an appropriate scale factor. Libre Office calc software was used to find the resistance bridge range change points and to multiply the resistance values by a correct scale factor. The resistance was converted to temperature by a Python program written by the author. The program utilized a conversion function including the resistor specific calibration constants provided by Lake Shore. Voltage data was left untouched, since the heating experiment would be done with the same setup, and it was assumed that any offset would remain the same during the calibration and the heating experiment. The calibration data was fed to a different Python program, also written by the author, that read the stage temperature and the SINIS voltage. The data was smoothed by dividing the temperature into discrete intervals and taking averages of the measured temperature and voltage. At the end there were 200 averaged data points representing the calibration curve. A library with Chebyshev polynomials was used to fit a Chebyshev function of 50 orders to the averaged data. A discrete temperature range [0.05 K,1.4 K], corresponding to the maximum and minimum temperature values of the measured data, was fed to the Chebyshev function with the coefficients acquired earlier from the fit. This resulted in a table of generated temperature and SINIS voltage data.

Figure 31 shows the averaged data points with values calculated from the Chebyshev fit for two different bias currents. One might notice that something is wrong with the data, since at higher temperature it seem to go negative. This is simply caused by careless use of the voltage amplifier, so that offset was not zeroed before the calibration run. There is no way to take the offset into account after the calibration was done. However this doesn't affect the calibration, since the real voltage levels are not in principle needed for thermometer usage. The real voltage values could be useful for comparing thermometers, but this comparison is omitted for the first sample. The saturation of electron temperature below $T < 100$ mK was seen already with the IV curves, but also in the calibration curve in Figure 31.

4.2.4 Heating experiment

The SINIS voltage and current and voltage over the SNS heater were recorded during the heating experiment. Again, offset was corrected before performing any further analysis. This time the correction was done by plotting the SINIS voltage, the SNS voltage and the SNS current into same figure and finding the data index of SINIS voltage peak (lowest temperature). At this data index the input power and thus SNS voltage and current should equal zero. This corrected datafile was fed to the previous program with the calibration data. A table of generated temperature and SINIS voltage pairs was used to interpolate the heating experiment SINIS voltage to

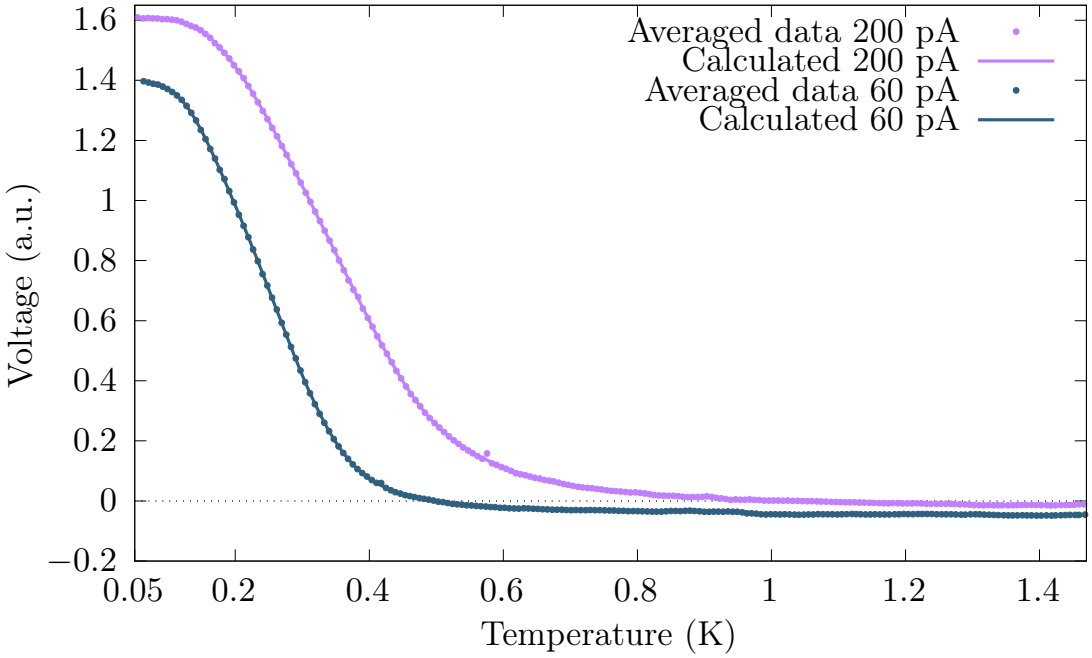

Figure 31. Calibration data with averaged data points and calculated points from the Chebyshev fit. There is some numerical error in the averaged data in both curves, right before 0.6 K for the 200 pA curve and just after 0.4 K for the 60 pA curve. However, this error is insignificant to the fit and thus negligible in final calibration results.

an actual temperature. Then, SNS voltage and current were transformed into SI units in the same manner as in the SINIS case.

In Figure 32, the power vs temperature with a 60 pA SINIS bias current is shown. There is also a simple power law fit and a simulation that follows equation (66) with one overall scale fitting factor. The simulation model assumes that the normal metal heater emits Lamb waves with 2D wave vectors from the heater outer edge, and only phonon modes that have group velocity outwards from the heater surface are taken into account. The power law is is of the form

$$P = A(T^n - T_{bath}^n) - P_{noise}, \tag{79}$$

where A, n and P_{noise} are free parameters to be fitted. The parameter n depends on the phonon gas dimensionality, so that $n = 4$ represents the ideal 3D phonon gas, whereas $n \approx 2.5$–3 would correspond to fully 2D limit, see equation (67). Figure 33 shows the same experiment, but with the 200 pA bias current, extending the sensitive range of the thermometer. It is noteworthy that in both measurements, the power was measured in two probe configuration, so there is an additional resistance from cryostat's wiring. So far there is no accurate estimate of this resistance and thus it is impossible to analyze accurately the data so that it only considers the SNS junction. Approximate power law behavior of the measured curve is as expected from the

Rayleigh-Lamb theory, so the experiment can be declared as partial success at this point. However, it is important to note that the simple power law fits for different SINIS biases gave different values for the parameter A, which depends on the thermal coupling of the heater and the thermometer. So either the coupling changed (unlikely) or the non-idealities of the experimental setup caused the observable coupling to change.

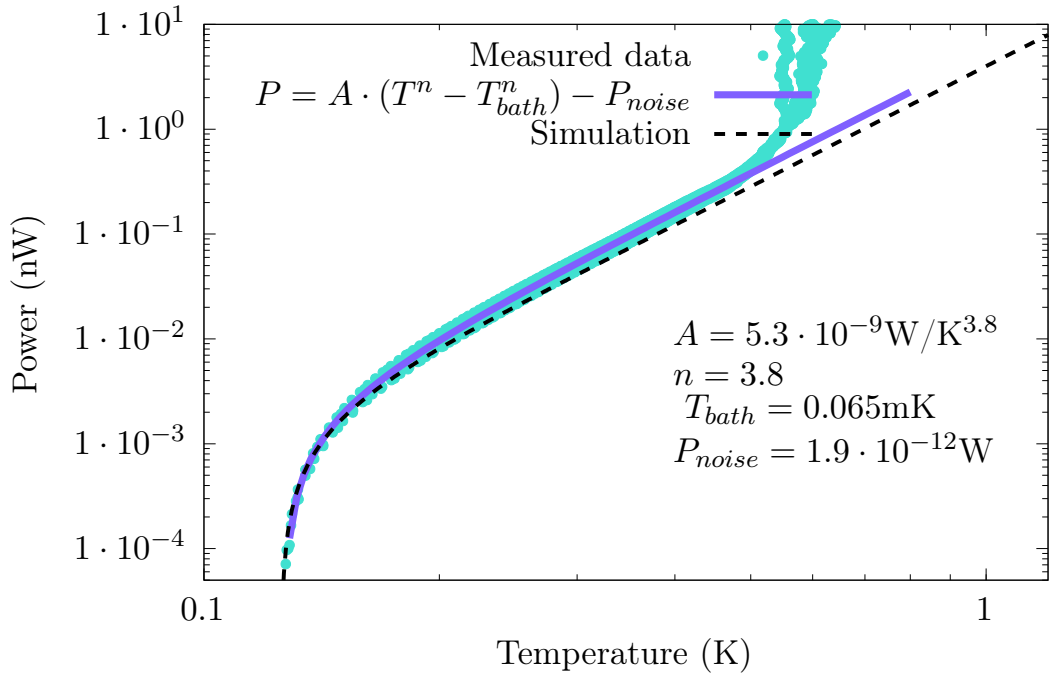

Figure 32. Power vs temperature with 60 pA SINIS bias current, the measured data is accompanied with simple power law fit and a simulation based on Rayleigh-Lamb theory with a fitted scale factor.

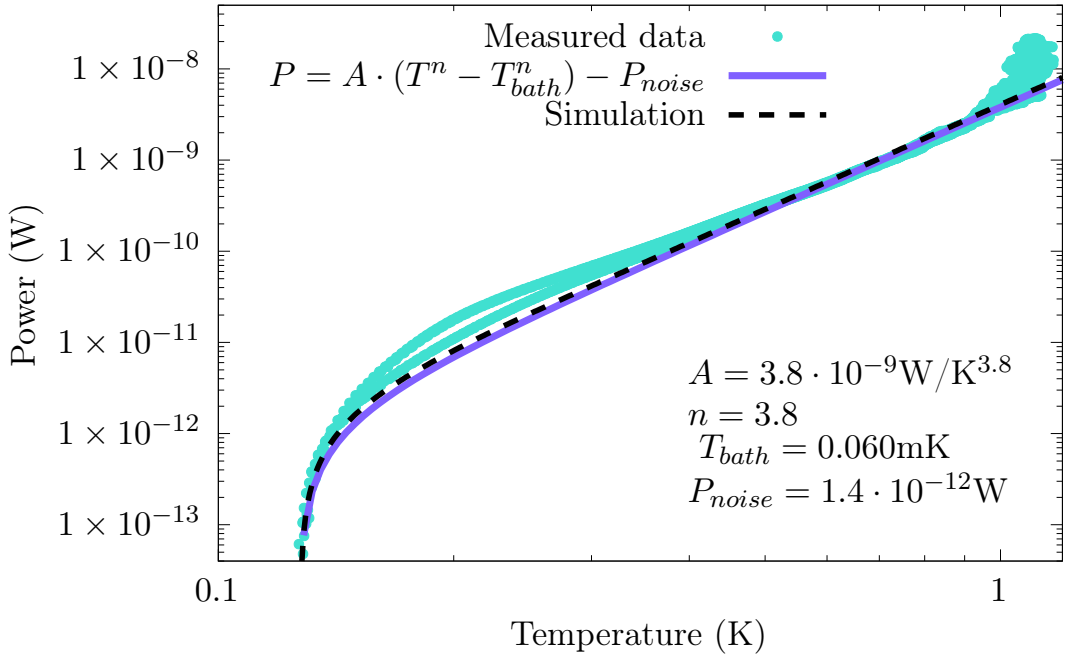

Figure 33. Power vs temperature with 200 pA SINIS bias current, the measured data is accompanied with simple power law fit and a simulation based on Rayleigh-Lamb theory with a fitted scale factor.

For completeness, let's see how these results compare with previous ones. The closest match to this experiment was done on top of a 300 nm thick suspended SiN membrane with a SINIS thermometer and a SINIS heater [13]. Since the heater geometry (SINIS vs SNS) was different, differences are expected, as in the older two SINIS geometry the view factor is different. In Figures 34 and 35 a comparison between the previous results [13] and this work is shown. The results seem to follow the same power law, as expected. However, the newer data seems to be cooler with the same input power, which at a first glance doesn't make any sense. However, remembering that the newer data was capture in a two probe configuration, the cryostat line resistance shifts the newer data to appear hotter than the old data. In Figure 34, 300 Ω of cryostat line resistance is taken into account in the data analysis, but the value was measured in room temperature with a multimeter. The new and the old data seem to follow the same power law, and both have the same feature at the end of the temperature range, where the sample heating gets slower and more noise can be spotted as well. The latter property is seen in samples where TiAu bilayer is used as a normal metal. This bending is not seen in samples with Cu normal metal in reference [13].

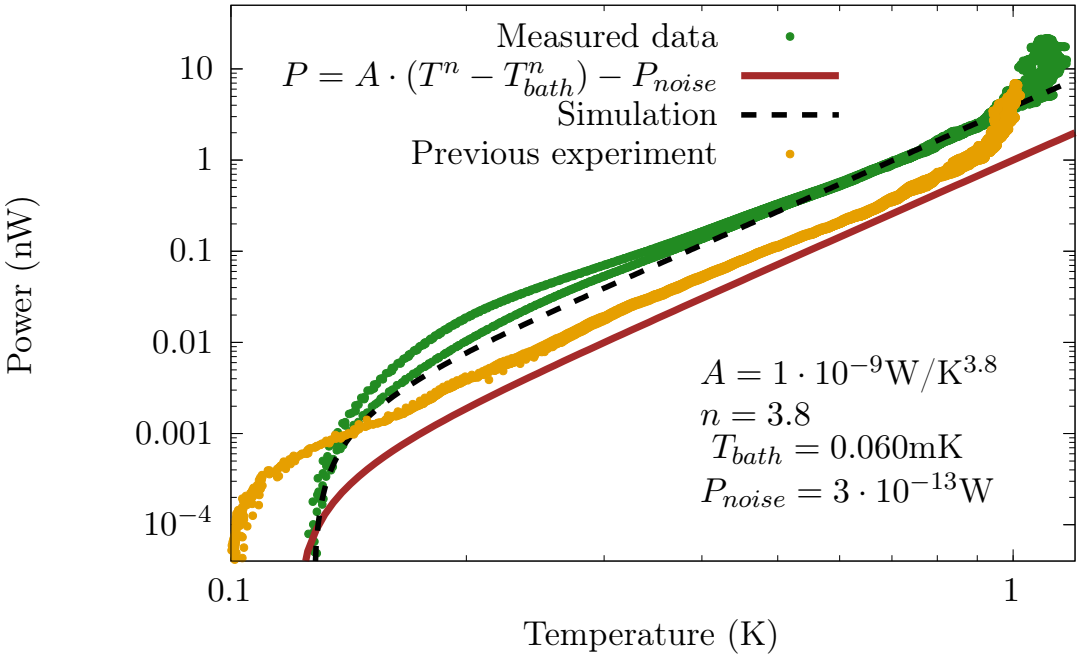

Figure 34. Data acquired during this work and previous measurement performed with SINIS heater and thermometer [13]. The cryostat line resistance was not taken into account in the data analysis.

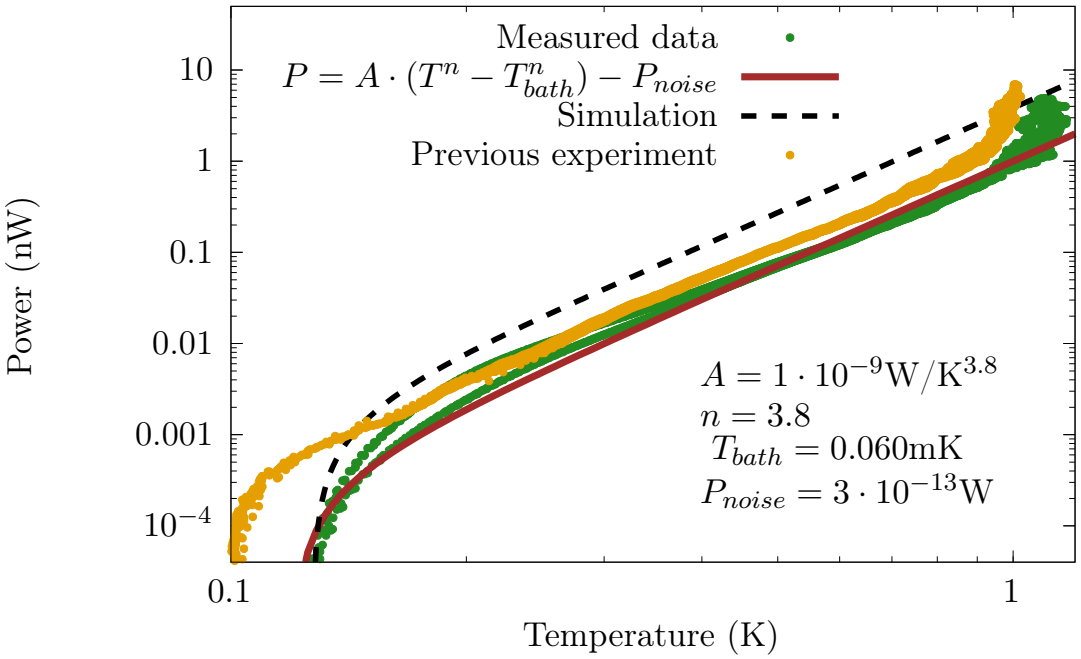

Figure 35. 300 Ω of cryostat line resistance was taken into account in the data analysis of the new data. This makes the results agree more closely with the previous experiment.

One can use data from the heating experiment to calculate the thermal conductance G of the membrane. In this case the calculation was made using two different definitions for thermal conductance, Equation (80) and Equation (81).

$$G = \frac{\mathrm{d}P}{\mathrm{d}T} \tag{80}$$

$$G = \frac{P}{\Delta T} = \frac{P}{T - T_{bath}}. \tag{81}$$

The calculations were made from the data that included the cryostat line resistance. The derivative in Equation 80 was approximated by using a generic central difference method [65].

The results are shown for the 60 pA and the 200 pA SINIS bias currents in Figures 36 and 37, respectively. The differential thermal conductance shows a lot more noise than direct thermal conductance. The explanation for this is that numerical derivatives are notoriously bad for noisy data. To get rid of the noise amplification, one could smooth the data for example by discretizing and averaging the data like was done with the SINIS calibration data. For now, the direct thermal conductance seems easier to analyze and it provides a greater range of reasonably smooth data. It is however important to note, that Equation (81) is valid in the limit where $\Delta T << T_{\mathrm{bath}}$.

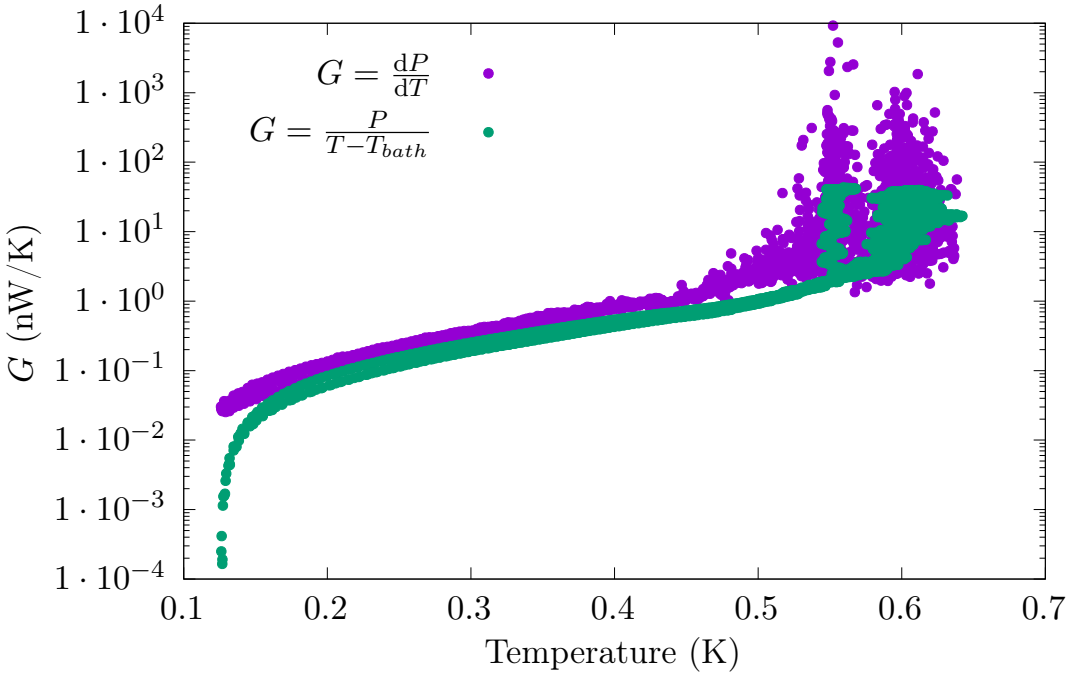

Figure 36. Thermal conductance is calculated from the heating experiment data acquired with 60 pA SINIS bias current through the thermometer. The data was not corrected for the cryostat line resistance. Two different definitions for thermal conductance were used.

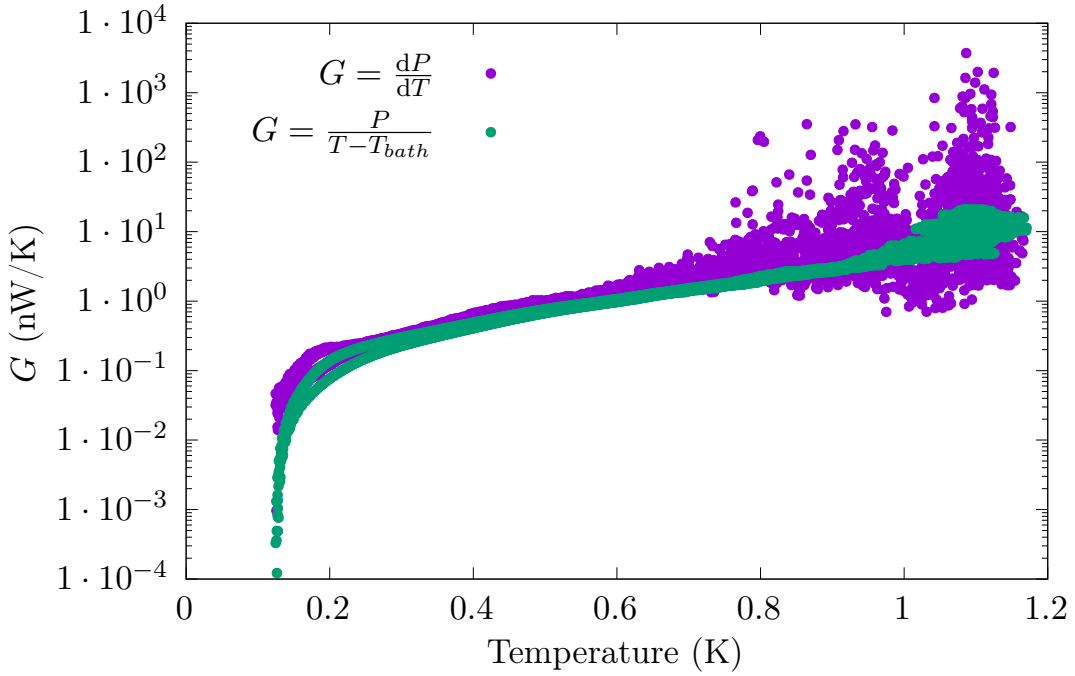

Figure 37. Thermal conductance is calculated from the heating experiment data acquired with 200 pA SINIS bias current through the thermometer. The data was not corrected for the cryostat line resistance. Two different definitions for thermal conductance were used.

4.2.5 SINIS T_c

The final experiment of the first run was conducted to find the critical temperature of the superconducting wires of the SINIS junction. This time the data analysis was a bit different, since the measurement was performed with two lock-in amplifiers. The measured voltage and current values were converted into resistance by using Ohm's law. The temperature was measured by the sample stage germanium thermometer. The cryostat was heated and cooled several times around T_c to obtain more data from that range.

The aluminum wire shows a clear transition at 1.35 K, see Figure 38. The critical temperature was read at a point $R/R_N = 0.5$, where R_N is the normal state resistance, $R = R' - R_S$, R' is the measured resistance and R_S is the resistance measured in the superconducting state (mostly junction resistance). The sharp steps within the transition are caused by different line widths from bonding pads to junction area having slightly different T_cs. Also the wider wires were covered with a normal metal, which causes a shift in T_c due to proximity effect as previously shown with niobium. The measured value for T_c was used in SINIS junction simulations.

There is an interesting feature (minimum in the resistance curve) right after the T_c. For the measured sample the observed feature was reproducible, because that

temperature range was swept multiple times. However, it would be interesting to study this more and find out if the feature is caused by tunnel junction effects or the superconductor itself.

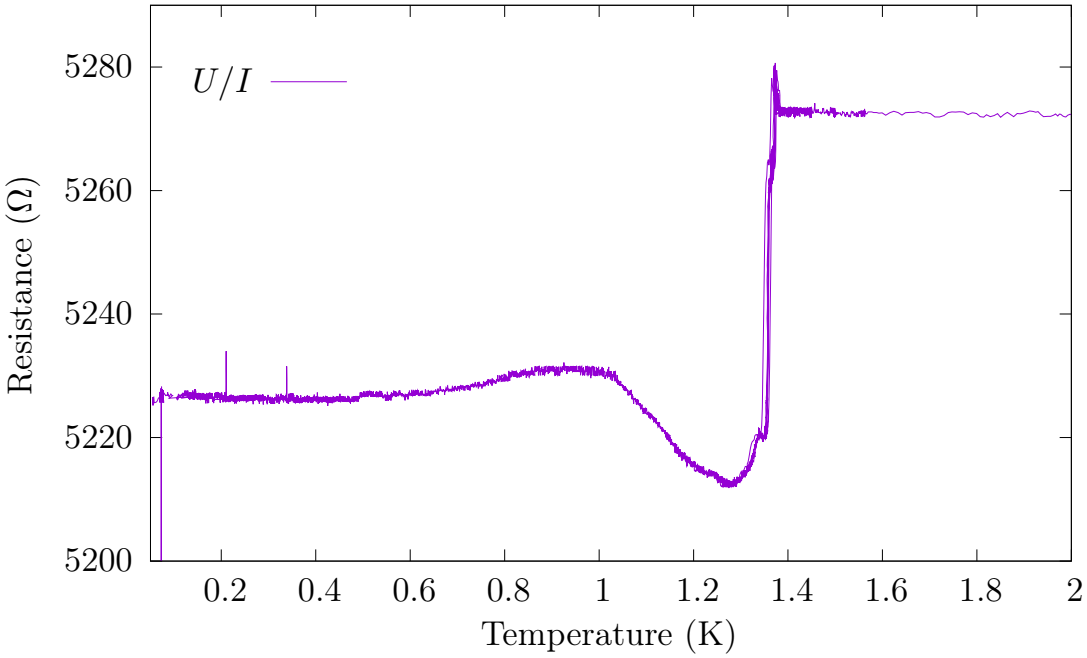

Figure 38. SINIS junction Resistance vs bath temperature. T_c was interpreted to be 1.35 K.

4.3 Data analysis and results of the second measurement run

A second sample was also fabricated using the same methods as with the first one. For the second sample however, the bonding to the cryostat sample stage was more successful with all of the bonds working, giving the capability to use a four probe configuration in the measurements. The cooling was now done with a different cryostat, but the working principle was still the same. The cryostat had some technical issues that had to be fixed before the sample could be measured and finding the real issue with the cryostat required nine cooldowns to 4 K. The tenth cooldown then provided the necessary cooling power for the experiments. The measurements were conducted similarly as before, but now a balanced isolation transformer (Furman IT-2315) was used to isolate all amplifiers from the ground.

4.3.1 SINIS IV curves

The same methods for the offset correction of the data were used here as explained in Section 4.2.2. This time the data had much less noise than in the first measurement as can be seen from Figures 39, 41–42. This is especially seen by comparing the differential conductance in Figures 29 and 41.

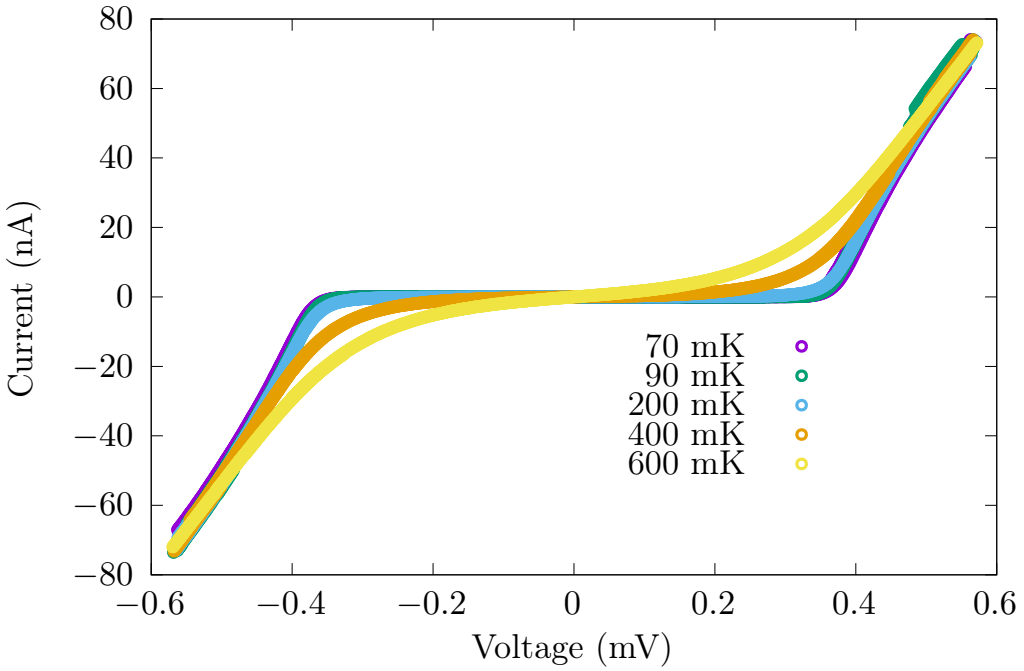

Figure 39. Current vs voltage curves of the SINIS junction measured at different temperatures.

In Figure 40 something strange happens in the bending area of the curve at ±0.5 mV. It seems that different sweeps show a bit different behaviour. This can't be an offset issue, since the offset seems to be correct in other parts of the curve. Ideal BCS theory curves with constant Γ are included in Figure 43. A thermal model would have given more accurate fits for the whole range of temperatures, but a careful tunnel junction study was left out of the scope of this thesis.

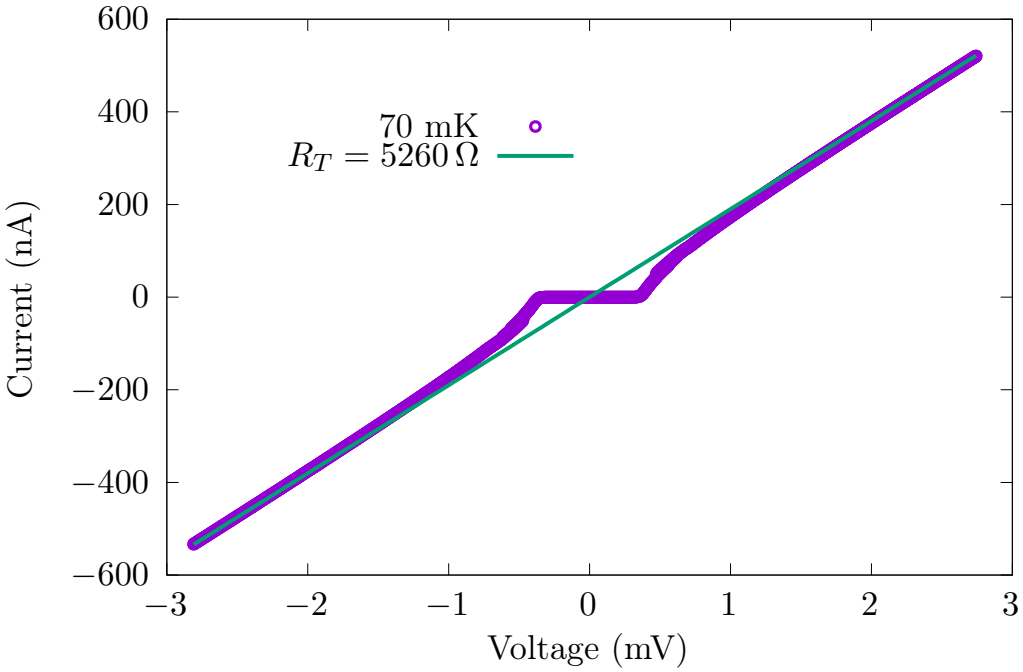

Figure 40. IV curve measured at 70 mK with longer voltage sweep. The tunneling resistance R_T was fitted to linear parts of the data, and the best fit gave $R_T = 5260\,\Omega$.

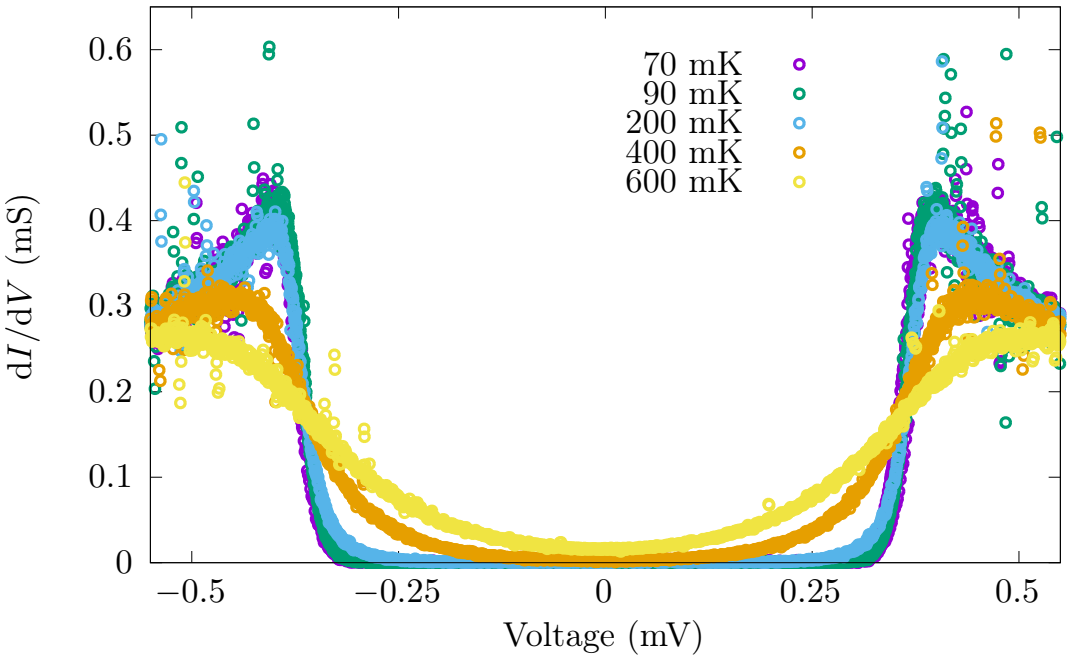

Figure 41. The differential conductance vs voltage with typical SINIS junction features. The second sample shows much cleaner behaviour than the first sample.

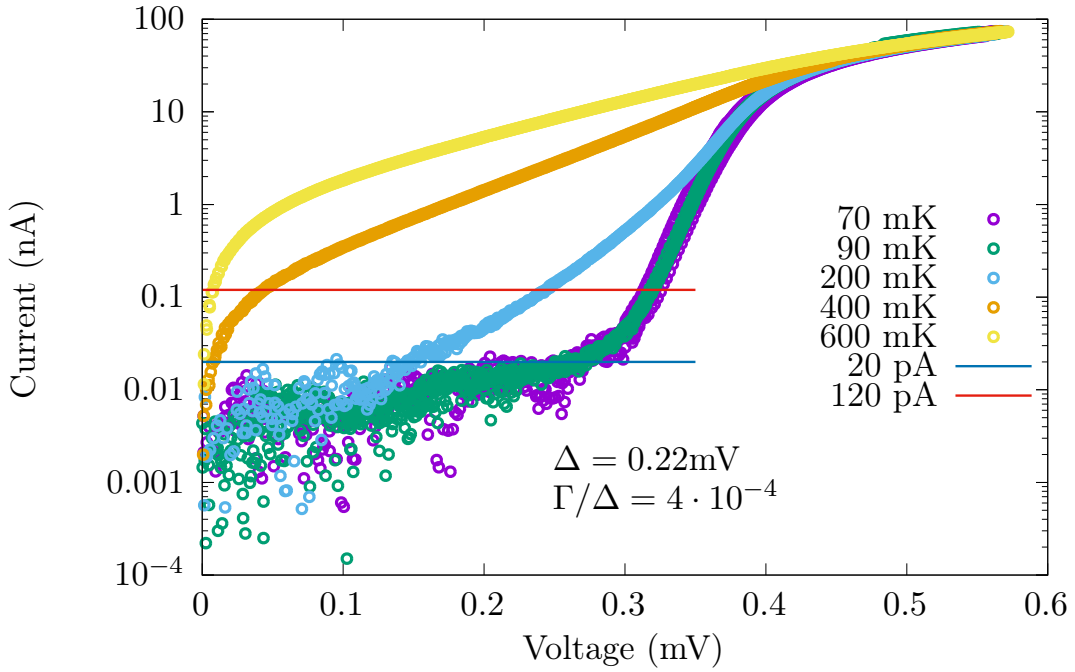

Figure 42. SINIS current voltage characteristics in a logarithmic current scale with two bias current values used in the heating experiment. The lower current bias is a bit too low, since it is already at the temperature independent subgap current level.

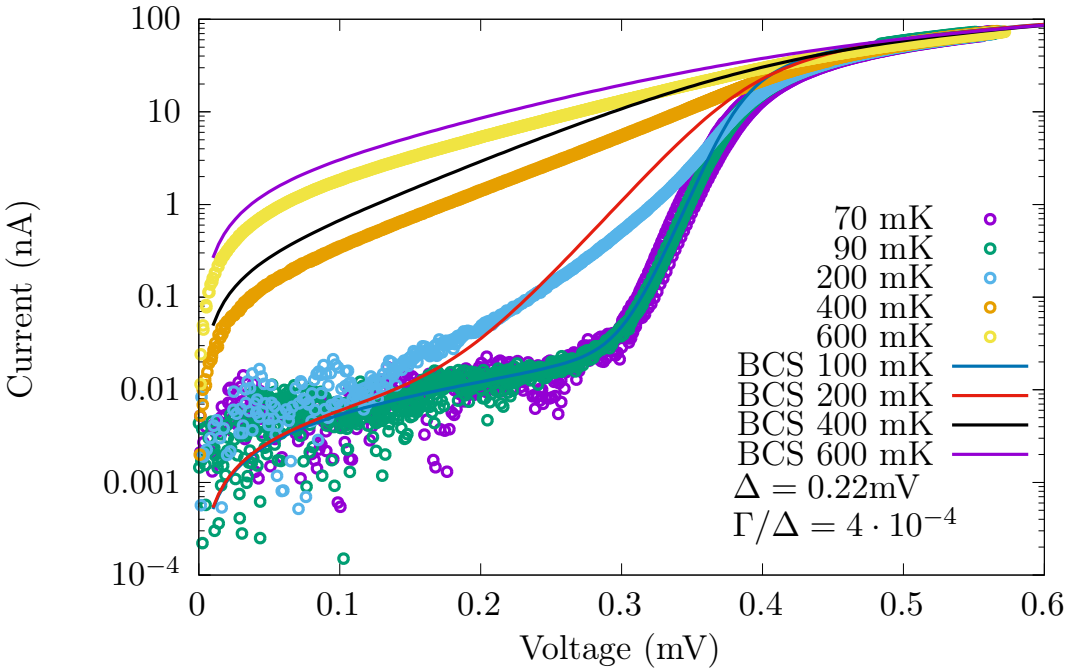

Figure 43. SINIS current voltage characteristics in a logarithmic current scale with simple BCS theory fits at all measured temperatures. SINIS self cooling is clearly visible in the 200 mK data.

4.3.2 SINIS calibration

The thermometer of the second cryostat stage had calibration data where its resistance was compared to a commercially calibrated thermometer. A polynomial fit was done to this data to get a function for converting the measured resistance into temperature. The SINIS junction was biased and a calibration run was performed in the beginning of each heating experiment day. The calibrations for each day in chronological order are presented in Figures 44, 45 and 46. The low temperature saturation seen in run 1 is much more benign in all the data, due to the better grounding principles.

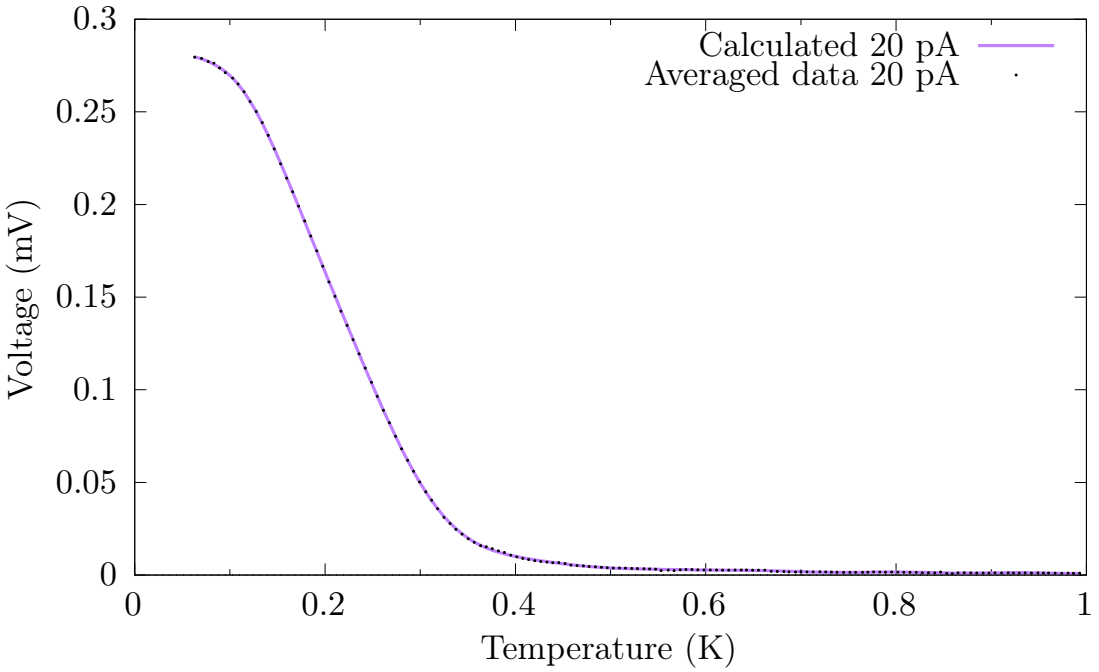

Figure 44. SINIS thermometer calibration curve for 20 pA bias current on the second day of measurements. The black dots are averaged data points and the continuous line is the fit function.

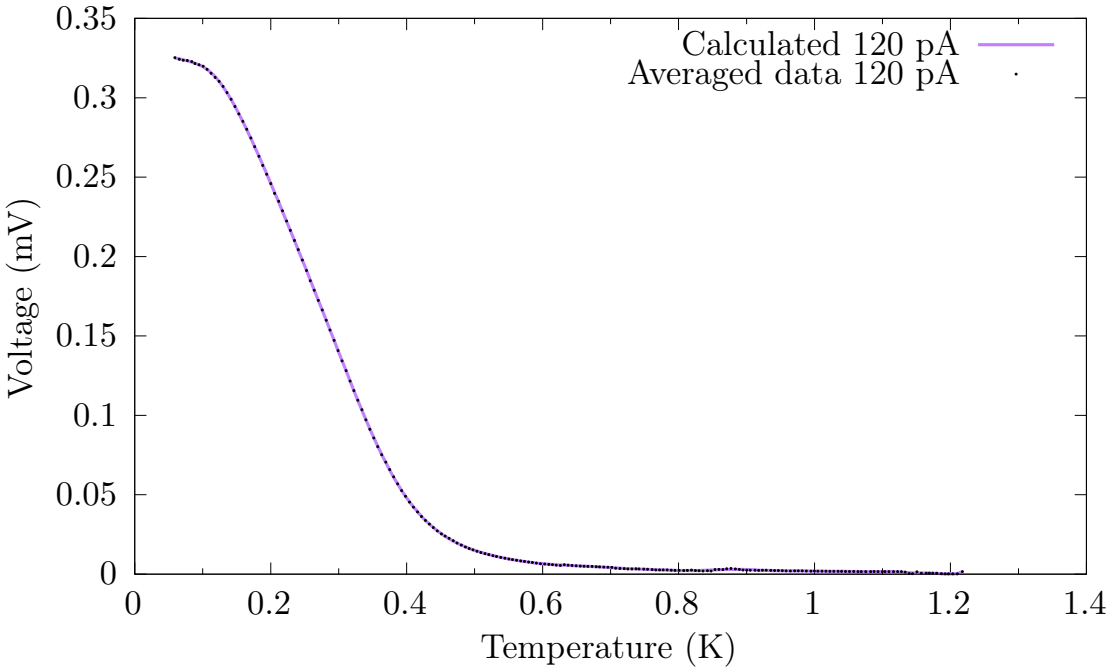

Figure 45. SINIS thermometer calibration curve for 120 pA bias current on the third day of the measurements. The black dots are averaged data points and the continuous line is the fit function.

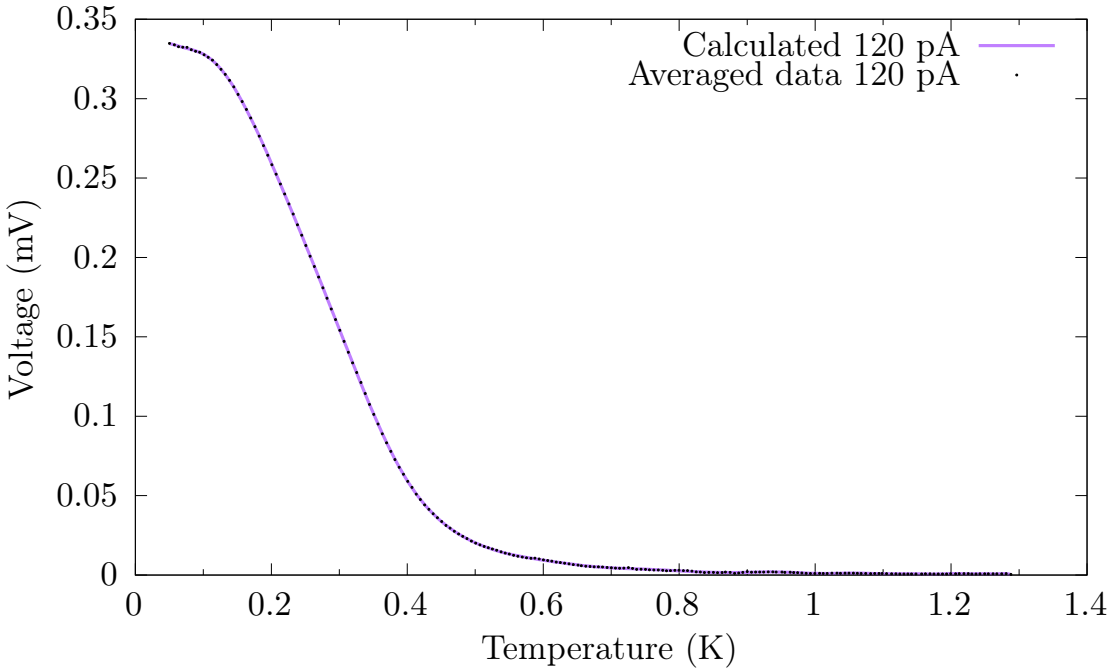

Figure 46. SINIS thermometer calibration curve for 120 pA bias current on the fourth day of measurements. The black dots are averaged data points and the continuous line is the fit function.

4.3.3 Heating experiment

The heating experiments of the second sample suffered from an antisymmetric offset in the SNS junction. The offset had to be zeroed separately for different sweep directions. The difference in the current offset was much larger than the voltage offset that was almost the same for both sweeping directions. For some reason, the voltage sweep box has different sweeping speeds for the rising and descending parts of the triangle wave. If the system has capacitance across the positive and the negative leads then it would explain the difference in the current offset as the current through the capacitor can be expressed as

$$I = C\frac{\mathrm{d}V}{\mathrm{d}t}, \tag{82}$$

where C is the capacitance and $\frac{\mathrm{d}V}{\mathrm{d}t}$ is the rate of change of the voltage.

The results of the heating experiments are shown in Figures 47, 48 and 49. The data in the first figure was acquired using the 20 pA SINIS bias current and the two other measurements were executed with the 120 pA SINIS bias current. A piecewise-defined function was used to fit a power law to the measured data

$$P(T) = \begin{cases} A_1(T^{n_1} - T_{bath}^{n_1}) - P_{noise} & T < 300 \text{ mK} \\ A_2(T^{n_2} - T_{bath}^{n_2}) & T > 300 \text{ mK}. \end{cases} \tag{83}$$

The fitting was done in pieces, because there is a small bend visible at $T = 300$ mK in the data. The best fit values for the parameters are presented in Tables 2 and 3 for the 20 pA SINIS bias measurement and the 120 pA SINIS bias measurements, respectively. The only difference in the fits is that a cooling effect present in the higher SINIS bias measurements caused the parameter P_{noise} to be negative, whereas in the lower SINIS bias measurement, the parameter was positive due to noise heating. This gives confidence in the new heater geometry, since essentially the only differences between the measurements are seen near the bath temperature and the most sensitive temperature range of the SINIS thermometer gives same results with different current biases. In addition, no drifting between measurement days was noticed in that temperature range.

One anomaly in the data is still mind boggling. The hotter end of the temperature range shows no consistent behaviour. Even if the thermometer is not very sensitive at the higher end of the temperature range, one would still expect similar behaviour between the measurements. In the first dataset (Figure 47), the hotter tail of the data tapers down as if there was an extra heating coming from somewhere. The second dataset (Figure 48) shows no anomalies at the hotter end of the data, and the third one (Figure 49) shows a cooling effect at the hotter end of the data.

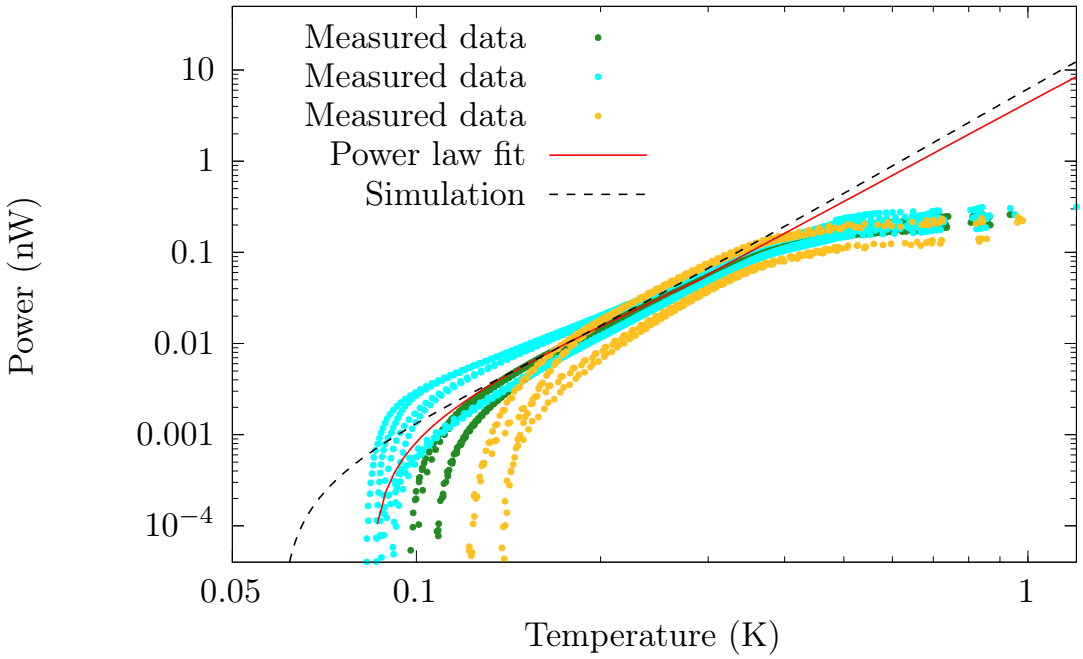

Figure 47. Power vs temperature measured with three different voltage dividers corresponding to different colors. Also the power law fit and a simulation based on Equation (84) are included.

Table 2. The power law fitting parameters for data shown in Figure 47.

Parameter	value
T_{bath}	0.070
A_1	$2.2{\cdot}10^{-9}$
A_2	$4.4{\cdot}10^{-9}$
P_{noise}	$0.5{\cdot}10^{-12}$
n_1	3.0
n_2	3.6

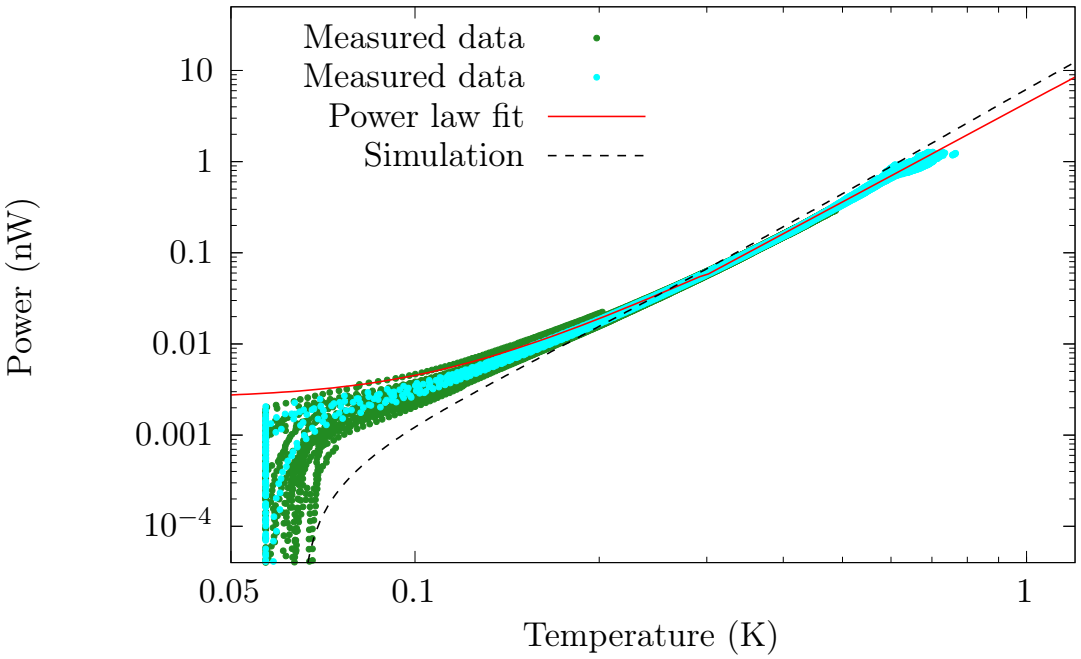

Figure 48. Power vs temperature with two different voltage dividers corresponding to different colors. Also the power law fit and a simulation based on Equation (84) are included. Here it is interesting to see the cooling effect starting from 200–300 mK.

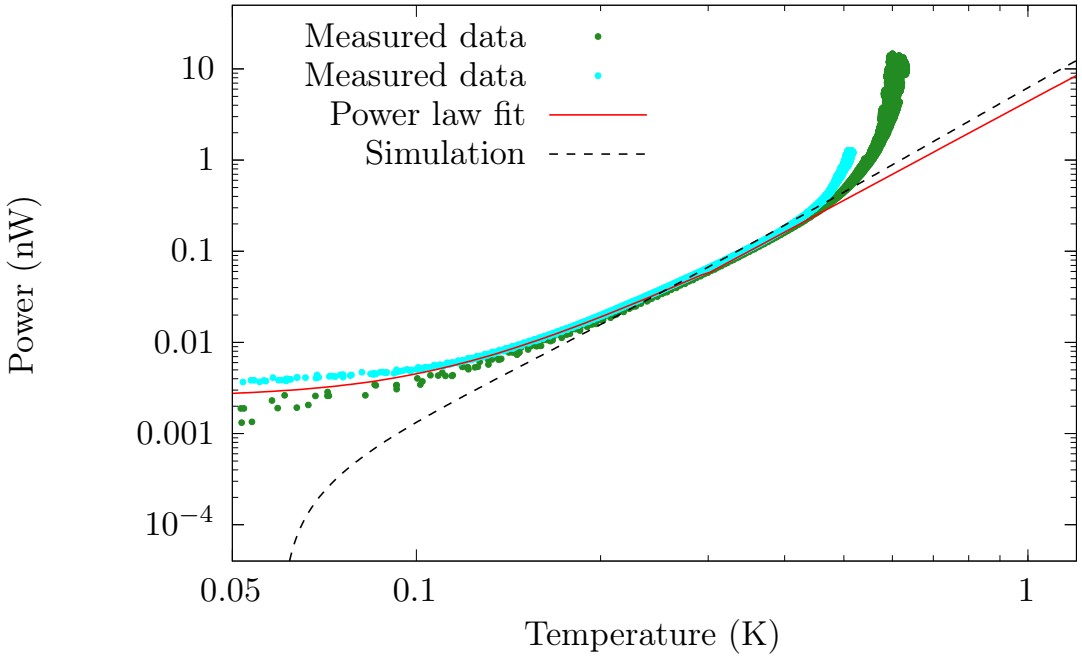

Figure 49. Power vs temperature with two different voltage dividers corresponding to different colors. Also the power law fit and a simulation based on Equation (84) are included. Here it is interesting to see the cooling effect starting from 200–300 mK. Note that the cooling is stronger in this dataset. The only difference with this data and the data shown in Figure 48 is the day of the measurement.

Table 3. The power law fitting parameters for data shown in Figures 48 and 49.

Parameter	value
T_{bath}	0.070
A_1	$2.2{\cdot}10^{-9}$
A_2	$4.4{\cdot}10^{-9}$
P_{noise}	$-3.2{\cdot}10^{-12}$
n_1	3.0
n_2	3.6

A simulation is also included in the power vs temperature plots. It is based on equation (66), but with a slight modification. The model now considers a normal metal wire on top of the membrane, whereas before it was thought to excite phonons uniformly across the membrane. A pictorial representation of the model is given in Figure 50. The new model in a form of an equation is

$$P(T) = \frac{1}{(2\pi)^2} \sum_j \oint_l \mathrm{d}l \int_K \mathrm{d}\vec{k} \hbar\omega_j(\vec{k}) n(\omega_j, T) \left| \frac{\partial \omega_j(\vec{k})}{\partial \vec{k}} \right|. \tag{84}$$

Effectively, the modification just multiplies the power by a factor of $\pi/2$.

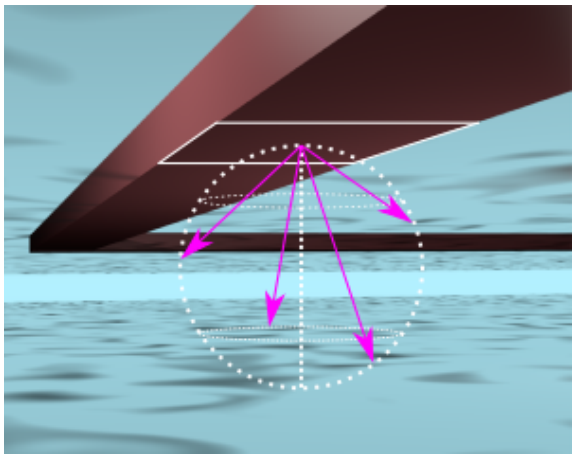

Figure 50. An updated model, where the normal metal heater is on top of the membrane. The model is viewed from inside of the membrane. The purple arrows represent the wave vectors and they are rotationally symmetric. The figure was kindly produced by Dr. Tuomas Puurtinen.

The updated simulation model was also tested with data from the older experiments [13]. The model still doesn't fit to the data directly, but a scaling factor would fix the issue [12], so the new model alone doesn't really improve the results with the old geometry. However, for the two SINIS geometry in [12, 13], a view factor correction has to be applied as well [14].

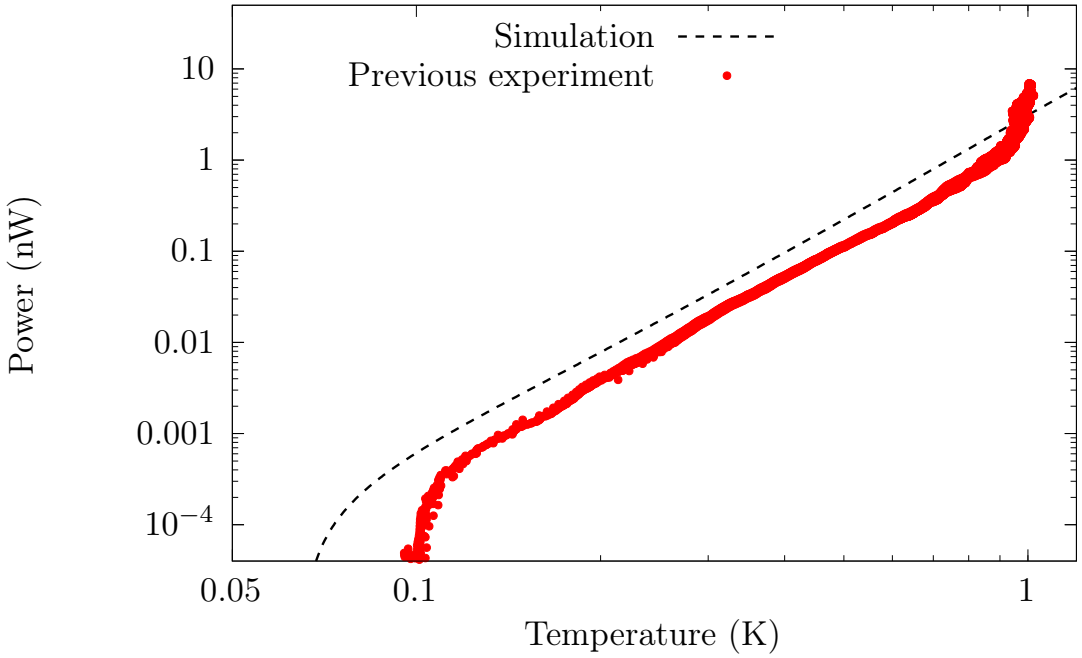

Figure 51. Data from the older experiment [13] with a simulation where the new model was used.

The thermal conductance was calculated from the data in a similar manner as with the first sample. The results are shown in Figures 52, 53 and 54. Again, the differential conductance fluctuates much more than the direct thermal conductance. The numerical derivative used to calculate the differential thermal conductance emphasizes the noise in the original dataset. Interestingly, the two thermal conductances cross at around 200 mK in every dataset.

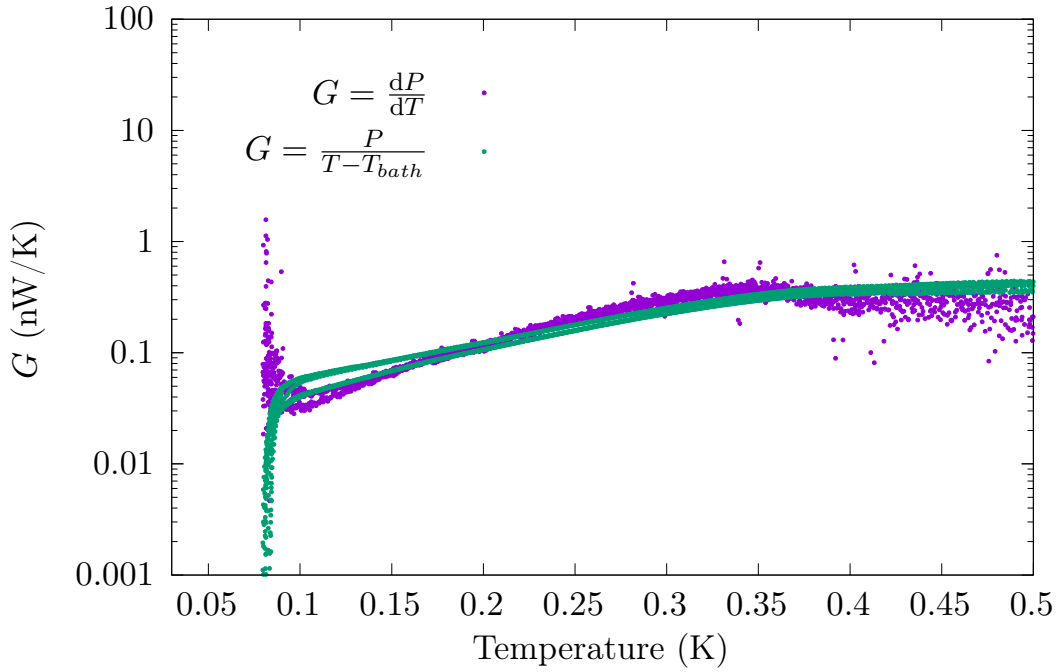

Figure 52. Thermal conductance is calculated from the heating experiment data acquired with a 20 pA SINIS bias current through the thermometer (green data in Figure 47). Two different definitions for thermal conductance were used.

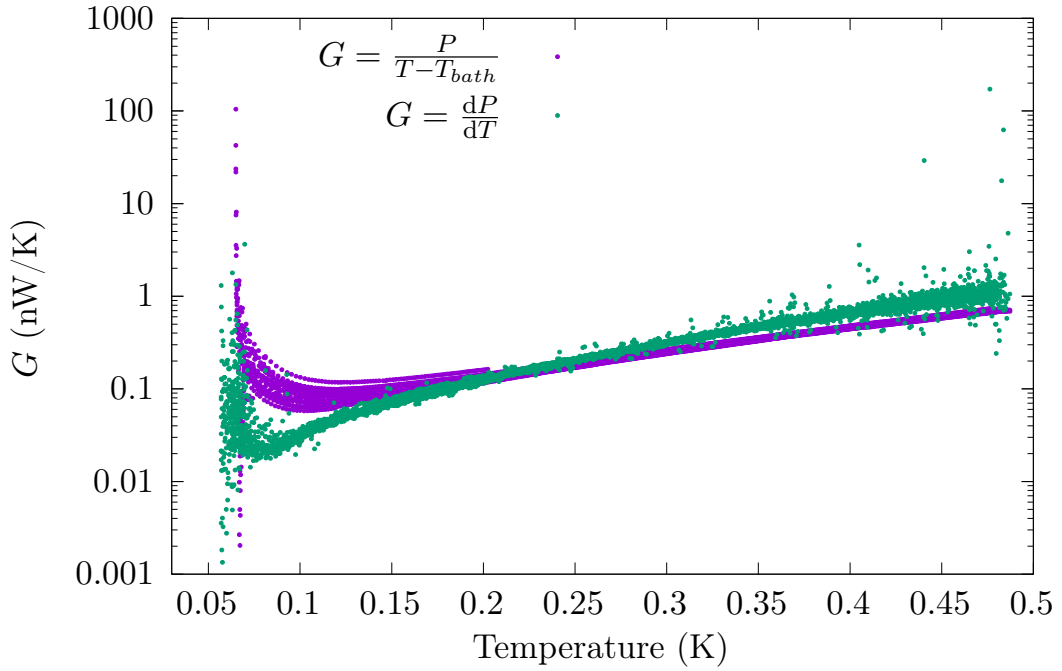

Figure 53. Thermal conductance is calculated from the heating experiment data acquired with a 120 pA SINIS bias current through the thermometer (cyan data in Figure 48). Two different definitions for thermal conductance were used.

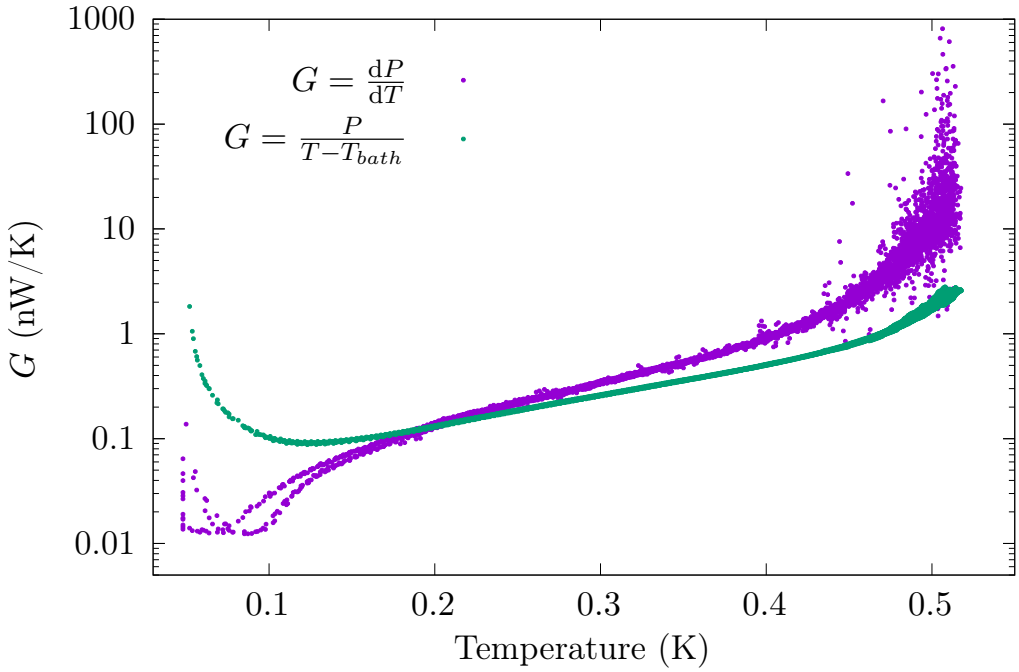

Figure 54. Thermal conductance is calculated from the heating experiment data acquired with a 120 pA SINIS bias current through the thermometer (cyan data in Figure 49). Two different definitions for thermal conductance were used.

5 Conclusions

A new heater geometry was designed, fabricated and tested. The starting point for the sample design was to make the analysis of the heating experiment easier. The heater element was designed in a way that the thermometer would thermalize better to the phononic temperature of the heater that is measured.

Many technical fabrication issues were solved during the fabrication process and also the design was updated many times to take all changes in the fabrication process into account. I hope that all issues with the sample fabrication presented in this thesis won't be bothering the ''next guy'' who starts a similar fabrication process development. Solutions for different fabrication issues were carefully explained here, so that anyone that encounters the same problems could quickly get a fix for them.

The first heating experiment measurement was not very successful, but it served as a good learning experience for the author. Also the first sample gave some indications of improvement over the old geometry. Some issues with the first measurements were caused by the fact that and all measurements were performed in two probe configuration. In addition, there was an issue with noise leaking into the measurement from the ground.

The experimental proof of the new heater geometry was obtained in the second measurement with a new sample. All technical issues experienced in the first measurement were fixed for the second measurement. The measurement went as planned for the most part. After the data was analyzed, it turned out that the new geometry works better than the old one. Also a kick-off for updating the current simulation model for heat transport was made. The experimental results were replicated by the updated simulation model without any scaling factors, which have always been used in the past to fit the simulation to the experimental data. More experiments with different membrane thicknesses are still needed to give more statistics. For now, a 100% conclusive statement about the matter cannot be made.

Most theoretical aspects of this thesis have been closely linked to experimental results gathered by the author and previous group members. Constant testing of theories is the backbone of experimental physics and I dare to say that this thesis has managed to test a wide range of theories from superconducting proximity effect to heat trasport of dielectric membranes. Another important job for experimentalists is to develop better methods for testing theories, and this thesis has at least set in motion a novel technique for heat transport studies.

References

[1] I. J. Maasilta et al. ‘‘Phononic Thermal Conduction Engineering for Bolometers: From Phononic Crystals to Radial Casimir Limit’’. In: *Journal of Low Temperature Physics* 184.1-2 (Nov. 2015), pp. 211–216. DOI: 10.1007/s10909-015-1372-0. URL: https://doi.org/10.1007/s10909-015-1372-0.

[2] K. Rostem, P. J. de Visser, and E. J. Wollack. ‘‘Enhanced quasiparticle lifetime in a superconductor by selective blocking of recombination phonons with a phononic crystal’’. In: *Physical Review B* 98.1 (July 2018). DOI: 10.1103/physrevb.98.014522. URL: https://doi.org/10.1103/physrevb.98.014522.

[3] Jonas Zmuidzinas. ‘‘Superconducting Microresonators: Physics and Applications’’. In: *Annual Review of Condensed Matter Physics* 3.1 (Mar. 2012), pp. 169–214. DOI: 10.1146/annurev-conmatphys-020911-125022. URL: https://doi.org/10.1146/annurev-conmatphys-020911-125022.

[4] Xudong Wu et al. ‘‘An investigation on interior noise reduction using 2D locally resonant phononic crystal with point defect on car ceiling’’. In: *Journal of Vibration and Control* (June 2018), p. 107754631878224. DOI: 10.1177/1077546318782242. URL: https://doi.org/10.1177/1077546318782242.

[5] Kevin O’Brien et al. ‘‘Ultrafast acousto-plasmonic control and sensing in complex nanostructures’’. In: *Nature Communications* 5.1 (June 2014). DOI: 10.1038/ncomms5042. URL: https://doi.org/10.1038/ncomms5042.

[6] D. Hatanaka et al. ‘‘Phonon waveguides for electromechanical circuits’’. In: *Nature Nanotechnology* 9.7 (June 2014), pp. 520–524. DOI: 10.1038/nnano.2014.107. URL: https://doi.org/10.1038/nnano.2014.107.

[7] V. N. Smelyankiy et al. ‘‘Donor Spin Qubits in Ge-based Phononic Crystals’’. In: (Sept. 2014). URL: https://arxiv.org/abs/1409.6285.

[8] Charles M. Reinke and Ihab El-Kady. ‘‘Phonon-based scalable platform for chip-scale quantum computing’’. In: *AIP Advances* 6.12 (Dec. 2016), p. 122002. DOI: 10.1063/1.4972568. URL: https://doi.org/10.1063/1.4972568.

[9] Rick Leijssen et al. ‘‘Nonlinear cavity optomechanics with nanomechanical thermal fluctuations’’. In: *Nature Communications* 8 (July 2017), ncomms16024. DOI: 10.1038/ncomms16024. URL: https://doi.org/10.1038/ncomms16024.

[10] Martin Maldovan. ‘‘Sound and heat revolutions in phononics’’. In: *Nature* 503.7475 (Nov. 2013), pp. 209–217. DOI: 10.1038/nature12608. URL: https://doi.org/10.1038/nature12608.

[11] Yan Pennec et al. ‘‘Two-dimensional phononic crystals: Examples and applications’’. In: *Surface Science Reports* 65.8 (Aug. 2010), pp. 229–291. DOI:

10.1016/j.surfrep.2010.08.002. URL: https://doi.org/10.1016/j.surfrep.2010.08.002.

[12] Nobuyuki Zen et al. ''Engineering thermal conductance using a two-dimensional phononic crystal''. In: *Nature Communications* 5.1 (Mar. 2014). DOI: 10.1038/ncomms4435. URL: https://doi.org/10.1038/ncomms4435.

[13] Yaolan Tian. ''Studies of two-dimensional and three-dimensional phononic crystal stuctures''. PhD thesis. 2016.

[14] Yaolan Tian et al. ''Minimizing coherent thermal conductance by controlling the periodicity of two-dimensional phononic crystals''. Submitted. 2019.

[15] Teemu Loippo. ''2D phononic crystal fabrication using neon ion beam milling''. Research training report. 2017.

[16] Antti Peltonen et al. ''Milling a silicon nitride membrane by focused ion beam''. In: *Journal of Vacuum Science & Technology B, Nanotechnology and Microelectronics: Materials, Processing, Measurement, and Phenomena* 34.6 (Nov. 2016), p. 062201. DOI: 10.1116/1.4963895. URL: https://doi.org/10.1116/1.4963895.

[17] M. Sledzinska et al. ''Fabrication of phononic crystals on free-standing silicon membranes''. In: *Microelectronic Engineering* 149 (Jan. 2016), pp. 41–45. DOI: 10.1016/j.mee.2015.09.004. URL: https://doi.org/10.1016/j.mee.2015.09.004.

[18] Jeremie Maire et al. ''Heat conduction tuning by wave nature of phonons''. In: *Science Advances* 3.8 (Aug. 2017), e1700027. DOI: 10.1126/sciadv.1700027. URL: https://doi.org/10.1126/sciadv.1700027.

[19] Jinyao Tang et al. ''Holey Silicon as an Efficient Thermoelectric Material''. In: *Nano Letters* 10.10 (Oct. 2010), pp. 4279–4283. DOI: 10.1021/nl102931z. URL: https://doi.org/10.1021/nl102931z.

[20] Tuomas Puurtinen and Ilari Maasilta. ''Low-Temperature Coherent Thermal Conduction in Thin Phononic Crystal Membranes''. In: *Crystals* 6.6 (June 2016), p. 72. DOI: 10.3390/cryst6060072. URL: https://doi.org/10.3390/cryst6060072.

[21] T. A. Puurtinen and I. J. Maasilta. ''Low temperature heat capacity of phononic crystal membranes''. In: *AIP Advances* 6.12 (Dec. 2016), p. 121902. DOI: 10.1063/1.4968619. URL: https://doi.org/10.1063/1.4968619.

[22] T. Kühn J. T. Karvonen and I. J. Maasilta. ''Temperature profile for ballistic and diffusive phonon transport ia a suspended membrane with a radially symmetric heat source''. In: *Chin. Journal Phys.* 49.435 (Aug. 2011). URL: https://arxiv.org/abs/1008.3230v2.

[23] H K Onnes. In: *Leiden Comm. 120b, 122b, 124c* (1911).

[24] W. Meissner and R. Ochsenfeld. ''Ein neuer Effekt bei Eintritt der Supraleitfähigkeit''. In: *Die Naturwissenschaften* 21.44 (Nov. 1933), pp. 787–788. DOI: 10.1007/bf01504252. URL: https://doi.org/10.1007/bf01504252.

[25] Michael Tinkham. *Introduction to superconductivity*. Dover, 2004.

[26] C. J. Gorter and H. B. G. Casimir. In: *Zeitschrift für Physik* 963.35 (1934).

[27] J. Bardeen, L. N. Cooper, and J. R. Schrieffer. ‘‘Theory of Superconductivity’’. In: *Physical Review* 108.5 (Dec. 1957), pp. 1175–1204. DOI: 10.1103/physrev.108.1175. URL: https://doi.org/10.1103/physrev.108.1175.

[28] Geng Zhuoran. ‘‘Development of an inductive NIS thermometer’’. MA thesis. University of Jyväskylä, 2012.

[29] K. Mendelssohn and J. L. Olsen. ‘‘Anomalous Heat Flow in Superconductors’’. In: *Physical Review* 80.5 (Dec. 1950), pp. 859–862. DOI: 10.1103/physrev.80.859. URL: https://doi.org/10.1103/physrev.80.859.

[30] A. F. Andreev. ‘‘Thermal conductivity of the intermediate state of superconductors’’. In: *Soviet physics JETP* 19.5 (May 1964), pp. 1228–1231.

[31] A. F. Andreev. ‘‘Thermal conductivity of the intermediate state of superconductors II’’. In: *Soviet physics JETP* 20.6 (June 1965), pp. 1490–1493.

[32] G. E. Blonder, M. Tinkham, and T. M. Klapwijk. ‘‘Transition from metallic to tunneling regimes in superconducting microconstrictions: Excess current, charge imbalance, and supercurrent conversion’’. In: *Physical Review B* 25.7 (Apr. 1982), pp. 4515–4532. DOI: 10.1103/physrevb.25.4515.

[33] S. Guéron et al. ‘‘Superconducting Proximity Effect Probed on a Mesoscopic Length Scale’’. In: *Physical Review Letters* 77.14 (Sept. 1996), pp. 3025–3028. DOI: 10.1103/physrevlett.77.3025. URL: https://doi.org/10.1103/physrevlett.77.3025.

[34] John M Martinis et al. ‘‘Calculation of TC in a normal-superconductor bilayer using the microscopic-based Usadel theory* 1’’. In: *Nuclear Instruments and Methods in Physics Research Section A: Accelerators, Spectrometers, Detectors and Associated Equipment* 444 (Apr. 2000). DOI: 10.1016/S0168-9002(99)01320-0.

[35] T. Hoss et al. ‘‘Multiple Andreev reflection and giant excess noise in diffusive superconductor/normal-metal/superconductor junctions’’. In: *Physical Review B* 62.6 (Aug. 2000), pp. 4079–4085. DOI: 10.1103/physrevb.62.4079. URL: https://doi.org/10.1103/physrevb.62.4079.

[36] Wolfgang Belzig et al. ‘‘Quasiclassical Green’s function approach to mesoscopic superconductivity’’. In: *Superlattices and Microstructures* 25.5-6 (May 1999), pp. 1251–1288. DOI: 10.1006/spmi.1999.0710. URL: https://doi.org/10.1006/spmi.1999.0710.

[37] K. K. Likharev. ‘‘Superconducting weak links’’. In: *Reviews of Modern Physics* 51.1 (Jan. 1979), pp. 101–159. DOI: 10.1103/revmodphys.51.101. URL: https://doi.org/10.1103/revmodphys.51.101.

[38] David R. Lide. *Handbook of Chemistry and Physics (72nd Edition)*. CRC Press, 1991. ISBN: 0849304725.

[39] Neil W. Ashcroft and N. David Mermin. *Solid State Physics*. Cengage Learning, 1976. ISBN: 0030839939.

[40] R. C. Dynes, V. Narayanamurti, and J. P. Garno. ‘‘Direct Measurement of Quasiparticle-Lifetime Broadening in a Strong-Coupled Superconductor’’. In: *Physical Review Letters* 41.21 (Nov. 1978), pp. 1509–1512. DOI: 10.1103/

physrevlett.41.1509. URL: https://doi.org/10.1103/physrevlett.41.1509.

[41] Charles Kittel. *Introduction to Solid State Physics*. John Wiley & Sons, 1958. ISBN: 0471111813.

[42] J. M. Ziman. *Electrons and Phonons: The Theory of Transport Phenomena in Solids (Oxford Classic Texts in the Physical Sciences)*. Oxford University Press, 2001. ISBN: 0198507798.

[43] Jaeho Lee, Jongwoo Lim, and Peidong Yang. ''Ballistic Phonon Transport in Holey Silicon''. In: *Nano Letters* 15.5 (Apr. 2015), pp. 3273–3279. DOI: 10.1021/acs.nanolett.5b00495. URL: https://doi.org/10.1021/acs.nanolett.5b00495.

[44] Karl F. Graff. *Wave Motion in Elastic Solids (Dover Books on Physics)*. Dover Publications, 1991. ISBN: 0486667456.

[45] Stephen Elliott and S. R. Elliott. *The Physics and Chemistry of Solids*. Wiley, 1998. ISBN: 047198194X.

[46] T. Kühn et al. ''Heat transport in ultrathin dielectric membranes and bridges''. In: *Physical Review B* 70.12 (Sept. 2004). DOI: 10.1103/physrevb.70.125425. URL: https://doi.org/10.1103/physrevb.70.125425.

[47] Thomas Kühn. ''Phononic transport in dielectric membranes''. PhD thesis. 2007.

[48] H. F. C. Hoevers et al. ''Radiative ballistic phonon transport in silicon-nitride membranes at low temperatures''. In: *Applied Physics Letters* 86.25 (June 2005), p. 251903. DOI: 10.1063/1.1949269. URL: https://doi.org/10.1063/1.1949269.

[49] *PELCO Silicon Nitride and Silicon Dioxide Support FilmsNANO PMMA and copolymer*. Ted Pella Inc. URL: http://www.tedpella.com/pdfs_html/Silicon-Nitride-Dioxide-4pg.pdf.

[50] Frank P. Incropera and David P. DeWitt. *Fundamentals of Heat and Mass Transfer, 5th Edition*. Wiley, 2001. ISBN: 0471386502.

[51] M. L. Roukes et al. ''Hot electrons and energy transport in metals at millikelvin temperatures''. In: *Physical Review Letters* 55.4 (July 1985), pp. 422–425. DOI: 10.1103/physrevlett.55.422. URL: https://doi.org/10.1103/physrevlett.55.422.

[52] F. C. Wellstood, C. Urbina, and John Clarke. ''Hot-electron effects in metals''. In: *Physical Review B* 49.9 (Mar. 1994), pp. 5942–5955. DOI: 10.1103/physrevb.49.5942. URL: https://doi.org/10.1103/physrevb.49.5942.

[53] Francesco Giazotto et al. ''Opportunities for mesoscopics in thermometry and refrigeration: Physics and applications''. In: *Reviews of Modern Physics* 78.1 (Mar. 2006), pp. 217–274. DOI: 10.1103/revmodphys.78.217. URL: https://doi.org/10.1103/revmodphys.78.217.

[54] E. T. Swartz and R. O. Pohl. ''Thermal boundary resistance''. In: *Reviews of Modern Physics* 61.3 (July 1989), pp. 605–668. DOI: 10.1103/revmodphys.61.605. URL: https://doi.org/10.1103/revmodphys.61.605.

[55] Frank Pobell. *Matter and Methods at Low Temperatures*. Springer, 2007. ISBN: 3540463569.

[56] Maria Stepanova and Steven Dew, eds. *Nanofabrication: Techniques and principles*. Springer Vienna, 2012. DOI: 10.1007/978-3-7091-0424-8. URL: https://doi.org/10.1007/978-3-7091-0424-8.

[57] F. Guthrie. ''On a New Relation between Heat and Electricity.'' In: *Proceedings of the Royal Society of London* 21.139-147 (Jan. 1872), pp. 168–169. DOI: 10.1098/rspl.1872.0037. URL: https://doi.org/10.1098/rspl.1872.0037.

[58] Jon Orloff. *Handbook of charged particle optics*. Boca Raton: CRC Press/Taylor & Francis, 2009. ISBN: 978-1-4200-4554-3.

[59] *NANO PMMA and copolymer*. Microchem. URL: http://microchem.com/pdf/PMMA_Data_Sheet.pdf.

[60] K.J.S. Sokhey, S.K. Rai, and G.S. Lodha. ''Oxidation studies of niobium thin films at room temperature by X-ray reflectivity''. In: *Applied Surface Science* 257.1 (Oct. 2010), pp. 222–226. DOI: 10.1016/j.apsusc.2010.06.069. URL: https://doi.org/10.1016/j.apsusc.2010.06.069.

[61] M. David Henry et al. ''Degradation of Superconducting Nb/NbN Films by Atmospheric Oxidation''. In: *IEEE Transactions on Applied Superconductivity* 27.4 (June 2017), pp. 1–5. DOI: 10.1109/tasc.2017.2669583. URL: https://doi.org/10.1109/tasc.2017.2669583.

[62] Minna Nevala. ''Development of niobium-based superconducting junctions''. PhD thesis. 2012.

[63] M. David Henry et al. ''Stress dependent oxidation of sputtered niobium and effects on superconductivity''. In: *Journal of Applied Physics* 115.8 (Feb. 2014), p. 083903. DOI: 10.1063/1.4866554. URL: https://doi.org/10.1063/1.4866554.

[64] John R. Howell, M. Pinar Menguc, and Robert Siegel. *Thermal Radiation Heat Transfer*. CRC Press, 2015. ISBN: 1466593261.

[65] Mark Newman. *Computational Physics*. CreateSpace Independent Publishing Platform, 2012. ISBN: 9781480145511.